October 2021

Towards higher power factor in semiconductor thermoelectrics: bandstructure engineering and potential barriers

Adithya Kommini
University of Massachusetts Amherst

Towards higher power factor in semiconductor thermoelectrics: bandstructure engineering and potential barriers

Adithya Kommini

TOWARDS HIGHER POWER FACTOR IN SEMICONDUCTOR THERMOELECTRICS: BANDSTRUCTURE ENGINEERING AND POTENTIAL BARRIERS

A Dissertation Presented

by

ADITHYA KOMMINI

Submitted to the Graduate School of the
University of Massachusetts Amherst in partial fulfillment
of the requirements for the degree of

DOCTOR OF PHILOSOPHY

September 2021

Electrical and Computer Engineering

TOWARDS HIGHER POWER FACTOR IN SEMICONDUCTOR THERMOELECTRICS: BANDSTRUCTURE ENGINEERING AND POTENTIAL BARRIERS

A Dissertation Presented

by

ADITHYA KOMMINI

Approved as to style and content by:

Zlatan Aksamija, Chair

Eric Polizzi, Member

Jun Yan, Member

Christopher V. Hollot, Department Head
Electrical and Computer Engineering

ABSTRACT

TOWARDS HIGHER POWER FACTOR IN SEMICONDUCTOR THERMOELECTRICS: BANDSTRUCTURE ENGINEERING AND POTENTIAL BARRIERS

SEPTEMBER 2021

ADITHYA KOMMINI

M.S.E.C.E., UNIVERSITY OF MASSACHUSETTS AMHERST

Ph.D., UNIVERSITY OF MASSACHUSETTS AMHERST

Directed by: Professor Zlatan Aksamija

To keep up with the current energy demand and to sustain the growth requires efficient use of existing resources. One of the ways to improve efficiency is by converting waste heat to electricity using thermoelectrics. Thermoelectric devices work on the principle of Seebeck effect, where an applied temperature difference across the material results in a potential difference in the material. The possibility of drastic improvements in the efficiency of thermoelectric (TE) devices using semiconductor nanostructured materials renewed interest in thermoelectrics over the last three decades. Introducing confinement, interfaces, and quantum effects using nanostructures for additional control of charge and phonon transport made it possible to achieve this higher efficiency in thermoelectrics. However, improving TE efficiency by tuning charge transport is not completely understood especially the quantum effects that play a predominant role in nanostructures. This dissertation focuses on understanding the impact of bandstructure engineering, carrier scattering, and potential barriers on charge transport by accurately modeling the charge dynamics.

Smart material selection with desired bandstructure properties is explored in this thesis, especially in two-dimensional (2D) materials to maximize TE efficiency. We identify computationally inexpensive material selection rules using properties in 2D materials that can be obtained from material databases. We show that a 2D material having a combination of low effective mass, higher separation in the height of the step-like density of states, and valley splitting, which is the energy difference between the bottom of the conduction band and the satellite valley, equal to 5 kT will lead to a higher TE power factor. Further, we find that inelastic scattering with optical phonons plays a significant role: if inelastic scattering is the dominant mechanism and the energy of the optical phonon equals 5 kT, then the TE power factor is maximized. Introducing these material selection rules in MoS_2 provides a two-order increase in power factor compared to intrinsic values.

Potential barriers introduced in materials using nanocomposites, superlattices, as well as single and multiple barrier structures, improve TE performance using energy filtering. Energy filtering is a process of restricting the movement of carriers with kinetic energy smaller than potential barriers (thermionic emission). To study these effects, a comprehensive model is developed that can simulate the classical (thermionic emission) and quantum behavior (tunneling) of carriers by integrating Boltzmann transport equation (BTE) with Wigner approach to include the carrier-potential interactions. Here we study single-layer 2D MoS_2 with lateral potential barriers to introduce either energy filtering or carrier confinement by changing the direction of the electric field, with confinement resulting when the electric field is parallel and energy filtering when the electric field is perpendicular to the potential barriers. A Wigner-Rode model with electronic structure calculated from first principles to simulate the effect of the shape and size of potential barriers on parallel and perpendicular transport is implemented. Our results show that the power factor can be doubled, from 25 mW m^1 K^2 without barriers to over 50 mW m^1 K^2 for parallel transport in sharp, narrow potential wells.

Generally, modeling carrier transport in materials using semi-classical BTE assumes phonons to be in equilibrium at all temperatures. However, at low temperatures phonons can provide extra momenta to carriers through electron-phonon interactions of non-equilibrium phonons. This phenomenon is called phonon drag that gives a boost to Seebeck coefficient and controlled by the mean free path of phonons. This effect is predominant in low-dimensional materials due to the long mean free path of phonons. To understand the phonon drag contribution in a 2D material, carrier transport is modeled in single-layer MoS_2. Using accurate phonon distribution to calculate the coupling between carriers and phonons, the phonon drag contribution to Seebeck coefficient is evaluated. Our simulations show phonon drag boosts Seebeck coefficient up to 27% at low temperatures in MoS_2. Also, TA phonons contribute more towards phonon drag than LA phonons.

Recent research on twisted bilayer graphene (TBG) uncovered its unique electronic properties [1, 2, 3, 4]. Experiments showed superconductivity, correlated insulating states, and magnetism at different twist angles. The flat bands in TBG result in a sharp density of states (DOS) that is desirable for superior thermoelectric performance. Using BTE and bandstructure from exact continuum models, the power factor (PF) of TBG at different twist angles is modeled. Our simulations show the power factor in TBG is twice in magnitude at 100 K compared to single layer graphene (SLG). The peak PF is observed at a twist angle of 1.26° where the bandgap is high enough to improve the Seebeck coefficient compared to SLG by improving the TDF even though the electrical conductivity is lower. We observed an increase in PF of TBG with decreasing temperature, an unique behavior previously observed in superconductors with a high superconducting transition temperature. The strong TE performance along with the ability to fine-tune the behavior using twist angle makes TBG a solid candidate for future TE devices. Our results aid in improving TE power factors and further the development of efficient waste-heat scavenging, flexible 2D TE converters, and Peltier cooling of nanoelectronics.

TABLE OF CONTENTS

LIST OF FIGURES

Figure **Page**

CHAPTER 1

INTRODUCTION

Increase in demand for energy sources inspired the search for new and efficient technologies that can maximize the utilization of existing resources. Current estimated energy consumption in US as shown in Fig. 1.1 has 67.5% of energy resources lost in the form of waste heat. Re-purposing waste heat to generate electricity using thermoelectrics is a viable option to achieve the maximum efficiency in existing power generation methods. But, to achieve the desired electrical output, efficient thermoelectric devices are required. The efficiency of thermoelectric devices of a material for power generation is determined by dimensionless figure-of-merit (ZT) [7]:

$$ZT = \frac{\sigma S^2}{\kappa_e + \kappa_p} T \tag{1.1}$$

where σ is electrical conductivity, S is Seebeck coefficient, κ_e is electronic thermal conductivity, κ_p is lattice (phonon) thermal conductivity. In Eq. 1.1, S, κ_e, σ, depend on electronic structure of materials and κ_p depends on the phonon (lattice vibrations) transport alone. In the quest for efficient thermoelectric device/material, many materials have been investigated and studied over the years.

1.1 Physics behind thermoelectric energy conversion

Energy and particle transport accompany each other in a material, especially in thermoelectrics where a temperature is difference is applied across the material. A basic thermoelectric device based on *p*-type and *n*-type semiconductor legs connected at ends that

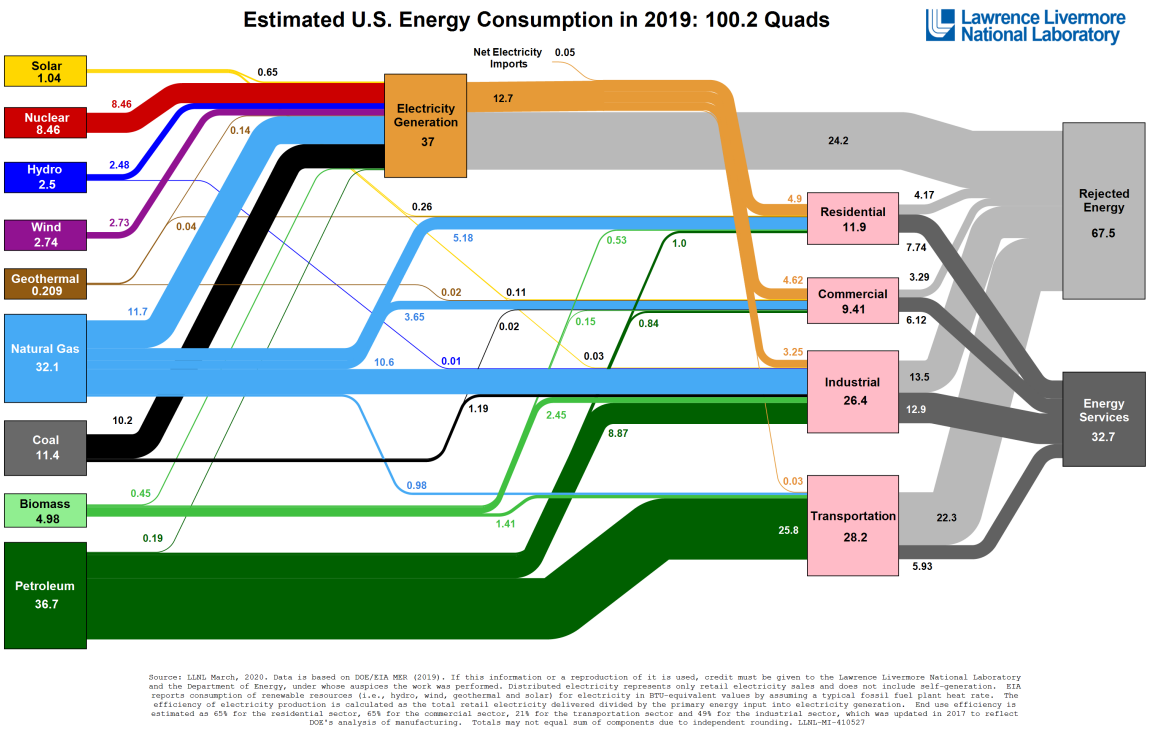

Figure 1.1: Different sources of energy being used to support the energy requirements and their corresponding share. Majority of the energy, approximately 67.5% is lost in the form of heat to the environment.

are maintained at different temperatures. This temperature gradient drives electrons and holes to diffuse from hot to cold side to distribute the energy. This results in Peltier cooling at the hot junction and a heating effect at the cold junction. In the process of this carrier diffusion, a potential difference is created between the two junctions. This whole process of potential difference (ΔV) creation across two junctions at different temperatures (ΔT) is called Seebeck effect. The energy transport that gives rise to heating and cooling trends are governed by Peltier coefficient (Π) and the potential difference between the junctions is caused by Seebeck Coefficient (S) where

$$S = -\Delta V/\Delta T. \tag{1.2}$$

Peltier coefficient (Π) and Seebeck Coefficient (S) are related using the Kelvin relation, which is given as,

$$\Pi = ST. \tag{1.3}$$

p-type and *n*-type semiconductor legs are connected, so that they are thermally parallel and electrically in series to create a thermoelectric device.

1.2 Thermoelectric Performance Parameters

Determining the efficiency of thermoelectrics using figure-of-merit (ZT) (Eq. 1.1) requires the calculation of Seebeck coefficient (S), electrical conductivity (σ) and thermal conductivity of both electrons (κ_e) and phonons (κ_p). In order to do that, Boltzmann Transport equation (BTE) coupled with relaxation time approximation is used to model carrier transport. BTE can capture the evolution of carrier probability distribution under the influence of different forces. Carrier transport occurs when the system is in a nonequilibrium state and to describe this nonequilibrium condition BTE is used. BTE is given as,

$$\frac{\partial f}{\partial t} + v \cdot \nabla_r f + \frac{F}{\hbar} \cdot \nabla_k f = \left(\frac{\partial f}{\partial t}\right)_c \tag{1.4}$$

where f is the distribution function. The left hand side of BTE is influenced by two factors, diffusion and drift. Diffusion is a result of the spatial gradient that effects f whereas drift is force exerted by electric field. The right-hand side (typically referred to as scattering or collision term) of the equation represents the interaction of this one particle with the rest of the particles in the system and the evolution of carrier probability distribution due to these interactions. To calculate the collision term in BTE, Fermi's golden rule is used, which gives rate of transition of a particle from one set of quantum states to other. By integrating the transition of a particle at a particular quantum state into all possible quantum states gives the scattering term for that particle. This scattering of particles is simplified using relaxation time approximation (RTA),

$$\left(\frac{\partial f}{\partial t}\right)_c = -\frac{f - f_0}{\tau}, \tag{1.5}$$

where τ represents the total relaxation time calculated by adding scattering rates from different processes and f_0 represents the equilibrium distribution of the carriers. Then the expressions for S, σ and κ_e are derived under the assumption that the local deviation from equilibrium is small and the relation between heat transport and carrier transport is included using the first law of thermodynamics. The expressions thus calculated are

$$\sigma = L^{(0)} \tag{1.6}$$

$$S = \frac{1}{eT}\frac{L^{(1)}}{L^{(0)}} \tag{1.7}$$

$$\kappa_e = \frac{1}{e^2T}\left(L^{(2)} - \frac{\left(L^{(1)}\right)^2}{L^{(0)}}\right) \tag{1.8}$$

$$L^{(\alpha)} = \int_0^\infty -\frac{\partial f_0\left(E\right)}{\partial E}(E - E_f)^\alpha \Xi(E) dE \tag{1.9}$$

$$\Xi(E) = e^2\tau(E)g(E)v^2(E) \tag{1.10}$$

where $L^{(\alpha)}$ is called transport integral, $\Xi(E)$ is called differential conductivity or transport distribution function (TDF). E_f is the Fermi energy, E is energy of the carriers, g(E) is density of states, τ(E) is energy dependent relaxation time, $\partial f_0\left(E\right)/\partial E$ is Fermi window and v(E) is group velocity of the carriers in the direction of the electric field or temperature gradient.

1.3 Trade-off between electrical conductivity and Seebeck coefficient

Even though ZT is a measure of thermoelectric energy conversion, the power factor σS^2, which is a part of ZT, is predominantly controlled by the carrier transport (electrons or holes). In metals, electrical conductivity σ is high due to the high density of electrons but S is low as most of the transport occurs near the Fermi level (E - $E_f \cong 0$). In insulators, the σ is low but S is high due to high bandgap. Semiconductors, on the other hand, have a moderate σ and S that give a good power factor compared to the insulators and metals

making them the suitable materials for thermoelectrics. Now, by carefully observing the expression for S, it can be interpreted as the weighted average of energies above the Fermi level. To improve it, the peak in TDF should be matched with the peak in Fermi window ($\partial f_0\,(E)/\partial E$) which occurs at the Fermi energy. But this alone is not sufficient because a perfectly symmetric function centered at Fermi level has a minimal contribution towards S. So, the peaks have to be matched by keeping the overlap asymmetric with respect to Fermi energy. Low-dimensional materials which have sharp features in the density of states will help to improve the S and σ simultaneously due to the asymmetry caused by those sharp features between the TDF and Fermi window. Doping can improve σ by moving the Fermi energy well into the conduction band, thereby improving the σ, but decreases the S due to the symmetry.

The electron group velocity, which depends on the effective mass (m_v) as $v(E) = \sqrt{2E/m_v}$, also causes trade-off between σ and S, especially in superlattices [8]. The bands having high effective mass results in the higher density of states and lower mobilities, resulting in high power factor. This is not the only possibility: even bands with high mobility and low effective mass have good power factor as velocity depends only on the curvature of the bands whereas the density of states depends on the entire dispersion relation. Selecting materials with a more suitable band structure can overcome this and better power factor can be achieved with optimal σ and S.

1.4 Improving thermoelectric power factor

High performance thermoelectrics can be created either by using materials with required properties in TE devices or by tuning the existing materials by employing techniques like bandstructure engineering, energy filtering. This thesis explores both approaches by studying power factor of low-dimensional materials to improve the TE performance. Even though we focus on improving the power factor, total thermal conductivity ($\kappa = \kappa_e + \kappa_p$) of semiconductors that effect ZT can be reduced without causing much change to the

electrical behavior, due to the vast difference in their transport behavior (differences in electron and phonon mean free paths). Also, phonons contribution to thermal conductivity is relatively higher than electrons and reducing phonon contribution gives significant performance gains. The phonon thermal conductivity (κ_p) depends on the lattice of the material and can be reduced by using different approaches like edge roughness and interface scattering [9, 10, 11], isotope insertion [12], grain boundaries [13, 14], and boundary confinement [15, 16]. These changes can modify the phonon thermal conductivity as they change the relaxation time of the phonons due to different scattering processes that are being introduced without impacting the charge transport.

Seminal work by Hicks and Dresselhaus [17] predicted that low-dimensional materials with sharp features in their density of states can significantly improve the power factor. Also, Mahan and Sofo [18] suggested that a structure having a narrow energy distribution with uninterrupted high carrier velocity in the direction of applied field results in high figure-of-merit. Towards this end, previous studies proposed simple material property criteria to narrow the search time for identifying the bulk materials or compounds that have better TE performance. Among them, the widely accepted criteria for bulk materials are low effective mass [19, 20], higher bandgap [20, 21, 22], higher band degeneracy [23, 20, 24, 25], doping and composition [24]. In our recent work, we studied the idea of using inelastic scattering mechanisms in a confined material at low temperatures to achieve an enhancement in Seebeck coefficient [26]. Modulation doping of material, by introducing doped islands in an undoped material [27, 28], and electrostatic gating [29] have also been shown to significantly improve electrical conductivity with little adverse effect on Seebeck coefficient, thus further boosting the power factor.

Energy filtering, where the transport is restricted to carriers with kinetic energy exceeding some potential barrier, also proved to enhance the power factor. There have been several studies implementing energy filtering in nanocomposites [30, 28], superlattices, cross-plane transport, as well as single and multiple barrier structures. Zide et al. [31] demon-

strated an increase in thermoelectric efficiency in a nanocomposite consisting of III-V semiconductors (specifically InGaAlAs) containing metallic nanoparticles of ErAs as energy-dependent scatterers. Yokomizo and Nakamura [32] showed that lateral graphene/h-BN superlattices drastically enhance the Seebeck coefficient compared to graphene. Neophytou et al. [33] achieved a simultaneous increase in the electrical conductivity and Seebeck coefficient due to grain boundaries in nanocrystalline silicon acting as energy filters. Also, unprecedented high values of Seebeck coefficient in a graphene-based interference device is observed [34, 35], where a series of gates are used to create a periodic potential in graphene. Subsequent work based on the non-equilibrium Green's function (NEGF) [36, 27] formalism with an effective-mass Hamiltonian studied the effect of smoothness and size of a potential barrier on thermoelectric parameters, but did not include detailed bandstructure and energy relaxation through inelastic scattering mechanisms.

Electron-phonon interactions have predominant control over the intrinsic properties of the material and they in turn control the TE performance. The general assumption that carrier scattering is controlled by equilibrium phonons fails at low temperatures. Below Debye temperature, a temperature at which most phonon modes become thermally excited, phonon can provide extra momenta to electrons and can drive a current in the direction of heat flow. This effect called phonon drag boosts the Seebeck coefficient, thereby improving the power factor. Phonons with long mean free paths especially acoustic phonons have major contribute towards phonon drag. The momentum transfer from phonon to electronic system is mostly from acoustic phonons due to their long mean free paths especially below Debye temperature. This effect is more pronounced in 2D materials, since phonon mean path is longer in 2D systems.

This dissertation is an effort to improve the thermoelectric power factor by studying the effect of electronic band structure along with dimensionality, phonon scattering and periodic potential barriers in 2D materials as discussed above. In particular, identifying the material parameters that effect the PF in 2D materials to formulate the material selection

rules. Twisted bilayer graphene (TBG) showed interesting properties due to the unique bandstructure dependency on twist angles. These bandstructure properties are explored in this thesis and the resulting boost to PF. The contribution of phonon drag is simulated to understand the contribution of non-equilibrium phonons in MoS_2 by calculating the full phonon distribution. Finally, the impact of spatially-varying potential barriers in MoS_2 is studied by modeling carrier transport using Wigner formalism to incorporate the quantum effects.

1.5 Outline of the dissertation

This dissertation is organized as follows: Chapter 2 discusses various low-dimensional material configurations studied in literature to understand the possibility of enhancing thermoelectric performance. Chapter 3 introduces the idea of improving power factor in a 2-D material and creating simple material selection rules that help in identifying future TE materials. The impact of spatially-varying potential barriers and the direction of electric field on TE performance in MoS_2 is discussed in chapter 4 by incorporating the carrier potential interactions using Wigner formalism. Chapter 5 discusses about solving coupled electron-phonon Boltzmann transport equation to study the contribution of phonon drag towards Seebeck coefficient in MoS_2. Chapter 6 explorers the unique properties of TBG that result in extraordinary high PF.

CHAPTER 2

IMPROVING TE PERFORMANCE IN HETEROSTRUCTURES AND LOW-DIMENSIONAL MATERIALS

On the quest towards improving the TE performance, many studies applied the approaches like energy filtering, bandstructure engineering to a range of materials with different chemical composition and dimensionality. Many review articles [37, 38, 39] presented the research on thermoelectric properties in bulk materials and the performance improvements achieved in those materials. Here, a brief review is presented to consolidate the TE performance reported in literature on different class of nano-structured materials.

2.1 3D heterostructures and superlattices

With the discovery of negative differential resistance (NDR) in narrow highly doped germanium *p*-*n* junctions by Esaki [40], a new era of electronics based on quantum tunneling devices was ushered in. These *p*-*n* junctions were called tunnel diodes as they demonstrated interband tunneling of carriers from the valence band on the *p*-side to conduction band on the *n*-side and vice versa. Tsu and Esaki [41] found that in the direction of a one-dimensional periodic potential, such as that found in a heterostructure (superlattice), electrons are localized to discrete energy states analogous to electrons in a two-dimensional electron gas. Further, due to the comparable dimensions of these potentials with electron wavelengths, the wave nature of electron leads to phenomena such as interference and tunneling. In such structures, when the energy of electrons coincides with one of the discrete energy states achieved by tuning the applied bias, electron can tunnel through the barriers and can have near-perfect transmission. With further increase in the applied bias,

the number of available electrons decreases, thus reducing the current flowing through the structure. Ultimately, the current increases again when high enough bias is applied to cause thermionic emission of electrons over the top of the potential barrier. This distinct feature is popularly known as NDR and has found numerous applications in devices such as high-frequency oscillators, frequency converters, and detectors and also exhibits great potential in high-speed logic devices and switches.

2.1.1 Progress in numerical simulation of 3D heterostructures

The semi-classical Boltzmann transport equation, which is used widely to simulate electron and thermal transport in electronic devices, is not adequate to capture quantum effects that are predominant in RTDs. Various quantum-transport frameworks such as the Wigner formalism and the related density matrix approach, as well as non-equilibrium Green's functions (NEGF), have been employed to study transport in RTDs. NEGF was one of the first methods used to study the transport in RTDs. Lake and Datta [42] studied the effect of energy broadening and inelastic scattering and reported an enhanced valley current due to inelastic scattering with simultaneous enhancement of occupation of the resonant states. Time-dependent transport capabilities of NEGF were demonstrated by simulating RTD [43] in mesoscopic region. Nam Do et al. [44] used fully self-consistent non-equilibrium Green's function approach to study the the impact of quantum-well width, the barrier thickness and the temperature, and showed their effect on peak- and valley-current ratio (PVR). PVR, as the name implies, is the ratio between the currents at the peak before the onset of the NDR and the valley after it, which helps to determine the feasibility of using the RTD for device applications.

Wigner formalism is one of the first methods [45] used to simulate the transport behavior of quantum-well RTD and their NDR. Biegel and Plummer [46] implemented a self-consistent Wigner-function-based quantum device simulation using the RTDs as a test case. A comparison between different iterative methods was presented here to solve the

Wigner function. It concluded that transient Gummel approach is reasonably accurate with low computational resource requirement for device simulations. A unified approach [47] was proposed to merge Wigner functions with semi-classical Boltzmann transport equation and treat the scattering term as a generating term.

2.1.2 Thermoelectric properties of superlattices

Quantum effects in heterostructures have a large impact on their thermoelectric properties, affecting both the Seebeck coefficient S, which is related to the average transport energy per carrier, and the conductivity σ. With the discovery of high figure-of-merit (ZT) in Bi_2Te_3 quantum well superlattices [48] renewed the interest in low-dimensional heterostructures for thermoelectric applications. High anisotropy along certain direction at low widths of quantum wells are shown to be the reason for this enhancement. This kicked off extensive research into understanding their thermoelectric properties and possible use in thermoelectric generators. Their predictions were later revised [49] when it was shown that the enhancement is controlled by period of the superlattice and not by the width of the well. Also, the overall ZT is projected to be less than one when tunneling is introduced between quantum wells. This idea was experimentally validated using PbTe/$Pb_{1-x}Eu_xTe$ superlattices [50] with a fivefold increase in ZT compared to bulk PbTe. A more extensive analysis [51, 52] for the case which includes a non-zero barrier and effects of carrier tunneling, revealed that the in-plane thermoelectric performance is not superior to bulk systems. Later short-period Si/Ge superlattice structures were shown [53] to provide higher ZT compared to thin-film Si/Ge and bulk Si-Ge alloys, which was attributed to the reduction in thermal conductivity. A further improvement [54] in ZT is reported in Si/Ge superlattices by applying strain to further tune the conduction band structure. Experimental studies demonstrated the thin-film thermoelectric coolers using both single heterostructure and superlattice structures from SiGe/Si [55, 56, 57, 58, 59, 60].

Using an exact numerical solution, a complete treatment of powerfactor in PbTe quantum well and quantum wire superlattices showed [61] weaker dependencies on potential barrier. Extending the study to GaAs quantum wire superlattices [62], it was established that significant enhancements in power factor can be achieved from restricting phonon transport. PbTe/PbTeSe-based superlattices are experimentally shown [63, 64] to improve ZT by 50% relative to bulk PbTe. This can be attributed to a reduction in thermal conductivity, an effect of the increase in scattering due to alloying. Later, majority of studies used this approach to improve ZT. Ge quantum dot in Si quantum dot superlattices were shown [65] to improve ZT by reducing the thermal conductivity due to scattering of phonons. Theoretical calculations of TE properties in superlattice nanowires [66] based on lead salts (PbS, PbSe and PbTe) exhibited a significantly higher ZT values, especially for 5 nm diameter wires.

Even though significant improvement in ZT was reported by restricting thermal conductivity, further improvement can be achieved by tuning the TE power factor. Many studies proposed mechanisms and ways to improve power factor in superlattices by tuning the band structure [67, 68, 69]. Energy filtering, a process of restricting movement of carriers with kinetic energy smaller than barrier height, has been consistently found to enhance the overall power factor. It raises the average energy of carriers and thereby its Seebeck coefficient. Nanocomposites [30, 28, 31], superlattices [32] as well as single and multiple barrier structures have been used to introduce some form of energy filtering in a material. Grain boundaries in highly-doped nanocrystalline Si have also been shown to simultaneously increase the Seebeck coefficient and conductivity [33]. Several studies [36, 27, 34, 35] tried to understand the effect of potential barrier smoothness and their structure on thermoelectric performance. Using a series of gates placed periodically in graphene, creating periodic potentials [34, 35] that resulted in a drastic increase in Seebeck coefficient. Thermionic emission over the barrier and tunneling through the barrier, control transport in these structures as shown in Figure 2.1. Semi-classical transport (diffusive transport) theory like Boltzmann

transport equation is capable of recreating the thermionic emission over potential barriers. Quantum effects like tunneling are typically simulated using density matrix formulation, Wigner formalism and non-equilibrium Green's functions.

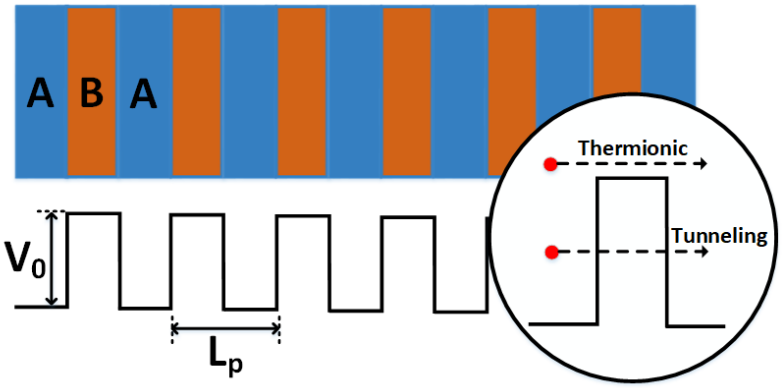

Figure 2.1: Periodic potential barriers can be used to understand the superlattice or heterostructure. Here, V_0 is the height of potential barrier and L_p is the period of the potential barriers. Due the presence of potential barriers, carrier transport in the system is controlled by thermionic emission over the barrier and tunneling through the barrier. Adapted from [5]

2.1.3 Wigner formalism

In the semi-classical Boltzmann transport equation (BTE), widely used in device simulation, electrons are treated as point particles [70, 71]. Despite its widespread use, this approach is unable to explain some device effects, such as underestimating the threshold voltage in ultra-thin body MOSFET [72, 73], and the carrier interactions with the rapid potential changes across heterojunctions. The impact of sharp spatially-varying potentials on transport in a superlattice can be simulated using the Wigner formalism. The Wigner formalism [74, 75] includes an additional quantum evolution term in addition to drift term that can capture the spatial variation in potential. The Wigner formalism has been the subject of an extensive recent review article [76]. BTE can be modified as follows to include Wigner formalism for rapid varying spatial potentials:

$$\left(\frac{\partial}{\partial t}+v_r\nabla_r+\frac{eF}{\hbar}\nabla_k\right)f_w\left(r,k,t\right)=Qf_w\left(r,k,t\right)+\left(\frac{\partial f_w}{\partial t}\right)_{coll} \tag{2.1}$$

where $f_w\left(r,k,t\right)$ is called Wigner distribution function, which is written as

$$f_w\left(r,k,t\right)=\frac{1}{2\pi}\int dr' e^{-ir'k}\rho\left(r+\frac{r'}{2},r-\frac{r'}{2}\right) \tag{2.2}$$

where the mixed state is represented by the density operator ρ. Here the coordinates r and r' represent the center of mass and spread of the electron wave packet, respectively. The potential operator $Qf_w\left(r,k,t\right)$, often called the quantum evolution operator, is given as

$$Qf_w\left(r,k,t\right)=\int dk' V_w\left(r,k-k'\right)f_w\left(r',k,t\right) \tag{2.3}$$

where the Wigner potential $V_w(r,k)$ is itself also obtained through a Wigner transform

$$V_w\left(r,k\right)=\frac{1}{i\hbar(2\pi)^d}\int dr' e^{-ir'k}\left(V\left(r+\frac{r'}{2}\right)-V\left(r-\frac{r'}{2}\right)\right). \tag{2.4}$$

$V_w\left(r,k\right)$ can be simplified as

$$V_w\left(r,k\right)=\frac{2}{\pi\hbar}\,Im\{e^{2ikr}\hat{V}(2k)\} \tag{2.5}$$

where $\hat{V}(k)$ is spatial Fourier transform of V

$$\hat{V}(k)=\int_{-\infty}^{\infty}V(r)e^{-ikr}dr. \tag{2.6}$$

The potential operator $Qf_w\left(r,k,t\right)$ is usually decomposed into two components: a slowly-varying, often called classical, potential (such as the applied external bias) V_{cl}, and sepa-

rate, rapidly-varying quantum-mechanical portion V_{qm}. Together, these two make up the potential according to

$$V(x) = V_{cl}(x) + V_{qm}(x). \tag{2.7}$$

By including the additional effect of rapidly varying potentials in the BTE, the resulting steady-state Wigner-Boltzmann transport equation (WBTE) can be written as (from Eq. 2.1)

$$\left(v_r \nabla_r + \frac{eF}{\hbar}\nabla_k\right) f_w(r,k,t) = Q f_w(r,k,t) + \left(\frac{\partial f_w}{\partial t}\right)_{coll}. \tag{2.8}$$

The collision term helps to further incorporate the semi-classical effects like energy and momentum relaxation from time-dependent perturbation theory. The Wigner formalism permits us to couple the interdependencies between quantum and semi-classical effects, as it uses a phase-space formulation. Wigner formalism can represent quantum dynamics in a phase-space formulation, which allows to better understand the carrier energy relaxation in the presence of both inelastic scattering and periodic potential barriers. Even though the Wigner formalism allows us to include quantum effects, there are several limitations to its use in quantum device modeling. In some Wigner simulations, the use of semiclassical boundary conditions for contacts results in unphysical results. This is due to the nonlocal nature of Wigner equation which is incompatible with the standard boundary scheme especially in the coherent regime that produces nonunique solutions [77, 78]. Dissipation and decoherence phenomena also pose a challenge in using Wigner approach. Even though they provide a unique solution, the results may be unphysical. The type of collision operator used in Wigner transport equation to describe the dissipative transport also causes anomalous behavior like negative probability-density [79]. Simplified local scattering models like relaxation time approximation (RTA) and Boltzmann-like treatments are not enough to overcome these unphysical behaviors [80]. Some studies proposed alternate approaches by density matrix using Lindbald-type scattering superoperators [81, 82] and conditional wave functions [83].

2.1.4 Non-equilibrium Green's functions

The ability to simulate electron-electron correlations in the time domain is a central feature of the non-equilibrium Greens's function (NEGF) formalism, which allows it to capture and simulate many-body quantum effects in nanoscale devices. A comprehensive review on nanoscale device modeling using NEGF was published by Datta [84]. Here we provide a brief overview of the technique before delving into its recent applications in studying transport in RTDs and thermoelectric devices. The equations of motion in the NEGF formalism in the steady state are given by the Dyson and Keldysh relations [85, 86, 87] as

$$\hat{G}^R(E) = [E\hat{I} - \hat{H}_0 - \hat{V}_c - \hat{\Sigma}^R(E)]^{-1}$$

$$\hat{G}^<(E) = \hat{G}^R(E)\hat{\Sigma}^<(E)\hat{G}^A(E)$$

where $\hat{V_c}$ represents the coherently treated interactions that include the mean-field Coulomb potential $\hat{V_c}^{m-f}$ and the electronic disordered part $\hat{V_e}^{rand}$. The spectral self-energy used to treat the incoherent interactions is expressed as

$$\hat{\Gamma} = i(\hat{\Sigma}^R - \hat{\Sigma}^A) = i(\hat{\Sigma}^< - \hat{\Sigma}^>), \tag{2.9}$$

where the retarded self-energy used to include the electron-phonon interactions is defined as

$$\hat{\Sigma}^R(t) = \Theta(t)(\hat{\Sigma}^< - \hat{\Sigma}^>). \tag{2.10}$$

The expectation values of the observables and current operator are calculated using the relation between density matrix and Green's functions.

The NEGF technique has found applications in understanding the impact of quantum effects on electronic and thermoelectric transport, as well as finding ways to further improve TE properties through confinement in heterostructures. The effect of confinement on the thermoelectric performance in Si/Ge/Si superlattices was simulated using NEGF. Strain-induced energy splitting in Si/Ge/Si superlattices is shown to improve power factor

by four orders in magnitude [88]. However, the gains in TE performance expected in such structures was shown to be limited by the reduction in conductivity of superlattices with thin barriers [89]. Quantum wire superlattices with lateral confinement were also studied with NEGF, while including the scattering processes due to electron-phonon couplings, phonon anharmonicity, charged impurities, surface and interface roughness and alloy disorder [90]. Thermionic emission and tunneling of carriers in periodic superlattices were simulated in the NEGF formalism [36, 27], and their effect on TE properties has been found to improve the power factor. These studies also investigated the optimum size and shape of the potential barriers in Si-based superlattices to further improve TE performance. They found that hierarchically designed materials, containing heterostructures at varying scales from the atomic to the microscopic, can significantly impact transport and improve the TE power factor [91]. Double-barrier RTDs were simulated in the NEGF formalism, with self-consistent treatment of inelastic scattering, to show the enhanced valley current which is a consequence of enhanced occupation of resonant state [42].

2.2 Quantum Wires

Quantum wires provide more quantum confinement than quantum wells. There are many theoretical studies showing a huge improvement in ZT due to additional confinement. But there is lack of experimental results that indicate the same. Boukai [92] et al. and Hochbaum [93] et al. claimed a ZT of 0.6 for silicon nanowires. There are reports showing that the boundary scattering in thin nanowires reduces thermal conductivity that improves ZT at low temperature. They also reported an improvement in ZT at low temperatures and attributed it to the phonon drag effects. Ryu et al. [29] also reported an increase in the contribution of phonon drag towards the thermoelectric efficiency at low temperatures. This phonon drag increases the Seebeck coefficient by using a phonon mode in electron transport that doesn't contribute much to thermal conductivity.

2.3 Quantum Dots

Quantum dots have zero dimension which provides high levels of quantum confinement. This gives a sharp density of states required to achieve high power factor. A single quantum dot doesn't help in making a thermoelectric device. It requires an array of quantum dots to form a thermoelectric device. The transfer of heat from one location to other require the movement of the electrons which is restricted if the energy barrier is narrow, and carriers are highly confined. If the barrier is shallow, then the sharp density of states is lost. When 3D array of dots is formed, then they behave like a bulk crystal. In their work, Linke et al. [94] studied the coupling between quantum dot energy level and reservoirs broadens the density of states and reduces the efficiency of the thermoelectric conversion process.

2.4 Resonant tunneling diodes in 2D lateral heterostructures

Tuning the band alignment at lateral heterojunction interface can open up interesting applications by optimizing their electronic and optical properties. Using one-step tube-moving chemeical vapor deposition method [95], a lateral WS_2/$WS_{2(1-x)}Se_{2x}$ hetrostructure was synthesized. Controlling the ratio of WSe_2 and WS_2 in evaporaton sources enables the tuning of the band alignment in heterostructures. Another approach to tuning the bandgap [96] in MoS_2 nanoribbons is introducing the sulfur vacancies, which enabled the creation of double barrier quantum well structure (DBQW). Following this approach [97] and using NEGF based on tight-binding calculations, a DBQW of armchair MoS_2 nanoribbons with two sulphur line vacancies was simulated. The resultant analysis showed that the double barrier structure has a PVR of about 78 at room temperature.

One of the first demonstrations [98] created pristine multi-junction heterostructures by direct synthesis based on graphene, MoS_2, $MoSe_2$ and WSe_2. This led to the creation of RTD in an atomically-thick stack with NDR. The spectrally-narrow NDR created in this structure, is superior to manually stacked heterostructures that were studied previously.

TMDs in the symFET architecture [99] have been shown to achieve PVR up to 10^9 compared to few hundred observed in graphene or III-V RTDs. Also, the ability to achieve such high PVR even in nanoscale devices makes them promising candidates for digital logic applications. A vertical heterostructure based on phospherene/rhenium disulfide (BP/ReS_2) demonstrated NDR with a PVR up to 6.9 at 180 K [100]. A ternary inverter was also created from this heterostructure that exhibited three distinct logic values, demonstrating a proof of concept for future multi-valued logic devices.

2.5 Power factor in 2D heterostructures

In addition to having large electron mobilities, some 2D materials have exhibited interesting thermoelectric (TE) properties, including possessing a large Seebeck coefficient, also called thermopower. It is defined as the ratio of the voltage produced by thermally diffusing electrons and the temperature gradient that is driving their diffusion from the hot side to the cold. Research in this area started with the measurements of TE transport in graphene [101], which exhibited anomalous TE transport of Dirac particles [102]. More recently, the enhanced TE Seebeck coefficient in graphene [103] was attributed to the role of hydrodynamic transport through inelastic scattering, which also leads to a violation of the Mott relation for the Seebeck coefficient (not to be confused with the Schottky-Mott rule for band alignment)

$$S_{Mott} = -\frac{\pi^2 k^2 T}{3|e|\sigma} \frac{d\sigma(E)}{dE}\bigg|_{E=E_f}. \tag{2.11}$$

Proposals to enhance the TE properties of graphene used heterostructures [34] and functionalization [104]. Graphene also exhibited a significant phonon drag component of the Seebeck coefficient [105], which is defined as the additional thermopower caused by the exchange of momentum between the heat-carrying lattice vibrations (phonons) and the electrons. This effect is particularly prominent at low temperatures where the diffusion thermopower is typically low.

Using both carrier and phononic engineering on a $ZrSe_2$/$HfSe_2$ single-layer superlattice [106], a ZT of 5.3 in *n*-type and 3.2 in *p*-type device was achieved. First-principles calculations along with Boltzmann transport equation showed that this is achieved due to the highly degenerate nature of the conduction bands in *n*-type device. A partially overlapped graphene/graphene vertical heterostruture [107] studied using atomistic tight-binding Hamiltonian demonstrated that the ZT can reach unity at room temperature. An analysis [108] on van der waals heterostructures with multilayer TMDs sandwiched between two graphene electrodes identified WSe_2 and $MoSe_2$ as the ideal TMDs that can provide high TE conversion efficiency. Graphene/*h*-BN/graphene vertical heterostructures are synthesized [109] to study their TE performance. Measurements in these structures uncovered a significant Seebeck coefficient at the material interfaces, which makes such heterostrutures suitable candidates for TE applications. Twisted bilayer graphene vertical heterostructures are studied extensively [110] due to their interesting properties like magic angles that can induce superconductivity, described in the previous section. With regards to their thermoelectric properties, measurements showed exceptional cross-plane thermopower, attributed to phonon drag from out-of-plane phonon modes (ZA/ZO'). Besides twisted graphene bilayers, MoS_2 has been shown to also exhibit a phonon drag effect [111].

2.6 Phonon drag

At low temperatures, the conventional theory of Seebeck coefficient based on the lattice being in equilibrium breaks down. Frederikse [112] shows that in antimony-doped (n-type) germanium at low temperatures due to the non-equilibrium phonon distribution boosting the electron transport. This increase in Seebeck coefficient and the corresponding contribution towards Seebeck coefficient is called *phonon drag*. Also, they show that the contribution by non-equilibrium phonon distribution is proportional to the ratio of phonon and electron mean free path. Similarly, Geballe and Hull [113] measured Seebeck coeffi-

cient between 20 K and 375 K in both p-type and n-type germanium. They show that there is a significant improvement in Seebeck coefficient at low temperatures. In a single crystal of molydenite, Mansfield and Salam [114] showed a similar effect on Seebeck coefficient. Later, significant contribution from phonon drag towards Seebeck coefficient is observed in *n*-type InSb [115]. An extensive study by Herring [6] developed the theory to effectively include the phonon drag, the contribution from non-equilibrium phonons on Seebeck coefficient.

The scattering of phonons with the charge carriers (either electrons or holes) improves the net energy transport in the direction of the carrier movement. The predominant effect of the temperature on phonon drag is dependent on the randomness of phonon transport, a consequence of higher phonon-phonon collisions/scattering. Since phonon-phonon scattering increases with increase in temperature phonon drag is mostly observed at low temperatures. To understand the factors that drive the phonon drag and their effect, the factors that effect the Seebeck coefficient should be studied. For a doped non-degenerate semiconductor with required charge carriers, the electronic contribution towards Seebeck coefficient is,

$$S_e = \frac{E_f - E_b - \Delta E_T}{eT} \tag{2.12}$$

where E_f is the Fermi level, E_b is the energy at edge of either conduction or valence band based on their doping, and ΔE_T, is the average energy of carriers that participate in transport. The difference between the band edge and Fermi level, $E_f - E_b$ is determined by the doping that controls the number of carriers available. Any material with density of states effective mass of m_d^*, available energy states at a given energy is

$$N(E) = \frac{4\pi}{\hbar^3} 2 m_d^{*3/2} |E - E_b|^{1/2}. \tag{2.13}$$

Integrating $N(E)$ over energy gives us the available carriers in a material. Hence, $E_f - E_b$ can be calculated using

$$\frac{|E_f - E_b|}{kT} = \frac{2(2\pi m_d^* kT)}{\hbar^3 n} \tag{2.14}$$

for a material with n available carriers. This helps to calculate the electronic contribution towards Seebeck coefficient (S_e) as,

$$S_e = \mp 86.2 \left[ln\left(\frac{8.7 \times 10^{15}}{n}\right) + \frac{3}{2}\, ln\left(\frac{m_d^*}{m_0}\right) + \frac{|\Delta E_T|}{kT} + \frac{3}{2} ln\, T \right] \tag{2.15}$$

To calculate $\Delta E_T/kT$, assuming equilibrium conditions with relaxation time τ_e the first order perturbation to electronic distribution at a electric field of F is

$$f^{(1)} \propto \tau_e F \Delta_k f^{(0)}, \tag{2.16}$$

where $f^{(0)}$ is the equilibrium or Fermi Dirac distribution. From this, average transport energy can be calculated by averaging energy using group velocity and relaxation time as weights,

$$\Delta E_T = \frac{\langle v^2 (E - E_b)\tau_e \rangle}{\langle v^2 \tau_e \rangle}. \tag{2.17}$$

Except τ_e, average transport energy is controlled by the features in the material band structure. Some studies approximate the relaxation time τ_e as a function of $E - E_b$ as,

$$\tau_e \propto |E - E_b|^r. \tag{2.18}$$

Based on the scattering process the exponent r is changed to simulate their effect on carriers. Using full scattering rate equations instead of the Eq. 2.18 improves the accuracy of the calculated Seebeck coefficient.

CHAPTER 3

SELECTION RULES FOR IDENTIFYING HIGH POWER FACTOR THERMOELECTRICS IN 2D MATERIALS

3.1 Introduction

One of the factors that limits our ability to improve power factor by band engineering, is the strong coupling between S and σ. Especially in semiconductors they have opposite behavior with respect to the carrier density and cannot be tuned independently. Hence, careful selection of materials with desired properties is required to boost the power factor. Towards this end, previous studies proposed simple material property criteria to narrow the search time for identifying the bulk materials or compounds. Low effective mass [19, 20], higher bandgap [20, 21, 22], higher band degeneracy [23, 20, 24, 25], doping and composition [24] of bulks materials are shown to be good indicators of high TE performance. More complex material descriptors or parameters are proposed to combine different material properties that can be used to evaluate the material capabilities. One of the first ones is the B-factor or material factor or β introduced by Chasmar and Stratton [116], that can be used as material descriptor independent of the carrier density (thereby independent of Fermi energy). A material with high β and optimal carrier density was shown to provide higher ZT [117]. To understand the anisotropy contribution to TE performance b-factor [118] is defined by expanding B-factor to include any form of band structure and band degeneracy. The higher band degeneracy requirement for high performing thermoelectrics [20, 24] is often proved using a simple constant relaxation time approximation (CRTA) or constant mean-free-path approximation. The first principles band structure calculations along with comprehensive electron-phonon scattering rates improved our understanding on the effect complex band

structures. In a material with multiple anisotropic valleys, the relative strength of intra vs inter valley electron-phonon scattering is shown to control the TE performance more than the degeneracy alone [118]. Parameters like Fermi Surface Complexity Factor [119] (FSCF) are used to quantify the effect of anisotropy and band degeneracy on TE performance in complex band structure materials. In an effort to come up with a metric that can help to identify materials with single cut-off energy, as proposed by Mahan [18], shape factor [120] (SF) a measure of the asymmetry in density of states (DOS) is proposed. A high throughput search among the known compounds revealed that the shape factor should approach unity to maximize ZT. The required shape for the DOS to achieve it resembles a step-like function, which is the shape of DOS in 2D systems. The material characteristics that are proposed to identify high performing TE's and described here, are consistent with the conclusions from our previous study [26]. A system with 2D DOS (using an inversion in gated silicon-on-insulator device), where the inelastic scattering (like intervalley scattering) of phonons with 5 kT is dominant is showed to enhance power factor. There is a need for further research in to formulating better or complete material descriptors in intrinsic 2D materials to identify high power factor materials.

With the advent of new 2D materials like single TMDs, the TE efficiency of these materials is of increasing interest. Even though reports suggest that an improvement in the power factor of these materials [121, 122, 123], but higher thermal conductivity restricts them from achieving higher ZT. Apart from TMDs, there are other 2D materials that have exceptional electronic and thermal properties, and a few exhibits good power factor as well. But it is neither obvious nor it is feasible to synthesize and test every 2D material. We need more insight into the relation between material parameters and TE efficiency, which can help in formulating the material selection rules for new efficient TE materials. Using publicly available material databases, studies [124, 125, 126] have predicted materials with weak van der Waals forces that can be exfoliated into single-layer forms. With this extensive and growing knowledge, there is a need to explore the possibility of their

use in future thermoelectrics. The main aim of this study is to use the distinct features of 2D materials and formulate simple yet powerful material selection rules that can provide optimum power factor. We focus on those material parameters that are easily available or that require computationally inexpensive calculations, to reduce the time required for initial material capability evaluation.

The selection of the material for maximum energy conversion at a given temperature depends on the interplay between the subband structure and effectively using the inelastic scattering mechanisms to take the advantage of such subband structure. Simulation for thermoelectric conversion coefficients in a silicon nanoribbon showed an enhancement in Seebeck coefficient at low temperatures in situations where inelastic transitions are dominant and little or no elastic interactions in the form of acoustic and surface roughness scattering. A further detailed study showed the formation of almost delta shaped transport distribution function due to the discrete band structure in confined nanostructures that restricts the electron transport to the lowest subbands. This forces electrons to acquire or emit the required energy to occupy these energy levels after scattering which is assisted by the optical phonons due to the dominant intervalley optical phonon scattering. In addition to that, we observed that a delta shaped TDF alone can't provide maximum enhancement, the Fermi window decides the extent of this enhancement. Furthermore, by applying external gate bias and thereby rearranging the subbands, we can achieve further control on enhancement in the thermoelectric Seebeck coefficient by tuning the TDF. Changing the density-of-states effective mass affects the height of the step in the TDF and further tunes the enhancement; however, the corresponding change in the subband structure limits the advantage from reduced effective mass.

In our study, the 2D nature is imparted by confining a bulk material and the applied gate voltage controls the spacing in the discrete band structure, thereby creating a strong interdependence that affects the enhancement. So, to avoid it an intrinsically 2D material can be used which will have an independent native discrete band structure and then a detailed

Table 1: Comparison of important material parameters between a Dirac material and a semiconducting 2D material.

Parameters	Dirac Material	Semiconducting 2D material
E_n	$\hbar v_F k_t$	$\frac{\hbar^2 k_t^2}{2m_n^*}$
$D_n(E) = \frac{g_s g_d}{2\pi}\frac{k}{\Delta E}$	$\frac{g_s g_n^v}{2\pi}\left(\frac{E_n}{\hbar^2 v_F^2}\right)$	$\frac{g_s g_n^v}{2\pi}\left(\frac{m_n^*}{\hbar^2}\right)$
Γ^{el}	$\Gamma_0^{el} D_n(E)$	$\Gamma_0^{el} D_n(E)$
Γ^{inel}	$\Gamma_0^{inel}\{(N_v+1)D_n(E-E_{ph})\Delta_1 + N_v D_n(E+E_{ph})\Delta_2\}$	$\Gamma_0^{\text{inel}}\{(N_v+1)D_n(E-E_{ph})\Delta_1 + N_v D_n(E+E_{ph})\,\Delta_2\}$
TDF $v^2 D_n(E)\tau_n(E)$	Elastic: $\frac{v^2}{\Gamma_0^{el}} = \frac{v_F^2}{\Gamma_0^{el}}$ Inelastic: $\frac{v_F^2 D_i(E)}{\Gamma_0^{inel}}\left(\frac{1}{D_f(E+E_{ph})\mathrm{N_v}\Delta_2 + D_f(E-E_{ph})(\mathrm{N_v}+1)\Delta_1}\right)$	Elastic: $\frac{v^2}{\Gamma_0^{el}} = \frac{2E}{m_n^*\Gamma_0^{el}}$ Inelastic: $\frac{v^2}{\Gamma_0^{inel}}\left(\frac{1}{\mathrm{N_v}\Delta_2 + (\mathrm{N_v}+1)\Delta_1}\right)$ intravalley $\frac{v^2}{\Gamma_0^{inel}}\frac{D_i(E)/g_i^v}{ZD_f(E)/g_f^v}\left(\frac{1}{\mathrm{N_v}\Delta_2 + (\mathrm{N_v}+1)\Delta_1}\right)$ intervalley

analysis in such material gives more insight on proposed method for achieving thermoelectric enhancement. A possible extension to this work can be implementing our approach in such 2D materials to observe the nature of the enhancement and formulating a general criteria to design an efficient thermoelectric device.

3.2 Parameters that effect power factor

Improving the power factor requires identifying the material parameters that effect the Seebeck coefficient (S) and electrical conductivity (σ). Using Boltzmann transport equation (BTE) under relaxation time approximation and assuming a small perturbation from equilibrium, S and σ in 2D systems can be calculated using Eq. 1.6 and Eq. 1.7. The transport integrals (L^α) and TDF (σ_n(E)) in 2D systems are defined as,

$$L^\alpha = \sum_n \int_0^\infty (-\partial f_0/\partial E)\,(E + E_n - E_f)^\alpha \sigma_n(E) dE, \tag{3.1}$$

$$\sigma_n(E) = e^2 \tau_n\,(E)\, D_n\,(E)\, v^2(E), \tag{3.2}$$

Here E_f is the Fermi energy, E_n is the bottom of subband or valley n, D_n(E) is density of states (DOS) of valley, τ_n(E) is the energy-dependent relaxation time, and v(E) is the velocity of the carriers. The Fermi window $\partial f_0/\partial E$ is symmetric about E_f and has a spread of about 10 kT. The relaxation time of the carriers depends on dominant scattering mechanisms in the material and has varying dependency on energy (E). Assuming that the scattering completely randomizes the transport, the relaxation time is calculated by taking an inverse of the sum of scattering rates.

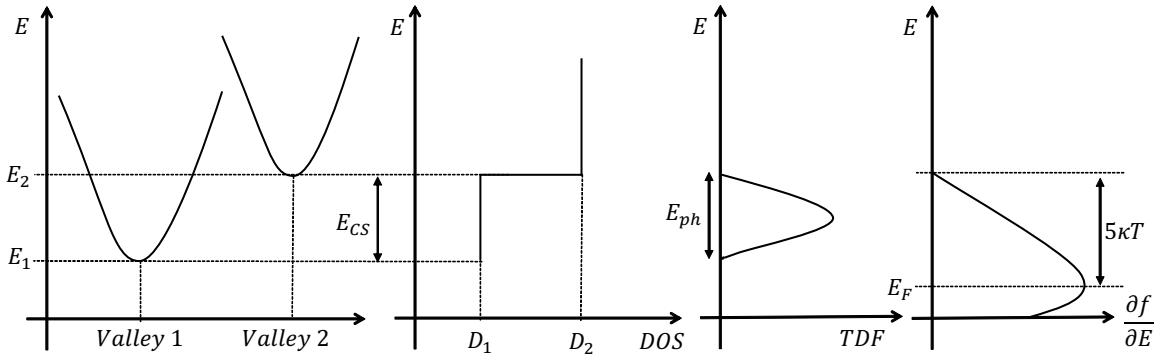

Figure 3.1: Schematic to show the parameters defined by the band structure and DOS of a 2D material. The step-like DOS along with the inelastic scattering of carriers results in window-shaped TDF. The approach used in our study is to maximize the power factor by matching window-shaped TDF and Fermi window.

In effective mass approximation, velocity of carriers and DOS can be defined using the effective mass of the valley and the energy. Now observing the transport integral, it will be apparent that TDF has to be maximized to improve σ. Also, it is shown that a δ-shaped TDF is needed for maximum achievable S [18]. But in realistic conditions, a delta-shaped TDF is not feasible in 3D materials due to the quadratic nature of the relaxation time (τ_n) and density of states (D_n), which cancels each other gains ($\tau_n \propto 1/D_n$). We proposed an approach [26] to use an extrinsic 2D material, in which quantum confinement in the material plane causes a step-like DOS with a separation of E_{cs} as shown in Fig. 3.1. We further found that this effect is enhanced when inelastic scattering is the dominant mechanism. Then by shifting the onset of inelastic scattering, a window-shaped TDF is

achieved as illustrated in Fig. 3.1. The delay in onset of scattering (Γ^{inel}), where $\Gamma^{inel} \propto$ $D_n(E+E_{ph})$ (since emission is dominant and E_{ph} is the energy of phonon being emitted), the product results in a rectangular function. This, in addition to quadratic nature of v^2, gives a window shape for TDF. To simultaneously improve Seebeck and conductivity, the Fermi window should coincide with the TDF. Maximizing this overlap of the half window of 5 kT around E_f requires TDF to be 5 kT wide and $E_F \cong 0$. Using this approach, we showed a peak enhancement [26] in S at low temperatures in an inversion layer created by confinement that has a step-like DOS.

Here we extend our approach to intrinsic 2D materials and formulate selection rules that can be used to shortlist candidates with potentially higher power factor. As discussed above, the important components to be optimized are TDF (which include $\tau_n(E)$, $D_n(E)$, and $v(E)$) and Fermi window. Table.1 tabulates the contributing factors for TDF in two different band profiles possible in 2D regime i.e., a Dirac material (like graphene) and a semiconducting material (like MoS_2). The electronic band structure of Dirac material can be defined using massless Dirac equation with a Fermi velocity of v_F, and for a semiconducting 2D material effective mass approximation (effective mass of m_n^*) with spherical bands is used. This results in massless DOS for Dirac material, and an effective mass dependent DOS for semiconducting material with a band degeneracy of g_n^v. Also, $v(E)$ is constant for Dirac materials and quadratic in nature for semiconducting material.

The scattering of carriers especially from phonons determines the relaxation time (τ_n) used to calculate TDF. Carrier scattering from phonons can occur in two forms: elastic and inelastic scattering. Elastic scattering, where there is little or no change in the energy of carriers. Acoustic phonons generally participate in such elastic scattering due to their low phonon energy. The elastic scattering depends on $D_n(E)$ of the band and a pre-factor Γ_0, which is proportional to deformation potentials (Ξ_0). On the other hand, inelastic scattering involves emission or absorption of phonons by carriers, resulting in the change of their energy. Controlling the relative strength of these two processes helps in achieving the win-

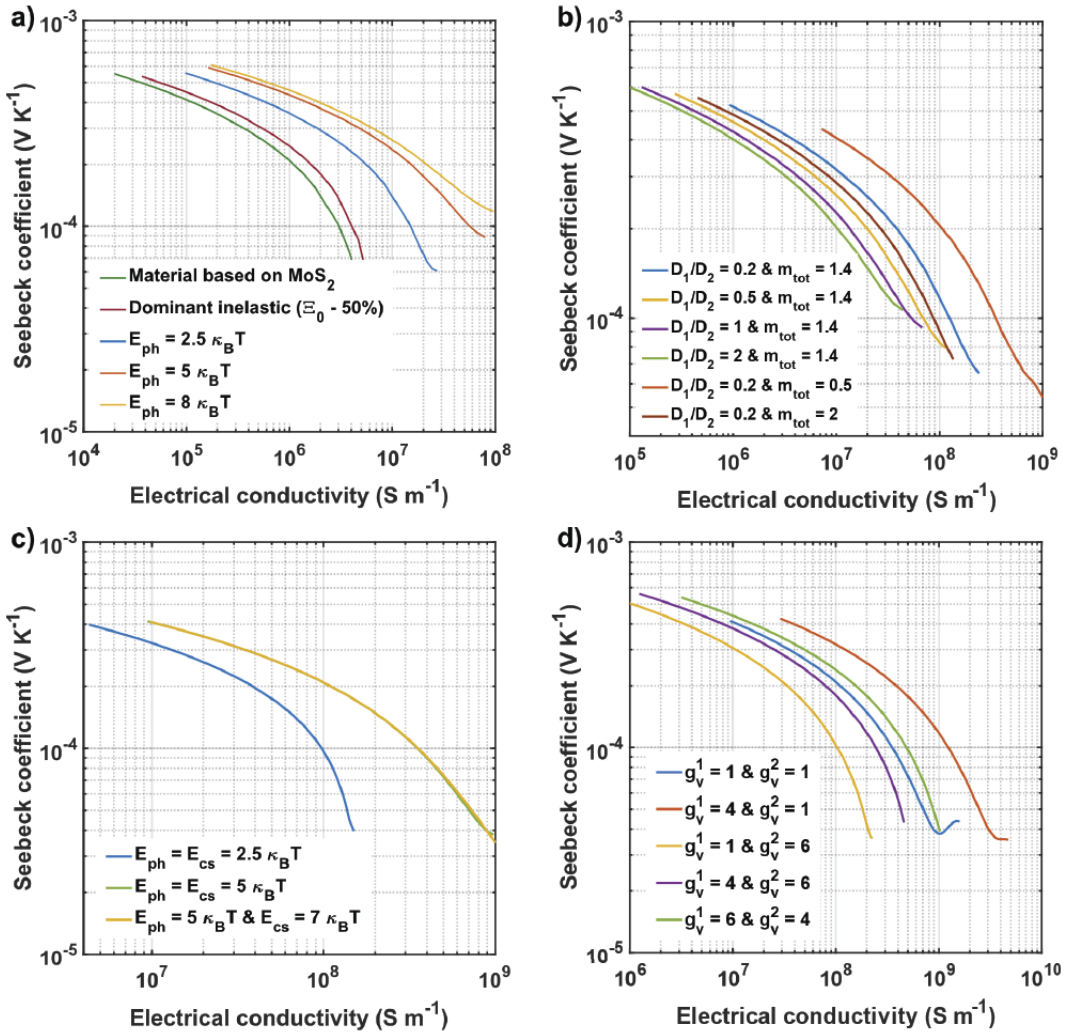

Figure 3.2: Material features identified in this study that can improve the power factor and their effect on power factor. (a) Effect of inelastic dominant material and the corresponding phonon energy (E_{ph}) on power factor enhancement. (b) Power factor is calculated by changing the total DOS and relative height difference (D_1/D_2) in DOS of valleys. (c) Matching the valley splitting (E_{cs}) and phonon energy (E_{ph}) to 5 kT maximizes the power factor along with the Fermi utilization. (d) Valley degeneracy (g_n^v) and its effect on power factor of the material. Higher degeneracy in lower valleys maximize the power factor.

dow shape for TDF. Δ_1 (for emission) and Δ_2 (for absorption) are used to make sure that the energy conservation is achieved in inelastic scattering. As shown in Table. 1, inelastic scattering in 2D materials can occur in the form of intervalley and intravalley transitions. In Dirac materials, inelastic scattering from both intravalley and intervalley is proportional to the ratio of initial and final $D_n(E)$. While in a semiconducting material, intravalley scatter-

ing is independent of $D_n(E)$, but intervalley scattering has the same dependence as a Dirac material. The linear DOS and a constant $v(E)$ in Dirac material results in a linear TDF instead of a window shape for TDF. The bipolar nature of the transport in Dirac materials due to the absence of bandgap results in low power factor. Hence, rest of the analysis is focused on semiconducting 2D materials.

Consolidating the variables to be analyzed, we divide them into two categories: parameters that control (a) the width and (b) the height of the TDF. The width of the TDF depends on the shift in the onset of inelastic scattering, which can be tuned by phonon energy (since $\Gamma^{inel} \propto D_n(E \mp E_{ph})$). To introduce this inelastic dominance, elastic scattering is suppressed using the prefactor Γ_0. In addition to step-like DOS and E_{ph}, the separation between valleys (E_{cs}) also determines the width of TDF as shown in Fig. 3.1. Along with controlling the width of TDF, E_{ph} and E_{cs} help to maximize the Fermi window utilization. $D_n(E)$, which depends on the effective mass m_n^* and band degeneracy g_n^v, controls the height of TDF. In addition to that, the inelastic scattering of carriers depends on the ratio of initial and final state DOS (D_i/D_f). Here, to effectively understand the effect of D_i/D_f the total DOS ($\sum_n D_n$) is kept constant using $m_{tot} = \sum_n m_n^*$. Now using these parameters to tune the power factor, model uses MoS_2 [127] as prototype material (where E_{cs} = 70 meV, E_{ph} = 47 meV, g_v^1 = 4, g_v^1 = 6, m_{tot} = 1.4, D_1/D_2 = 0.8) and isotropic circular valleys are assumed for conduction band. We use this prototype material to vary the material parameters and find the optimum combination for a 2D material that can provide high power factor.

3.2.1 Dominant inelastic scattering and E_{ph}

To obtain the window-shaped TDF by shifting the onset of scattering in a material, inelastic scattering should be dominant. Here we achieve this indirectly by reducing the elastic scattering by 50% using Γ_0. This results in an improvement in power factor as shown in Fig. 3.2(a) (further the S vs σ curve extends higher the power factor), mainly due to the increase in σ. The onset of inelastic scattering to create a window-shaped TDF and

to maximize the Fermi window utilization can be shifted by changing the phonon energy that participates in transport. By increasing the energy (E_{ph}) of phonons that participate in inelastic scattering a maximum in power factor is observed when E_{ph} = 5 kT. Any increase in E_{ph} further resulted in little or no improvement in power factor. This is a consequence of better overlap of window-shaped TDF and Fermi window (which has a half width of 5 kT).

3.2.2 D_1/D_2 and m_{tot}

Once a window shape for TDF is achieved in the material with E_{ph} = 5 kT, the DOS is tuned to further improve the height of TDF. By keeping the m_{tot} constant, the ratio of D_1/D_2 is varied. As seen in Fig. 3.2(b), a lower D_1/D_2 results in higher power factor. This shows that the higher separation between D_1 and D_2 is desirable to maximize power factor. Now by keeping D_1/D_2 constant, the m_{tot} is varied and a lower m_{tot} gives higher power factor. Lower effective mass reflects higher velocity of carriers that improve the height of TDF function (TDF $\propto v^2$). This requirement has already been established in 3D materials, but it applies to 2D materials as well.

3.2.3 Valley splitting (E_{cs})

Our approach tries to create a rectangular shape for the product of relaxation time (τ_n) and DOS (D_n) using the step-like DOS. The valley splitting (E_{cs}) controls the width of first step, which in turn decides the width of TDF. We already know that the ideal shift in the onset of scattering occurs when E_{ph} = 5 kT. Now by further matching this with the width of the first step (when $E_{cs} = E_{ph}$), transport can be effectively restricted to first step or valley. By calculating the power factor in an inelastic dominant 2D material with D_1/D_2 = 0.2 and m_{tot} = 0.5 when varying the valley splitting, a maximum is observed when $E_{cs} = E_{ph}$ = 5 kT as shown in Fig. 3.2(c). Further increase in E_{cs} beyond 5 kT by limiting E_{ph} to 5 kT, doesn't help since the width is limited by E_{ph}.

3.2.4 Valley degeneracy (g_n^v)

Till now, we studied the effect of different material parameters on power factor assuming the degeneracy of the valleys to be 1 (circular valleys). Now to study the effect of valley degeneracy, g_n^v is varied but D_1/D_2 is still maintained at 0.2 by adjusting the m_n^*. As shown in Fig. 3.2(d), high valley degeneracy for D_1 (the valley that contributes to transport the most) improves the power factor. However, a higher degeneracy for the secondary valley deteriorates σ, thereby reducing the power factor. This is due to the availability of more states in second valley (high degeneracy) to scatter into from first valley.

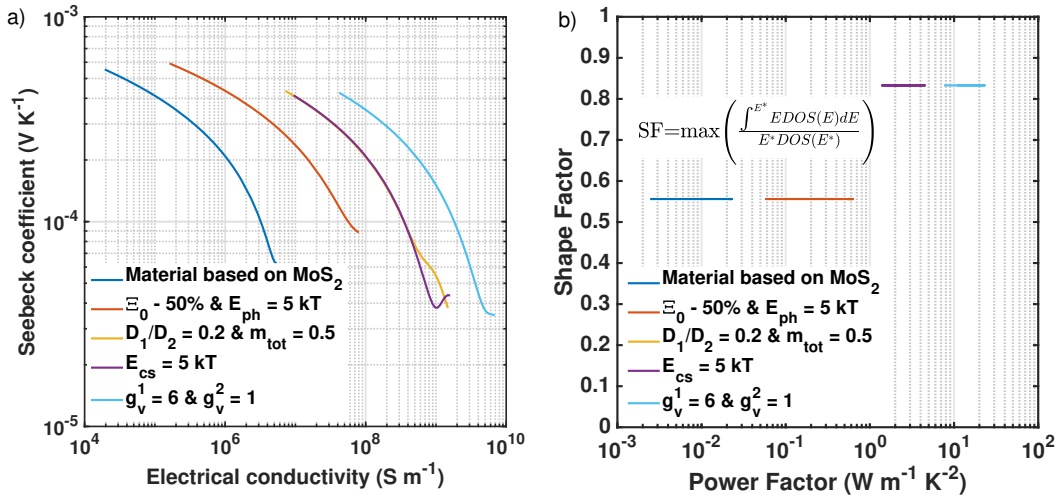

Figure 3.3: (a) The power factor enhancement achievable by tuning the material by including the features identified in this study. By introducing these features there is two orders of improvement in the power factor of MoS_2. This shows that any highly degenerate 2D material with high effective mass, low D_1/D_2 and valley splitting of 5 kT improves power factor. Power factor will be further boosted if transport is dominated by inelastic scattering mechanisms with phonon energies of 5 kT. (b) Shape factor is calculated for the material features identified in this study to show the power factor enhancement achievable that is not reflected in the shape factor.

Fig. 3.3(a) shows the step-by-step contribution from each material selection criteria proposed here that can be achieved or maximum achievable power factor enhancement. To compare the material selection criteria with already defined metrics, shape factor (SF) is calculated by introducing the features identified in this study (as shown in Fig. 3.3(b)). Observing the SF values, shows the inability of SF to predict the power factor enhancement

seen here. Since SF is only controlled by the asymmetry in the DOS, it won't be able to completely capture the changes that occur in TDF. Here, SF is only affected by D_1/D_2 and increases when D_1/D_2 is reduced. Using only SF as a selection criteria will result in a broad spectrum of 2D materials due to their intrinsic step-like DOS. Hence there is a need to look beyond SF for the features like the ones identified in this study, that can be used as material selection rules for 2D materials for better power factor prediction. Using the simple transport model as described here along with the recent development of 2D databases [128] that are comprehensive, identifying higher power factor materials can be done in a faster pace.

3.3 Conclusion

In conclusion, the search for new highly efficient thermoelectrics requires the corresponding materials used to have a high power factor. Here, a novel approach is proposed to ease the process of this material search using selection rules that ensure high power factor. A simple model based on effective mass approximation is implemented for 2D semiconducting material where inelastic scattering is dominant along with step-like DOS and by shifting the onset of scattering along with maximizing the Fermi window utilization. Our simulations show such inelastic dominance (elastic processes are suppressed) with phonon energy (E_{ph}) of 5 kT improves the power factor. Also, a further enhancement is possible if the separation between the DOS of valleys is large (lower D_1/D_2), lower effective mass, and higher degeneracy for the conduction band valley that participate in the transport. By introducing this combination of material features in our prototype material MoS_2, the power factor is boosted from 0.044 $Wm^{-1}K^{-2}$ to 22 $Wm^{-1}K^{-2}$, which is an increase of two orders in magnitude. We believe the material selection rules formulated here can help researchers to reduce the time and resources in the process of predicting and preselecting 2D materials that have high power factor. In future, these selection rules can be applied to 2D material database like Computational 2D Materials Database (C2DB) [128] to search for possible

high power factor materials. Further using machine learning algorithms and training on the existing material TE properties data (using methods based on first principles and BTE) can help to understand the properties (features) of materials that contribute to the TE performance. Using these machine learning models one can predict the TE performance using basic material properties without the need to simulate the transport in the material.

CHAPTER 4

ENHANCEMENT OF SEEBECK COEFFICIENT IN RAPID SPATIALLY VARYING PERIODIC STRUCTURES USING WIGNER FORMALISM

Past the discovery of graphene, focus has been shifted to 2D materials that possess extraordinary properties. One of such properties that can help in fabricating good TE devices is power factor. Identifying new 2D materials with high power factor can be a tedious task, both in terms of fabrication and expensive atomistic simulations. Other way is to tune the existing 2D materials by introducing the potential barriers that can act as energy filters that can boost the power factor. Multilayer thermionic devices are proposed like TMDs [109] and hexagonal boron nitride [129] sandwiched between graphene electrodes that can achieve high efficiency. Because of the weak van der Waals interlayer interaction in vertically stacked 2D heterostructures, the electrical transport is deteriorated. Recent achievements in growth of 2D lateral heterostructures and superlattices provided new direction for TE devices [129, 13]. Lateral heterostructures created from TMDs showed promising increase in the ZT [106]. These heterostructures can have single and multi-barrier structures. In single barrier devices, an optimum height barrier is used in one direction and a large barrier is used in other direction to prevent the reverse current. In multibarrier barrier devices, Mahan and Woods [130] suggested an improvement by a factor by two but later concluded that it worse than the normal devices. Seebeck enhancement by hot electron filtering is observed in some systems [31], but this comes with a decrease in electrical conductivity because of reduced number of carriers.

Recent achievements in the growth of lateral (in-plane) 2D heterostructures and superlattices provide a new direction for TE devices [129, 131, 132]. Depending on the direction

of applied electric field relative to the potential barriers created by interfaces in the heterostructure, carriers experience either confinement or energy filtering, both of which can be beneficial to TE properties. In addition to striped heterostructures [133], lateral potential barriers can be also realized in 2D materials by periodically modulating the bandgap through one of several ways, including applying local strain [134] and wrinkling [135], varying the local alloy composition [136], or patterning the substrate to very its dielectric screening [137]. Such lateral heterostructures created from TMDs have shown promising increases in the ZT [138] but research so far has focused primarily on the lattice thermal transport [139]. However, a unified framework to assess the extent of possible enhancement, the influence barrier shape and size on TE performance, and the anisotropy between transport in the directions parallel and perpendicular to the barriers is still lacking.

The general interpretation of the carrier transport over the barriers is that the electron with higher kinetic energy perpendicular to the barrier is emitted. Many hot electrons with higher transverse momentum are unable to overcome the barrier. To break this, non-planar barriers or scattering centers are created [140]. Moreover, the effect of barriers on the distribution function of the particles is not considered. If the non-planar or the scattering centers have a characteristic length less than electron de Broglie wavelength, then wave nature of the electron has to be considered which makes the problem complex to analyze. Even though simulating the TE parameters in superlattice or heterojunction is done previously [36, 27], they lack comprehensive treatment of electron scattering. In our previous work [5], we showed the impact of the barrier shape of such sharp potentials in silicon (bulk and a square wire) and concluded that sharp, tall barriers with small periods result in better TE performance. Our model captures the carrier-potential interactions in the Wigner formalism as an additional force term (quantum evolution operator) along with the semiclassical Boltzmann transport equation (BTE). The resultant Wigner-Boltzmann transport equation is solved using Rode's iterative method [141, 142]. We then studied the impact of height, width, and shape (smoothness) of the potential barrier on TE properties.

Even though Wigner formalism allows us to include quantum effects, there are limitations to its use in quantum device modeling. TE applications, unlike their device counterpart, require longer systems that are made of nm-thick layers, which can be considered periodic, akin to the earlier work on quantum cascade lasers [143].

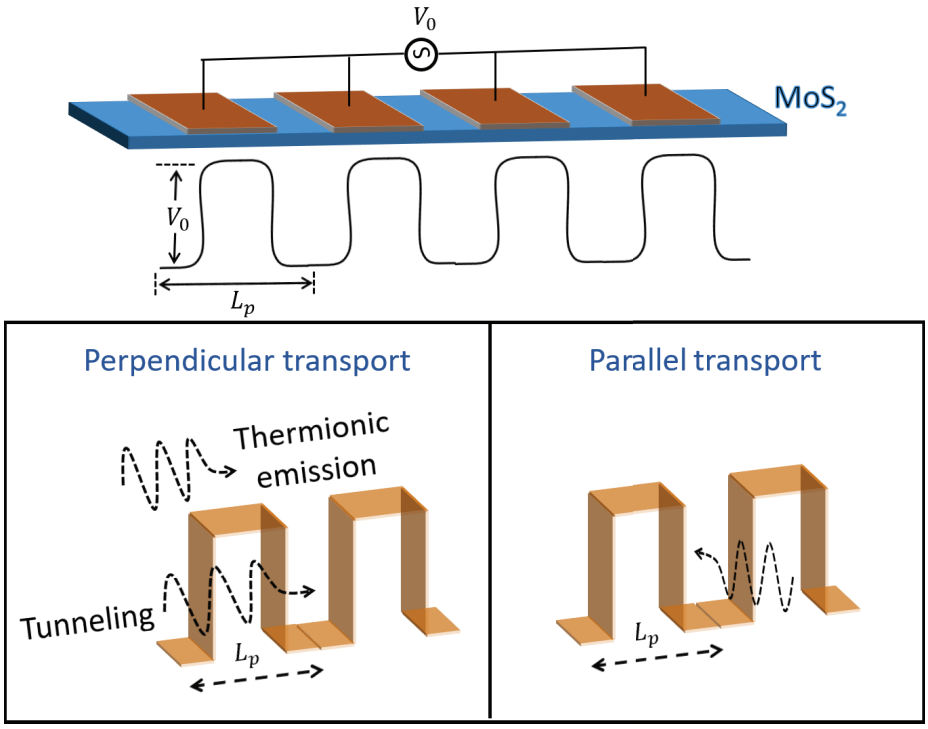

Figure 4.1: Schematic of the simulated structure to study energy filtering in SL MoS_2 with a series of spatially varying potential barriers. Here the effect of potential barriers on electron transport with electrons flowing into the barriers (perpendicular transport) and flowing parallel to the potential well (parallel transport) are studied.

Here we study the anisotropic transport in 2D materials, focusing on the transition metal dichalcogenide (TMD) MoS_2 as a prototype. We introduce a series of potential barriers, as shown in Fig. 4.1, to establish the extent of possible gains in TE power factors and elucidate the conditions required for achieving them. If the direction of the field is perpendicular to the barriers (perpendicular transport), they undergo energy filtering and, depending on the features of the barriers, a combination of thermionic emission and tunneling is possible. Conversely, when the electric field is parallel to the barriers (parallel

transport), the band offsets can confine the carriers by forming potential wells. Extending our previous 3D Wigner-Rode model [5] to 2D materials, we calculate the conductivity and Seebeck coefficients in both parallel and perpendicular directions in the presence of smooth or sharp potential barriers. We study the effect of their shape, height, and smoothness on the resulting TE performance and quantify the relative enhancement due to the barriers. Our simulations show higher power factors are realize for transport parallel to the potential barriers than perpendicular transport across them. We find that parallel transport is influenced by confinement while perpendicular transport is dominated by energy filtering and can result in the reduction of the power factor, especially with sharp square barriers.

4.1 Rode's method for solving Boltzmann transport equation

To model the electron transport by solving the Boltzmann transport equation (BTE), Rode 's method can be used. Rode's method [142] is an iterative method to calculate electronic characteristics of a material by solving for perturbation to the distribution function due to the applied field. Then this perturbation is used to calculate electrical transport parameters like the Seebeck coefficient, electrical conductivity, electron thermal conductivity etc. The collision operator in BTE (Eq. 1.4) includes the evolution of the particles from scattering mechanisms. This evolution caused by the perturbation in the distribution of carriers can be obtained easily in the absence of any inelastic processes using RTA approximation (Eq. 1.5) for collision operator in BTE. In the presence of dominant inelastic scattering process, the concept of RTA is not accurate as the distribution of carriers doesn't relax to their equilibrium distribution.

In Rode's method, the accuracy of the solution to BTE is improved by including contributions from inelastic scattering processes, especially the in-scattering. This is achieved by splitting the BTE collision integral into two separate terms—the in-scattering and the out-scattering. To do that the distribution function is approximated to first order using Legendre polynomials

$$f(k) = f_o(k) + \sum_{n=1} g_n(k) p_n \left(cos(\theta)\right) \tag{4.1}$$

where $f_o(k)$ is equilibrium distribution function, $g_n(k)$ is the perturbation to the distribution function due to the applied electric field and θ being the angle between carrier velocity and electric field. The collision term in Eq. 1.4 can be written as sum of contribution from elastic and inelastic scattering processes.

$$\left(\frac{\partial f}{\partial t}\right)_{coll} = \left(\frac{\partial f}{\partial t}\right)^{el}_{coll} + \left(\frac{\partial f}{\partial t}\right)^{inel}_{coll} \tag{4.2}$$

Including both in-scattering and out-scattering processes of inelastic scattering mechanisms, its contribution can be written as

$$\left(\frac{\partial f}{\partial t}\right)^{inel}_{coll} = cos(\theta)\left[I(k) - g(k) I_o(k)\right] \tag{4.3}$$

$$I(k) = \sum_{k'} g(k') cos(\alpha) \left[S^{inel}_{kk'} f_0 + S^{inel}_{k'k}(1 - f_0)\right] \qquad \text{in-scattering processes} \tag{4.4}$$

$$I_o(k) = \sum_{k} \left[S^{inel}_{k'k} f_0{}' + S^{inel}_{kk'}(1 - f_0{}')\right] \qquad \text{out-scattering processes} \tag{4.5}$$

and the contribution from elastic mechanisms can be written as

$$\left(\frac{\partial f}{\partial t}\right)^{el}_{coll} = \frac{g(k) cos(\theta)}{\tau^{el}(k)} \qquad \text{outscattering processes} \tag{4.6}$$

where α is the angle between the initial and final wavevector, $S_{k'k}$ is the scattering rate from k' to k, f_0 is the Fermi-Dirac distribution of corresponding wavevector and $\tau^{el}(k)$ is the elastic processes relaxation time. Substituting Eq. 4.2 in Eq. 1.4, perturbation in distribution can be written as

$$g_{i+1}(k) = \left(I(k) + \frac{eF}{\hbar}\frac{\partial f_0}{\partial k} - v(k)\frac{\partial f}{\partial r}\right) \Big/ S_0(k) \ . \tag{4.7}$$

$$\text{where} \qquad I(k) = \sum_{k'} g_i(k') cos(\alpha) \left[S^{inel}_{kk'} f_0 + S^{inel}_{k'k}(1 - f_0)\right] . \tag{4.8}$$

S_0 is the sum of out-scattering rates of all processes and in-scattering rates of all scattering mechanisms except inelastic mechanisms. Here the i^{th} iteration solution of g_i is used to calculate the $(i+1)^{th}$ solution of the perturbation to the distribution function and the process is continued till it converges. The iteration is started from an equilibrium distribution, such that the initial in-scattering term is zero and the first update is straightforward to compute. A general Jacobi iteration is implemented to solve for $g(k)$ in Eq. 4.7, along with successive over-relaxation (SOR) to achieve better convergence. The calculated perturbation ($g(k)$) to distribution function is used to calculate transport distribution function (TDF) as

$$\sigma(E) = \frac{1}{\Omega(2\pi)^2 F} \int v(k) g(k) \delta(E - E(k)) d^2k \tag{4.9}$$

where $v(k)$ is group velocity of carriers, Ω is the volume of the first Brillouin zone, and F is applied electric field. We can recover the widely-used relaxation-time-approximation (RTA) solution of the BTE by substituting the zeroth-iteration solution of the perturbation $g_0(k) = eFv(k)\tau(k)\left[\partial f_0(E)/\partial E\right]$. Here, $\tau(k)$ is the relaxation time, which is the inverse of total out-scattering rate $S_o(k)$ in the RTA. Once the iteration reaches convergence, as measured by the norm of the difference between successive iterations, S and σ are calculated from the TDF using Eq. 1.6 & Eq. 1.7.

4.2 Rode's implementation of the Wigner Boltzmann transport equation

Next, Rode's approach is applied to solving the WBTE by adding the Wigner potential contribution representing the additional forces arising from the potential variation in the structure. Then, the resultant perturbation to the distribution function in Eq. 4.7 can be modified as

$$g_{i+1}(k) = \left(I(k) + \frac{eF}{\hbar}\frac{\partial f_0}{\partial k} - v(k)\frac{\partial f}{\partial r} + Q f_w \right) \Big/ S_0(k) \; . \tag{4.10}$$

In this thesis, an extensive study of effect of rapid varying periodic potentials of different periodicity and shape is done. The reason for a rapid varying periodic potential is to limit position dependence and complexity of solution of the potential operator or quantum evolution term at a fixed position for a single electron packet. To study the effect of periodic potential structure (shape and size), a square barrier with smoothening parameter β and a smooth cosine shaped potential barrier are used. A generalized potential that is spatially periodic can be represented as

$$V(r) = \sum_{n=-\infty}^{\infty} V_p(r - nL_p). \tag{4.11}$$

The quantum evolution (Eq. 2.3) (derived in Appendix B of [5]) of this generalized form for periodic potentials is

$$Qf_w = \sum_{m=1}^{\infty} W_m(r) \left[f_w\left(r, k - \frac{m\pi}{L_p}\right) - f_w\left(r, k + \frac{m\pi}{L_p}\right) \right]. \tag{4.12}$$

The quantum evolution force for square barriers,

$$V_p(r) = \frac{V_0}{2} \left\{ -erf[\beta(r-a)] + erf[\beta(r+a)] \right\} \tag{4.13}$$

of height V_0 with smoothening factor β and width $2a$ or $L_p/2$ is (refer to Appendix B for derivation)

$$W_m(r) = \frac{2V_0}{\pi\hbar m} e^{\frac{-m^2\pi^2}{\beta^2 {L_p}^2}} \sin\left(\frac{2\pi m a}{L_p}\right) \sin\left(\frac{2\pi m r}{L_p}\right). \tag{4.14}$$

In perfectly smooth potentials, a cosine shaped potential $V_q(r) = A\, cos(K_0 r)$, (applied in r direction) where $K_0 = 2\pi/L_p$ has a simple quantum evolution as it has single order Wigner potential which is calculated using the Eq.2.4 (detailed derivation is shown in Appendix B)

and the quantum evolution in Eq. 2.3 for cosine potential is obtained as (refer to Appendix B for derivation)

$$Qf_w = W_m(r)\left[f_w\left(r, k - \frac{K_0}{2}\right) - f_w\left(r, k + \frac{K_0}{2}\right)\right] \tag{4.15}$$

$$\text{where} \qquad W_m(r) = \frac{A\, sin(K_0 r)}{\pi\hbar} \tag{4.16}$$

It should be noted that the quantum evolution force for a smooth potential is the first order approximation (m=1) to the quantum evolution force of a square barriers (Eq. 4.12).

The solution for the perturbation $g(k)$ to distribution function (Eq. 4.10) in WBTE can now be used to study the thermoelectric behavior of the system. The Wigner distribution function used in above formulations to calculate the quantum evolution term can be written as

$$f_w\left(r, k, t\right) = f_0\left(r, k, t\right) + g_w\left(r, k, t\right) \tag{4.17}$$

which is the sum of equilibrium distribution function from Fermi-Dirac statistics, and perturbation to distribution due to the electric field and rapid potential variation (as shown in Eq. 2.7). This shows the nonlinearity of WBTE, hence using the Rode's iterative method the perturbation distribution is evaluated at i^{th} iteration and then the quantum evolution for $(i+1)^{th}$ is calculated as shown in Eq. 4.10 with solution of i^{th} iteration. This process can be repeated till convergence is achieved.

4.3 Implementation of Transport Model

Rode's approach of Wigner-Boltzmann transport formalism is implemented in single layer MoS_2 which is used here as a prototypical gapped 2D material. To maintain a more realistic approach to the implementation, the full band structure of MoS_2 is used for modeling the thermoelectric properties. The electronic structure of MoS_2 used in this study is calculated from first principles using self-consistent density functional theory (DFT) calculations with the open-source software Quantum-Espresso [144]. For MoS_2, we used a non-

relativistic norm-conserving pseudopotential (NCPP) for molybdenum (Mo) and a scalar relativistic NCPP for sulfur (S). The potentials employed a Martins-Troullier method with a Perdew-Wang (LDA) exchange correlation. The lattice constant of MoS_2 used here is a = 3.125 Å and z = 3.11 Å, where z is the SS distance. Planes of atomic monolayers of MoS_2 are separated by a 20 Å vacuum to calculate the monolayer band structure and a cutoff energy of 140 Ry is used. A convergence threshold of 10^{-16} is implemented for initial total energy calculation on a MonkhorstPack grid sizes of $6 \times 6 \times 4$. Using the central difference method, the group velocities in each band ($v(k)$) are obtained to calculate the transport properties.Then the density of states (DOS) is calculated using the Spherical averaging method (SAVE) [145]. Then the scattering rates are calculated from the band-structure and the density of states.

The scattering rates that are covered in this model are elastic acoustic deformation potential phonon scattering and Fröhlich scattering. Also, inelastic intervalley optical phonon scattering (f-type and g-type processes)(refer to Appendix A for the expressions). Using the electron-phonon deformation potentials determined from first principles [127]. An acoustic deformation potential of 2.1 eV is used for longitudinal acoustic (LA) phonons and 5.2 eV for transverse acoustic (TA) phonons. For inelastic scattering, an optical phonon deformation potential of 2.6×10^8 eV cm^{-1} for longitudinal optical (LO) phonons with a phonon energy of 48 meV. A deformation potential of 4.1×10^8 eV cm^{-1} is used for homopolar phonons with a phonon energy of 50 meV. A coupling constant of 98 meV is used for Fröhlich (LO) interactions. Once scattering rates are calculated, then the drift component of Eq. 4.10 is calculated. The model in this dissertation is written for a single period length of the potential (either cosine shaped or general square potential). The length of the material along with the rapid varying potential is discretized for the simulation. Then the quantum weight $W_m(r)$ is calculated at every point in the grid, from where the convergence for g_i is started.

As Rode's method uses in-scattering of the inelastic mechanisms for calculating the perturbation in distribution function, it has to be implemented carefully. For any band the inelastic mechanism used here i.e., intervalley optical phonon scattering, can have the in-scattering contributions from other three branches and from the same branch. To include this we again used the spherical averaging method [145] to calculate $I(k)$. For example, for f-type emission the $I(k)$ is calculated using SAVE method with $\Lambda_{inems}\left(k'\right) g_i\left(k'\right)$ as an weight using Eq. A.6 and Eq. 4.8, where DOS is written as $\int dk\, \delta(E - E(k))$. So,

$$I(k) = \int dk' \Lambda_{inems}\left(k'\right) g_i\left(k'\right) \delta(E_i + \hbar\omega_0 - E(k')) \tag{4.18}$$

where the $E(k')$ is the band from which the carrier scatters to the band E_i. g_i is the perturbed distribution function of the i^{th} iteration and $\hbar\omega_0$ is the optical phonon energy. The coefficient Λ_{inems} for a f-type intervalley scattering can be written as using Eq. A.6 as

$$\Lambda_{inems} = \frac{e\left(N_0 + 1 - f\left(k\right)\right)(Z-2){D_0}^2}{\rho\omega_f} \tag{4.19}$$

where N_0 is phonon Bose-Einstein distribution, $f\left(k\right)$ is the Fermi-Dirac statistics for electron., D_0 is the optical coupling potential for f-type processes, Z is the degeneracy of silicon, ρ is density and ω_f is the frequency of f-type phonons. This method is used to calculate the in-scattering contribution from intervalley optical phonon scattering by both f and g processes for a band from other three bands and from itself. S_0 in Eq. 4.7 is calculated as follows:

$$S_0 = S_{acs} + S_{imp} + S_b + S^o_{iop} \tag{4.20}$$

S_{acs} is deformation acoustic phonon scattering rate, S_{imp} is impurity scattering rate, S_b is the boundary scattering rate and S^o_{iop} is out-scattering rate of inelastic intervalley phonon scattering. To evaluate the contribution from rapid varying potential in Eq. 4.15 and 4.12, the k vector displaced $g_i(k^+)$ and $g_i(k^-)$ is calculated by interpolating $g_i(k)$.

4.4 Power factor

To validate our model's ability to reproduce the intrinsic behavior, we calculated TE parameters for SL MoS_2 without any potential barriers. Figure 6.2(a) shows the dependence of Seebeck coefficient (solid) and conductivity (dashed lines) on carrier concentration in intrinsic MoS_2 at temperatures of 100 K, 200 K, 300 K, and 400 K. Solid lines in Figure 6.2(b) show the calculated power factors corresponding to Figure 6.2(a) and the maximum is observed at a carrier concentration of 7×10^{12} cm^{-2} at room temperature and below. Beyond this value, the power factor drops, which can be traced back to both Seebeck coefficient and mobility (dashed lines in Fig. 6.2(b)) degrading at high carrier concentrations. Comparing our results with experimental measurements [146], there is good agreement in Seebeck coefficient of intrinsic MoS_2. The power factor calculated here is slightly higher than experimental measurements because we focus on phonon-limited carrier transport, resulting in higher electrical conductivity than the measurements, which likely included some scattering from charged impurities. Our simulations show a peak power factor of 23 $mWm^{-1}K^{-2}$ at 300 K whereas experimental measurements show a peak power factor of 0.15 $mWm^{-1}K^{-2}$ [147] and 5 $mWm^{-1}K^{-2}$ [146]. In this study, we assume field-effect (electrostatic) doping by a series of gates, so carriers do not experience ionized impurity scattering from dopants, resulting in higher electrical conductivity. The absence of ionized impurity scattering is observed in field-effect-doped TMD WSe_2 [148] in the form of higher mobility compared to Ta-doped WSe_2[149]. The mobility in SL MoS_2 is reduced five-fold due to the ionized-impurity scattering[150] when impurity density is increased from 10^{11} cm^{-2} to 10^{13} cm^{-2}. Our phonon-limited mobility values (around 400 $cm^2V^{-1}s^{-1}$ at room temperature), shown as dashed lines in Figure 6.2(b), are in good agreement with those calculated from first principles [127].

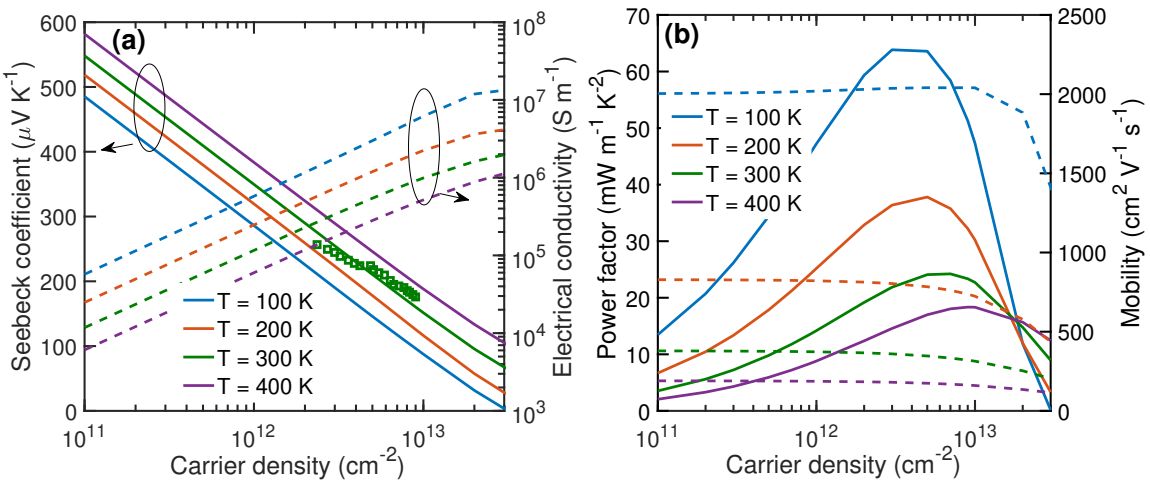

Figure 4.2: TE properties of MoS_2 calculated by varying the carrier densities of electrons at various temperatures. Seebeck coefficient and electrical conductivity are plotted in (a) by varying the carrier density. From (b), a peak in power factor (solid lines, left axis) is observed at a carrier density of around 7×10^{12} cm^{-2} at temperatures below 300 K, attributed to the drop in electron mobility (dashed lines, right axis).

4.4.1 Perpendicular Transport

Next, spatially-varying potentials are introduced into the MoS_2 and TE parameters are calculated by solving WBTE using our Wigner-Rode iterative method. Perpendicular transport is modeled after introducing both smooth and sharp barriers. Fig. 6.3(a) shows the effect of potential barrier height (V_0 - E_f) on the TE performance for both cosine (smooth) and nearly square (sharp) barriers. With an increase in (V_0 - E_f) and the absence of tunneling, S increases because of energy filtering from thermionic emission of carriers that allows only high energy electrons to flow across the barrier. This can be seen in the barriers with wide period lengths, L_p = 7 nm (irrespective of barrier shape, smooth or sharp) and in smooth barriers with short period lengths, L_p = 3 nm. When carriers are moving perpendicular to the sharp potential barriers, tunneling emerges in narrow potential barriers and results in a reduction of S (solid green line in Fig. 6.3(a)), particularly with effective barrier heights (V_0 - E_f) greater than 16 meV. This in turn allows more carriers to cross the barrier, increasing the electrical conductivity (dotted green lines in Fig. 6.3(a)) compared to wide sharp potential barriers (dotted purple lines in Fig. 6.3(a))

To better understand this behavior of S, energy-resolved $S(E)$ is plotted for both narrow and wide sharp barriers as shown in Fig. 6.3(c) and Fig. 6.3(d). In thin sharp barriers, the tunneling of the carriers is higher and can be seen in the form of low average energy of the carriers participating in the transport. Whereas wider sharp barriers are efficient at filtering the carriers and results in a larger contribution to S. Coming to the σ, conductivity decreases with the effective barrier height irrespective of the barrier shape and period length. The observed relative difference is due to the variation in the tunneling of carriers as discussed above. For sharp barriers with thin period lengths, L_p = 3 nm, this results in a reducing power factor beyond 16 meV. At wide period lengths with sharp barriers, the reduction in conductivity compensates for any gains in S which results in an overall reduction in power factor. In smooth barriers, power factor increases with effective barrier height (V_0 - E_f) and converges to 25% for thin period lengths whereas for wide barriers power factor changes almost linearly with effective barrier height.

To this point, effective barrier height (V_0 - E_f) was changed using V_0 while keeping the Fermi level constant. To understand the influence of carrier concentration N_d via the Fermi level (E_f), the barrier height is changed using E_f by keeping V_0 at 13 meV. The peak in power factor with changing the E_f is seen around $N_d = 7\times 10^{12}$ cm^{-2} (E_f = -10 meV) same as in intrinsic monolayer MoS_2. Due to the increased proportion of tunneling from lower-energy carriers around the middle of the barrier height in sharp barriers, smooth barriers have higher power factors than sharp barriers in the case of perpendicular transport.

4.4.2 Parallel Transport

The perpendicular transport simulations in MoS_2 with potential barriers helped us illuminate the interplay between tunneling and energy filtering on the TE power factor. To compare it with the influence of carrier confinement, the direction of the electric field is changed to be parallel to the barriers. In parallel transport, our simulations show sharp barriers have higher S (as shown in Fig. 4.4(a)) due to efficient carrier confinement that

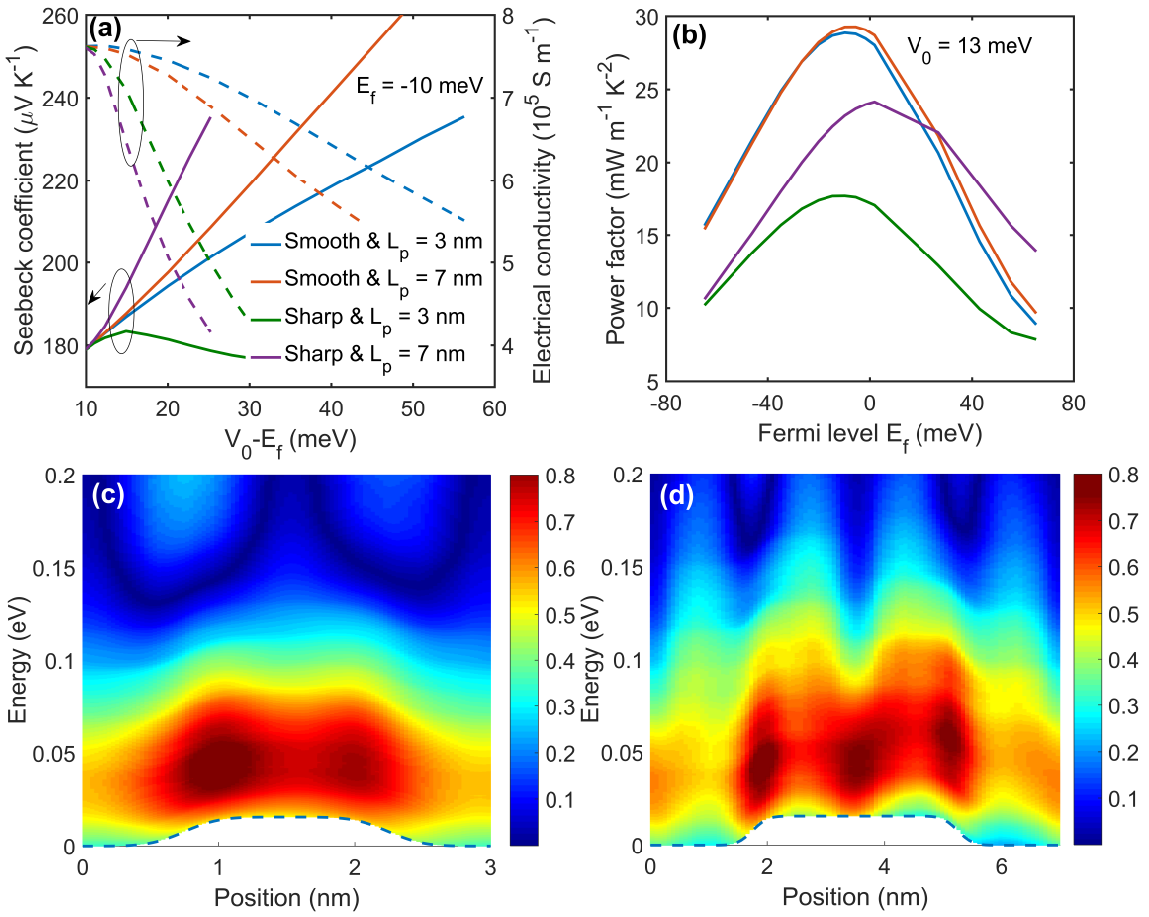

Figure 4.3: Perpendicular charge transport in presence of potential barriers at T = 300 K in MoS_2. (a) Effect of potential barrier height (V_0 - E_f) on S and σ with smooth and sharp barriers at a carrier density of $7\times\ 10^{12}$ cm^{-2}. (b) Power factor calculated by varying the Fermi level with V_0 fixed at 13 meV for the same barriers as (a). The peak in the power factor still stays at $7\times\ 10^{12}$ cm^{-2}. To understand the difference in S for sharp barriers with L_p = 3 nm (c) and L_p = 7 nm (d), energy resolved S is plotted (dotted lines represent the barrier dimensions in the material). The heat map shows the higher tunneling in sharp barriers with L_p = 3 nm that results in lower average energy for the carriers.

increases the average carrier energy. This effect is more predominant in potential barriers with thin period lengths. This confinement of carriers with the potential wells created by the barriers, effects the conductivity of carriers. σ of smooth barriers is higher than the sharp barriers and this behavior is not affected by the period length (also seen in Fig. 4.4(a)). To understand this behavior, the energy resolved conductivity is plotted using Eq. 4.9 at L_p = 3 nm for smooth (Fig. 4.4(c)) and sharp (Fig. 4.4(d)) barriers. The relatively low barrier

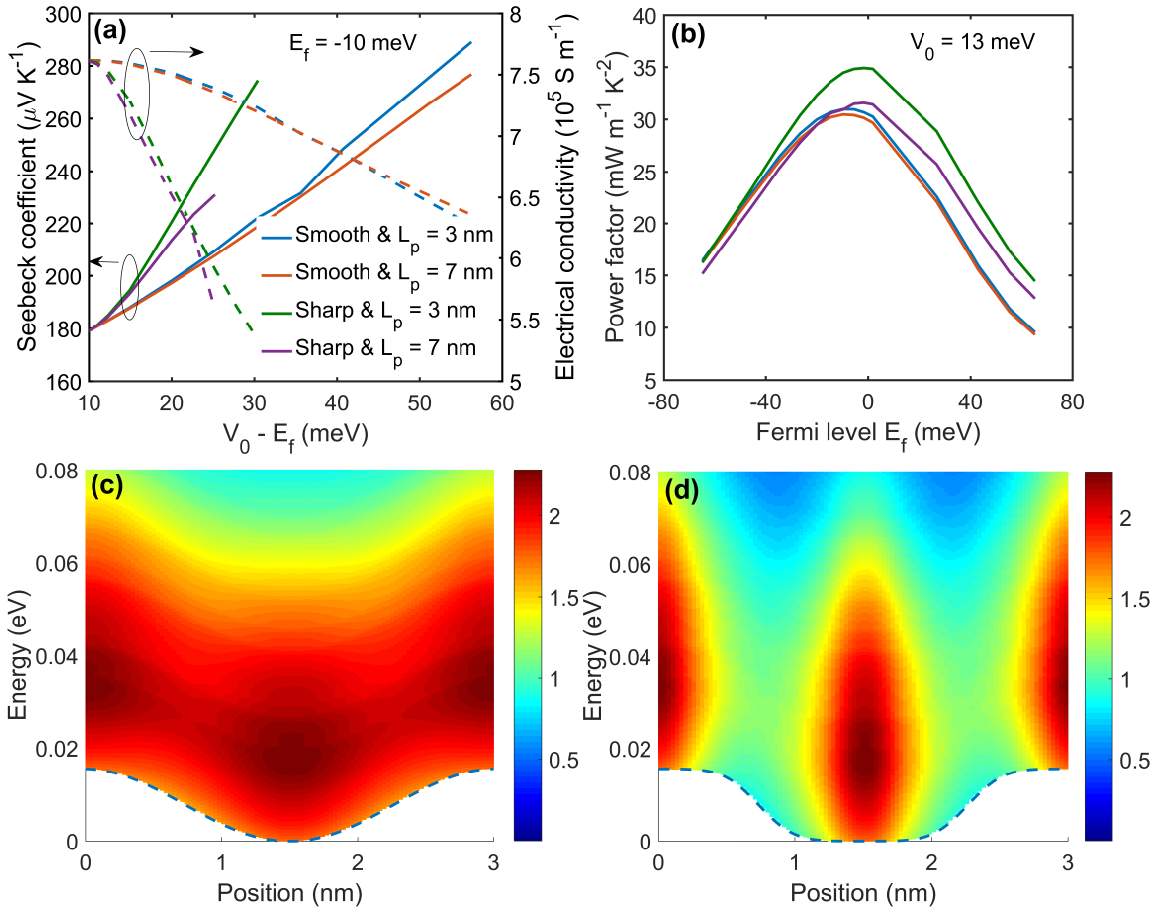

Figure 4.4: Parallel charge transport in presence of potential barriers at T = 300 K in MoS_2. (a) Effect of potential barrier amplitude (V_0 - E_f) on S and σ with smooth and sharp barriers at a carrier density of 7×10^{12} cm^{-2}. (b) Power factor calculated by varying the fermi level with the barrier height fixed at 13 meV for the same barriers as (a). The peak in the power factor is observed at V_0-E_f = 23 meV = 0.9 kT and the calculated carrier density at the peak where E_f = -10 meV is 7×10^{12} cm^{-2}. To understand the difference in σ for smooth (c) and sharp barriers (d), energy resolved σ (Eq. 4.9) is plotted (dotted lines represent the barrier dimensions in the material). Lower σ seen in sharp barriers is a result of the effective confinement experienced by carriers as shown in the heat map.

height of 0.0155 eV compared to average energy of carriers (1 k_BT = 0.0259 eV) allows for significant conduction of carriers above the potential barrier. The energy used in Fig. 4.4(c) and (d) is relative to the band edge, which follows the potential barriers. Sharp barriers confine carriers more effectively compared to the smooth barrier which can be seen in the lack of conducting channels in the presence of sharp barriers. Even though this explains

the lower conductivity in sharp barrier, the higher Seebeck coefficient translates to higher power factor in sharp barriers.

Similar to the perpendicular transport, the E_f is changed independent of V_0 which is kept constant at 13 meV. Power factor calculated for smooth and sharp barriers at different period lengths show a peak at N_d = 7$\times$ 10^{12} cm^{-2} (E_f = -10 meV), which is consistent with perpendicular transport. Also, sharp barriers outperform smooth barriers in terms of power factor and barriers with thin period lengths are more effective in confining carriers resulting in higher power factor.

4.5 Anisotropy in the TE Power Factor

To understand the anisotropy in TE properties, power factor is calculated using the perpendicular and parallel transport simulations for smooth (Fig. 6.4(a)) and sharp barriers (Fig. 6.4(b)). Parallel transport dominated by carrier confinement always results in higher power factor, which doubles from 25 $mWm^{-1}K^{-2}$ without barriers to over 50 $mWm^{-1}K^{-2}$, a record-high value exceeding those reported for graphene encased in hexagonal boron nitride (hBN) [151]. The significant increase in S compared to the reduction in σ with the barrier height coupled with the quadratic dependency of S on power factor results in power factor enhancement observed in parallel transport. The increase in the power factor in parallel transport by increasing the barrier height (V_0 - E_f) will eventually converge to the power factor of an infinite potential well. In the perpendicular transport regime, the smooth barriers outperform the sharp barriers while sharp barriers are better for parallel transport. A 25% increase in power factor can be achieved using tall smooth barriers under perpendicular transport. But tunneling in sharp barriers at thin period lengths and low conductivity of carriers at wide period lengths reduce the power factor, even below the intrinsic values. The power factor enhancement varies linearly (Fig. 6.4(a)) with effective barrier height once transport is moved in parallel with the barriers. In smooth barriers, enhancement of power factor in parallel transport is 70% higher than perpendicular transport with tall barri-

ers. This difference reaches around 300% for sharp barriers when comparing both transport regimes at low period lengths.

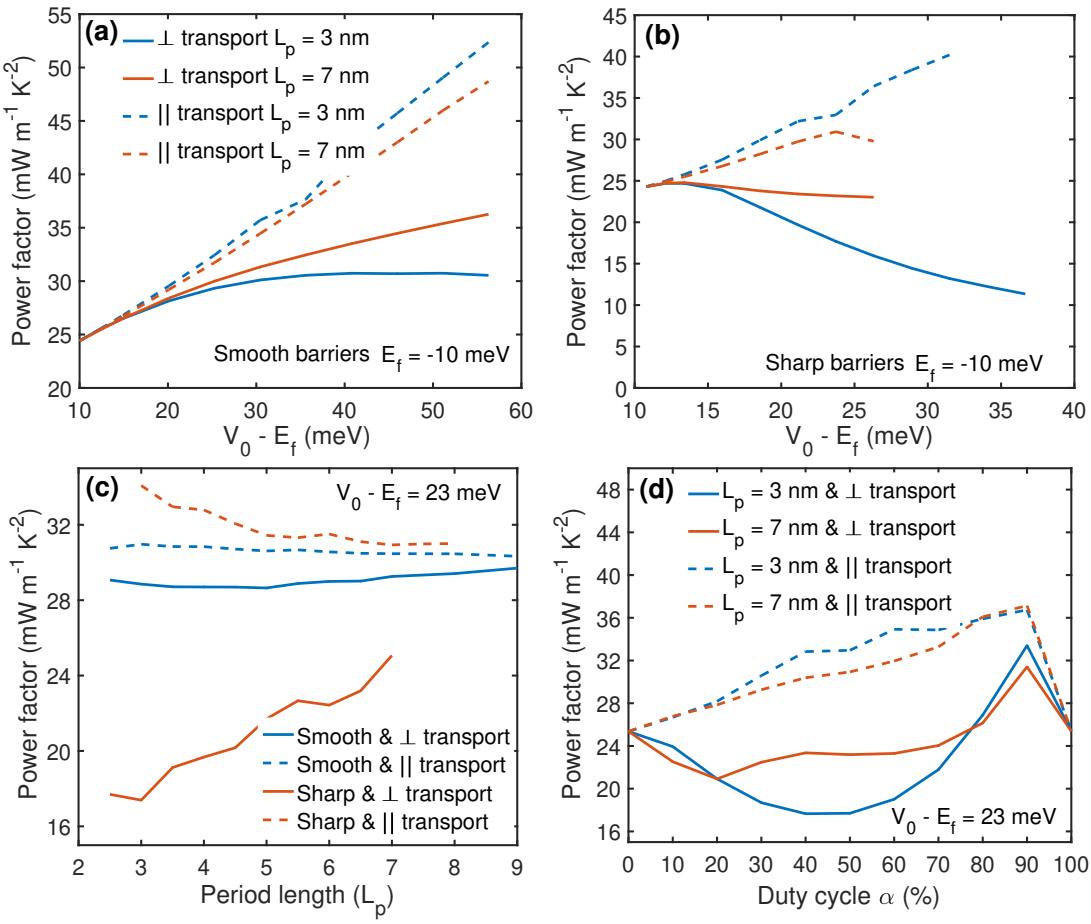

Figure 4.5: Changes in power factor of SL MoS_2 by introducing potential barriers using a series of gates. Comparison between perpendicular and parallel transport in a) smooth barriers and b) sharp barriers at different period lengths. c) Effect of period length on the power factor in smooth and sharp barriers in both the transport regimes. d) Power factor changes with the asymmetry in shape of the sharp barrier are observed by changing α.

The difference in transport mechanisms of parallel and perpendicular transport can be seen in their respective dependence on the period lengths (L_p). Fig. 6.4(c) shows the power factor calculated at different period length with effective barrier height of 23 meV for both sharp and smooth barriers. In the presence of sharp barriers where tunneling and confinement are strong, increasing L_p improves power factor in perpendicular transport and decreases in parallel transport. In perpendicular transport, where energy filtering and

tunneling impact transport, increasing L_p improves energy filtering (through thermionic emission) and reduces tunneling, resulting in an increase in power factor. Confinement of carriers in parallel transport reduces power factor with increase in L_p. This is a consequence of the higher energies of the available states that participate in transport when carriers travel through the potential wells with thin period length. These higher energies translate to higher S at thin period lengths as seen in Fig. 4.4(a), even though σ experiences no effect. Varying L_p for smooth barriers shows no change in power factor at a given barrier height.

Another sharp barrier parameter that can affect the TE performance is the duty cycle (ratio of the barrier width to the period length) of the potential barrier. To this point, all the simulations were performed by assuming a symmetric sharp potential barrier (α = 50%). By changing the duty cycle of sharp barriers, the power factor of the structure is plotted in Fig. 6.4(d). In perpendicular transport, power factor increases in sharp barriers that are asymmetric (α higher or lower than 0.5), especially barriers with lower period lengths (L_p = 3 nm). At higher period lengths, increasing α improves the power factor of the structure due to more efficient energy filtering with the wide barrier. As duty cycle (α) approaches 100%, the wells in the potential barriers disappear creating a constant potential throughout the material. This results in an intrinsic material with higher band edge which results in the difference in power factor and does not converge to the value at α = 0%. In parallel transport, asymmetry in barriers results in changing the effective potential well width. Reducing the well width raises the energy levels in the well, thus altering the resulting power factor. Hence, highly asymmetric barriers (having larger α) result in thin potential wells that produce higher power factors.

4.6 Conclusion

Improving thermoelectric efficiency of nanoscale TE devices requires a thorough understanding of carrier scattering, tunneling, and confinement. In any 2D material with spatially-varying lateral potential barriers experiences these effects depend on the direction

of the electric field with respect to the potential barrier direction. When the field is perpendicular to the potential barriers, carrier transport is affected by thermionic emission and tunneling while in the direction parallel to the barriers, carriers are confined by the change in the potential across the material. We implemented a comprehensive model based on the Wigner formalism and the Boltzmann transport equation to fully account for the influence of the potential barriers at nanoscale along with the scattering of carriers. Using electronic structure obtained from first-principles DFT calculations, we calculated TE properties of MoS_2 with lateral potential barriers and varied the shape and size of the barrier. Our results show that potential barriers result in a two-fold enhancement of power factor, from 25 to 50 $mWm^{-1}K^{-2}$, particularly with parallel transport in sharp barriers having small width. Regardless of barrier shape, carrier transport parallel to the barriers results in a factor of three enhancement in power factor compared to perpendicular transport. We observe significant anisotropy as smooth barriers outperform sharp barriers in the case perpendicular transport while sharp barriers have higher power factor with parallel transport. Lastly, our simulations show that introducing potential barriers does not always improve power factor, particularly when transport is perpendicular to the barriers, nor that sharp barriers are universally advantageous. Our study will guide future implementations of flexible and efficient 2D TE devices with significantly enhanced power factors. Further investigation in to understanding the effect of multi barrier structures on TE efficiency is much needed. This will help in understanding the impact of resonant states on TE performance especially in resonant tunneling diodes (RTDs).

CHAPTER 5

PHONON DRAG CONTRIBUTION TOWARDS SEEBECK COEFFICIENT IN MoS_2: USING FULL PHONON DISTRIBUTION

Studies explored the phonon drag contribution in 2D systems like GaAs/$Al_xGa_{1-x}As$ heterojunctions, $LaAlO_3$/$SrTiO_3$ heterostructures [152, 153, 154, 155, 156, 157, 158]. Similar 2D systems like carbon nanotubes [159, 160, 161, 162], graphene [163, 164] and graphene nanoribbons [165] are studied to understand the phonon drag effect in these systems. This boost to the electron transport can be calculated by taking in to account the rate at which momentum is transferred from electronic system to phonon and carrier current density. Assuming that phonons are in equilibrium and isotropic, phonon drag contribution can be written as [166],

$$S_{ph} \approx \mp m^* v_p^2 (f\tau_p / e\tau_e T) \tag{5.1}$$

where τ_p is the effective phonon relaxation time, τ_e is effective electron relaxation time, v_q^2 is the group velocity of phonons and m^* is the electron effective mass. f is the fraction of the crystal momentum lost by electronic system to phonon system and written as

$$f = \frac{\tau_{ac}^{-1}}{\tau_{ac}^{-1} + \tau_{es}^{-1}}, \tag{5.2}$$

where τ_{ac}^{-1} and τ_{es}^{-1} are electron-phonon relaxation time and rest of the momentum destroying processes, respectively. Processes like impurity scattering can result in loss of electron momentum which restricts the complete transfer of momentum. To obtain the above phonon drag Seebeck coefficient, Onsager relation is used where Peltier coefficient

is calculated. Peltier coefficient is the ratio of phonon heat flux and electric current density. Phonon heat flux is written as

$$Q^p = \mp v_p^2 \tau_p enFf, \tag{5.3}$$

and using electric current density $J = \sigma F$, substituting them in Onsager relation gives Eq. 5.1.

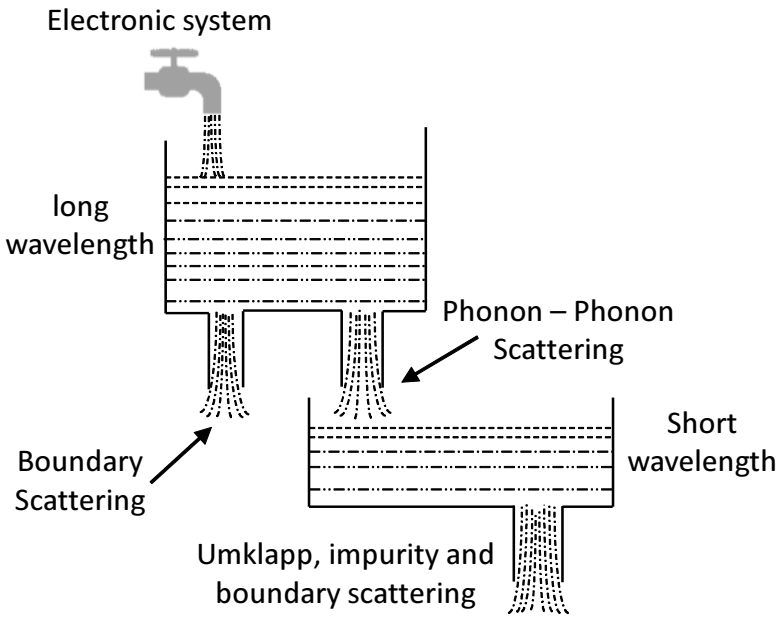

Figure 5.1: Momentum transfer from electronic system to lattice or phonon modes of low and high wavelength (adapted from [6]).

Much of the momentum contributed from electronic system is fed into long wavelength phonons (low q). The upper sign represents electrons and lower sign represents holes. For phonon contribution towards Seebeck coefficient to be significant, the ratio of phonon to electron/hole relaxation time to be significantly higher. As shown in Fig. 5.1, these long wavelength phonons can escape to short wavelength phonons through phonon-phonon scattering or lost to processes like boundary scattering. The momentum transferred to short wavelength phonons is lost to impurity, umklapp, or boundary scattering. At low temperatures, much of the momentum stays with long wavelength phonons as they are less susceptible to scattering. Due to their significant contribution towards the total momentum

at low temperatures, long wavelength phonons alone almost determine the phonon scattering rate τ_p. Cantrell-Butcher formulated the phonon drag in 2D systems which are scattered by 3D phonons [167] as

$$S_{ph} = \pm \frac{g_s g_v e}{2A\sigma kT^2} \sum_{k,k',Q} \hbar\omega_q f(E_k)[(1 - f(E'_k))] p_p^a(k,k') \tau_p v_p . (v_k \tau_k - v'_k \tau'_k) \tag{5.4}$$

where g_s, g_v are the spin and valley degeneracy, the electron transition rate p_p^a is given by

$$p_p^a(k,k') = \frac{2\pi}{\hbar} \left| \frac{g_p}{\epsilon(q)} \right|^2 N_q \delta(E'_k - E_k - \hbar\omega_q) \delta_{k',k+q}. \tag{5.5}$$

One can retrieve the Eq. 5.1 from Eq. 5.4 by replacing the scattering with acoustic phonon scattering with equilibrium phonons at weak electric fields (for details refer [168]). Using this formalism, phonon drag is calculated in MoS_2 at low temperatures to show significant contribution towards Seebeck coefficient. Even though these studies explored the effect of phonon drag in 2D systems, they excluded the impact of normal phonon-phonon processes that play a significant role in these systems. This dominant contribution of normal processes to transport, more than momentum destroying umpklapp processes, results in hydrodynamic transport especially in low temperatures. By including the impact of normal processes in phonon distribution, a better understanding of phonon drag can be achieved in 2D systems.

5.1 Nonequilibrium phonon contribution to electron transport

The time-dependent phonon BTE (pBTE) for the phonon modes q in a branch b is given by

$$\frac{\partial N_{q,b}(\vec{r},t)}{\partial t} + \vec{v}_{q,b} \cdot \nabla_{\vec{r}} N_{q,b}(\vec{r},t) = \left[\frac{\partial N_{q,b}(\vec{r},t)}{\partial t} \right]_{coll}. \tag{5.6}$$

In order to include these normal processes Allen's improved Callaway model (AIC) [169] introduces a perturbation to phonon distribution due to the presence of normal processes

that relaxes to a drifted distribution with a drift velocity of $\vec{\lambda}$. The collision term is written as the sum of two terms

$$\left[\frac{\partial N_{q,b}}{\partial t}\right]_{coll} = -\left(\frac{N_{q,b} - N^0_{q,b}}{\tau^R_{q,b}}\right) - \left(\frac{N_{q,b} - N^*_{q,b}}{\tau^N_{q,b}}\right), \tag{5.7}$$

which is the sum of rate at which non-equilibrium distribution returns to Bose-Einstein distribution ($N^0_{q,b} = [e^{(\hbar\omega_{q,b}/kT)} - 1]^{-1}$) and drifted distribution $N^*_{q,b}$ (referred to as *flowing equilibrium*) respectively. The flowing equilibrium is written as drifted Bose-Einstein distribution $N^*_{q,b} = [\exp(\hbar\omega_{q,b}/kT + \vec{\lambda}\cdot q) - 1]^{-1}$, with a displacement $\vec{\lambda}$. The $\tau^R_{q,b}$ and $\tau^N_{q,b}$ are the average resistive and normal scattering times respectively. The $\tau^R_{q,b}$ and $\tau^N_{q,b}$ are the average resistive and normal scattering times respectively that relaxes the non-equilibrium distribution. Resistive processes include umklapp phonon-phonon processes, isotope, and line-edge roughness scattering. The deviation of the phonon distribution function from equilibrium is $\Phi_{q,b}(\vec{r},t) = N_{q,b} - N^0_{q,b}$. The flowing equilibrium $N^*_{q,b}$ is expanded around $\vec{\lambda} = 0$ in a Taylor series, [170, 171] keeping terms up to first order in $\vec{\lambda}$

$$N^*_{q,b} \approx N^*_{q,b}(\vec{\lambda} = 0) + \vec{\lambda}\cdot\left(\frac{\partial N^*_{q,b}}{\partial\vec{\lambda}}\right)_{\vec{\lambda}=0} = N^0_{q,b} - \frac{kT^2}{\hbar\omega_{q,b}}\frac{\partial N^0_{q,b}}{\partial T}(\vec{\lambda}\cdot\vec{q}). \tag{5.8}$$

On replacing $N^*_{q,b}$ on the right side of Eq. (5.6) with the expression in Eq. (5.8), and $N_{q,b} - N^0_{q,b}$ with $\Phi_{q,b}$, and first Fourier-transform the time-dependent pBTE is written as

$$\vec{v}_{q,b}\cdot\nabla T\frac{\partial N^0_{q,b}}{\partial T} = -\frac{\Phi_{q,b}}{\tau^C_{q,b}} - \frac{1}{\tau^N_{q,b}}\left[\frac{kT^2}{\hbar\omega_{q,b}}\frac{\partial N^0_{q,b}}{\partial T}\vec{\lambda}\cdot\vec{q}\right], \tag{5.9}$$

where $1/\tau^R_{q,b} + 1/\tau^N_{q,b}$ is the combined quasi-particle relaxation rate $1/\tau^C_{q,b}$ [171]. By rearranging the terms, $\Phi_{q,b}$ can be written as

$$\Phi_{q,b} = -\tau^C_{q,b}\vec{v}_{q,b}\cdot\nabla T\frac{\partial N^0_{q,b}}{\partial T} - \frac{\tau^C_{q,b}}{\tau^N_{q,b}}\frac{kT^2}{\hbar\omega_{q,b}}\frac{\partial N^0_{q,b}}{\partial T}(\vec{\lambda}\cdot\vec{q}) \tag{5.10}$$

To obtain an expression for the displacement of the drifted distribution $\vec{\lambda}$ we follow AIC model [171], according to which the total crystal momentum should be the same for both the actual distribution $N_{q,b}$ and the flowing equilibrium $N^*_{q,b}$. From which we can write displacement as

$$\lambda = \frac{\lambda_1}{\lambda_3}\frac{\partial T}{kT^2} = \frac{\sum_{q,b} q_{\parallel}\left(\tau^C_{q,b} v_{q,b}\frac{\partial N^0_{q,b}}{\partial T}\right)\nabla T}{\sum_{q,b} q_{\parallel}^2 \frac{\partial N^0_{q,b}}{\partial T}\frac{kT^2}{\hbar\omega_{q,b}}\left(1-\frac{\tau^C_{q,b}}{\tau^N_{q,b}}\right)}, \tag{5.11}$$

where $q_{\parallel}$ is the phonon wavevector in the transport direction.

To better include the phonon drag contribution that comes from acoustic phonon scattering, the phonon distribution is expanded to include the non-equilibrium contribution ($\Phi_{q,b}$). In order to do that the general equipartition approximation used to calculate the acoustic phonon scattering given as

$$\Gamma^{ac}_{el} = \frac{2\pi D_1^2 kT D(E)}{\hbar\rho v^2}, \tag{5.12}$$

is expanded to include the full scattering matrix. The acoustic phonon scattering including the complete phonon distribution is defined as

$$\Gamma^{ac}_{b} = \frac{\pi D_1^2}{\rho v}\int dk' \left(N^0_{q,b} + \phi_{q,b} + f^{\pm} + \frac{1}{2} \mp \frac{1}{2}\right)\delta(k \pm q - k')\delta(E(k) \pm \hbar\omega_0 - E(k'))). \tag{5.13}$$

The full scattering matrix based acoustic phonon scattering can be included in the Rode's equation (4.7) to solve for the perturbation in the electron distribution. This perturbation in distribution can be used to calculate the TE parameters that can effectively account for the phonon drag contribution towards TE performance.

5.2 Model implementation

A comprehensive model that solves the coupled electron and phonon transport using BTE and account for the effect of non-equilibrium phonons on electron transport is im-

plemented here. Rode's method along with the AIC model [171] is used to solve the coupled electron and phonon BTE. The non-equilibrium phonon contribution towards electron transport is included by solving for the perturbation in phonon distribution and replacing the acoustic phonon scattering with Eq. 5.13. The deviation or perturbation of the phonon distribution ($\Phi_{q,b}$) as shown in Eq. 5.10 is calculated using AIC model. Here, we use monolayer MoS_2 in this study to understand the phonon drag contribution towards TE performance. Phonon dispersion and band structure of MoS_2 are calculated from Quantum Espresso, a first-principles DFT implementation. Then the phonon scattering rates used including anharmonic umklapp and normal phonon-phonon [12], isotope [172], and line-edge roughness [173] are taken from [174]. The only unknown component in Eq. 5.10 is the temperature gradient (∇T) across the simulation domain. In order to calculate ∇T, Rode's method is used to calculate the perturbation to distribution with Bose-Einstein distribution assuming $\Phi_{q,b} = 0$. The scattering rates that influence charge transport in MoS_2 are elaborated in 4.3 and the same parameters are used in this model. Here, instead of using open circuit method to calculate the transport parameters, a current compensation method is implemented. At a given ∇T, $g(k)$ is iteratively solved at an applied electric field by modifying 4.7,

$$g_{i+1} = \frac{S_{io} g_i + \frac{eF}{\hbar}\frac{\partial f_0}{\partial k} - v_r \frac{\partial f_0}{\partial T}\nabla T}{S_0}. \tag{5.14}$$

Using bisection method to scan between T_{max} and T_{min}, a ∇T is identified that can compensate the current from the applied field to produce zero current ($J = 0$) as shown in Fig. 5.2.

Using ∇T to calculate $\Phi_{q,b}$ for acoustic modes, phonon wave vectors that contribute to electron scattering is calculated using the electronic band structure. For all electron states k, phonon wave vectors required for all the possible transitions to k' for both absorption and emission, can be accounted for in a single q ($q = k - k'$) matrix (in both x and y directions). A series of reduction criteria are used to reduce the required q elements to calculate $\Phi_{q,b}$ as described in Fig. 5.3. This reduction in number of q elements can speed up the calculations

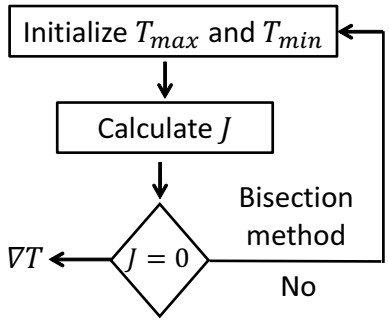

Figure 5.2: Temperature gradient (∇T) required to calculate the perturbation to phonon distribution ($\Phi_{q,b}$) is solved for using bisection method using current compensation method. By applying an electric field and scanning for the appropriate ∇T as shown in flow chart that produces zero current due to the compensating drift (from electric field F) and diffusion (from temperature gradient ∇T) currents.

along with avoiding any redundant calculations. First, the entire q is divided in diagonal, upper and lower triangular arrays. The phonon perturbation for diagonal array requires the calculation of $\Phi_{q,b}$ at $q = 0$ due to no change in state or self scattering. To further reduce the required calculations, all the phonon wave vectors without sufficient energies are removed from both upper and lower arrays. Using the phonon dispersion, the maximum possible energy of phonons in acoustic modes is calculated and compared with the required energy to facilitate the transitions from k to k'. This is done by comparing the $E(k) - E(k')$ with $E_{max} = max\{E_{q,b}\}$ where $b \in \{LA, TA\}$ modes. From the remaining q arrays, unique pairs of (q_x, q_y) are identified in upper and lower triangular arrays, to remove redundancy. These arrays are used to calculate $\Phi_{q,b}$ for acoustic phonon modes that contribute to acoustic phonon scattering. Then using diagonal, upper, and lower arrays to create the full $\Phi_{q,b}$ matrix is reconstructed to calculate the acoustic phonon scattering Γ_b^{ac}.

The perturbation to the electron distribution is calculated using the Rode's method with the updated acoustic phonon scattering rates. Due to the inclusion of inelastic processes in acoustic phonon scattering, Rode's is updated to reflect the contribution from in-scattering towards $I(k)$ (as shown in Eq. 4.18). Electron scattering deformation potentials used are described in section 4.3. After solving for the perturbation in electron distribution, TE

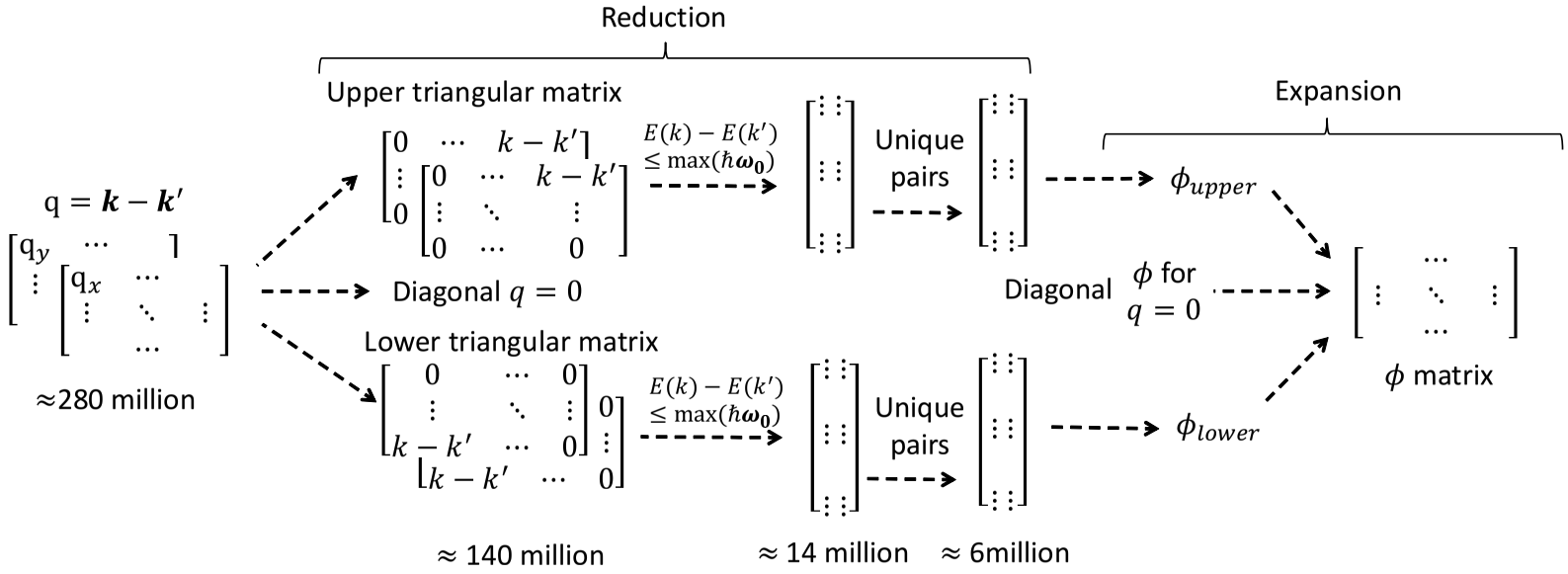

Figure 5.3: Reduction of the phonon momentum vectors (q vectors) to reduce the computation time of full scattering matrix. Unique phonon momentum vector are identified by splitting the matrix in to upper and lower triangular matrices. The phonon probability distribution for these unique q vectors are calculated and expanded back to full matrix.

parameters are calculated as shown in Eq. 1.6 & Eq. 1.7 that include the phonon drag contribution towards Seebeck coefficient S_{ph}. The implementation of our model used in this study is shown in Fig. 5.4 in the form of a flow chart.

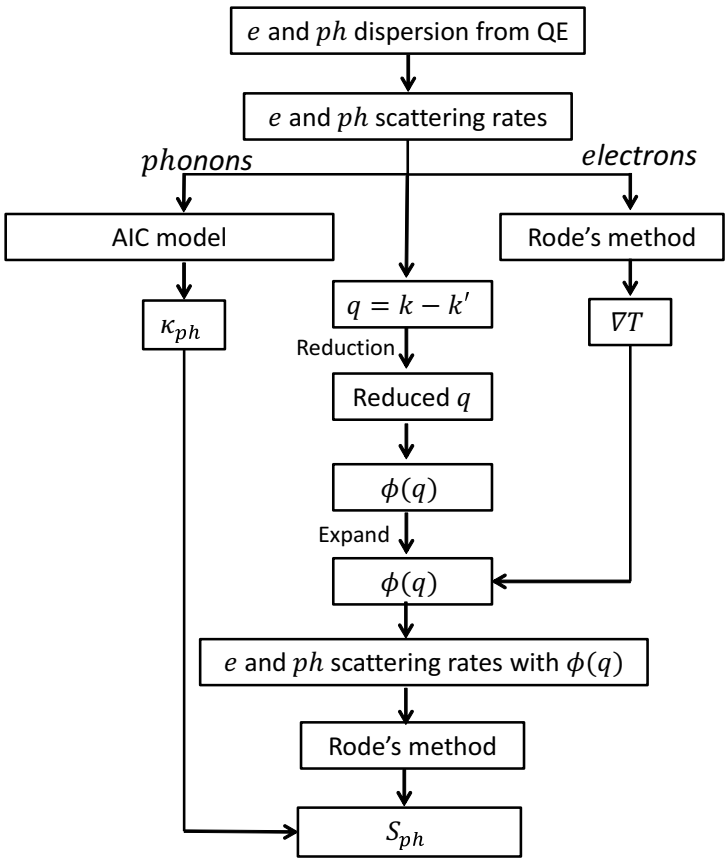

Figure 5.4: Flow chart of coupled electron-phonon Boltzmann solver to calculate the impact of phonon drag on Seebeck coefficient.

5.3 Phonon drag in MoS_2

Seebeck coefficient (S) of MoS_2 is calculated to understand the contribution of non-equilibrium phonons by varying temperature and electron carrier density. Fig. 5.5(a) and (b) shows the S obtained at $N_d = 1\times 10^{12}$ cm^{-2} and $N_d = 7\times 10^{12}$ cm^{-2} respectively. Including the perturbation (ϕ shown in Eq. 5.10) to calculate Inelastic acoustic scattering with complete phonon distribution boosts S compared to elastic acoustic scattering. Further,

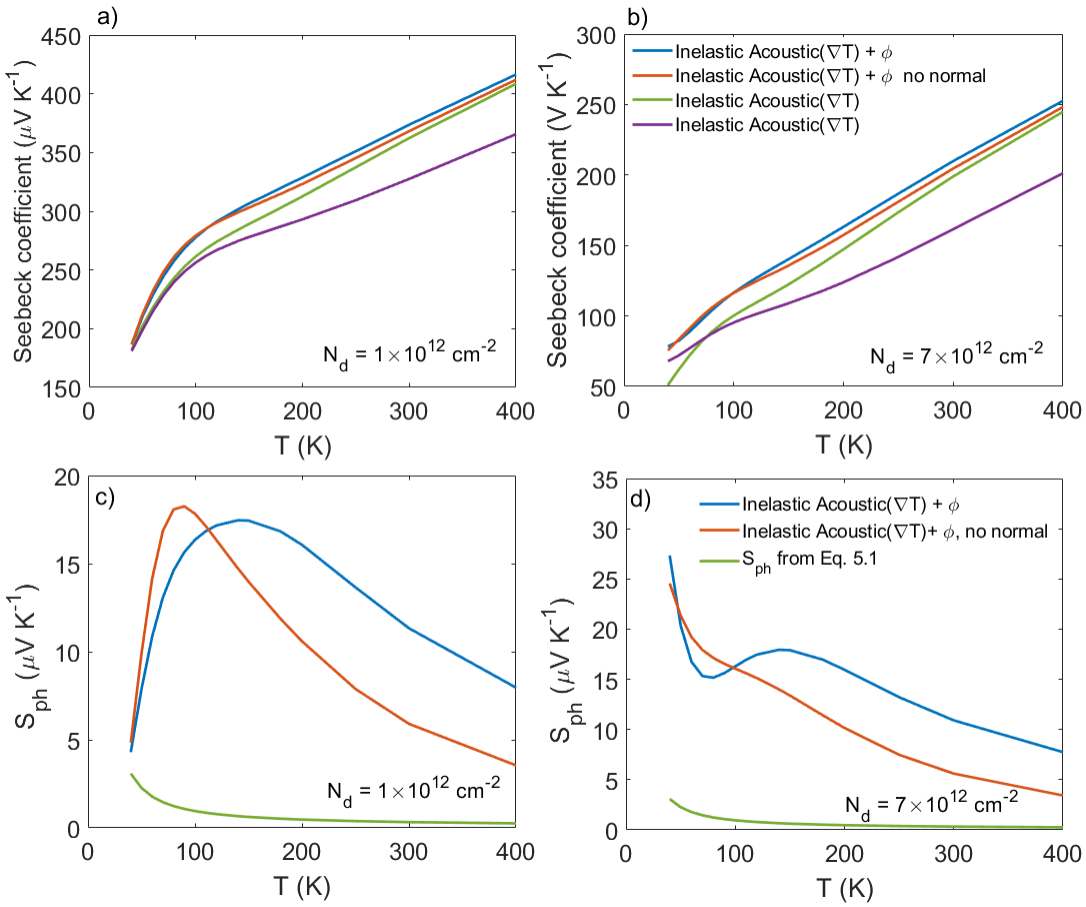

Figure 5.5: Seebeck coefficient of MoS_2 at a) $N_d = 1\times 10^{12}$ cm^{-2} and b) $N_d = 7\times 10^{12}$ cm^{-2}. The full phonon distribution is included in calculating the inelastic acoustic phonon scattering. Perturbation in phonon distribution from normal processes contribute significantly towards phonon drag in addition to resistive phonon processes. The phonon drag contribution towards S at different temperatures is plotted for carrier density of c) $N_d = 1\times 10^{12}$ cm^{-2} and d) $N_d = 7\times 10^{12}$ cm^{-2}.

ϕ also includes the contribution from phonon normal processes that can improve S. Fig. 5.5(a) and (b) shows this additional contribution from these normal processes especially at low temperatures. Fig. 5.5(c) and (d) help to visualize the phonon drag contribution to S (S_{ph}) and the relative contribution from ϕ. Approximated phonon drag S_p (Eq. 5.1) is plotted to show the inability of this approximation in calculating the phonon drag. Availability of more carriers to interact with phonons result in high contribution from phonon drag towards S especially at temperatures below 70 K. Above 70 K, there is little to no

effect from difference in electron carrier density. Including the phonon normal processes, a peak Seebeck phonon drag of 17 μV K^{-1} at T $>$ 70 K irrespective of the carrier density.

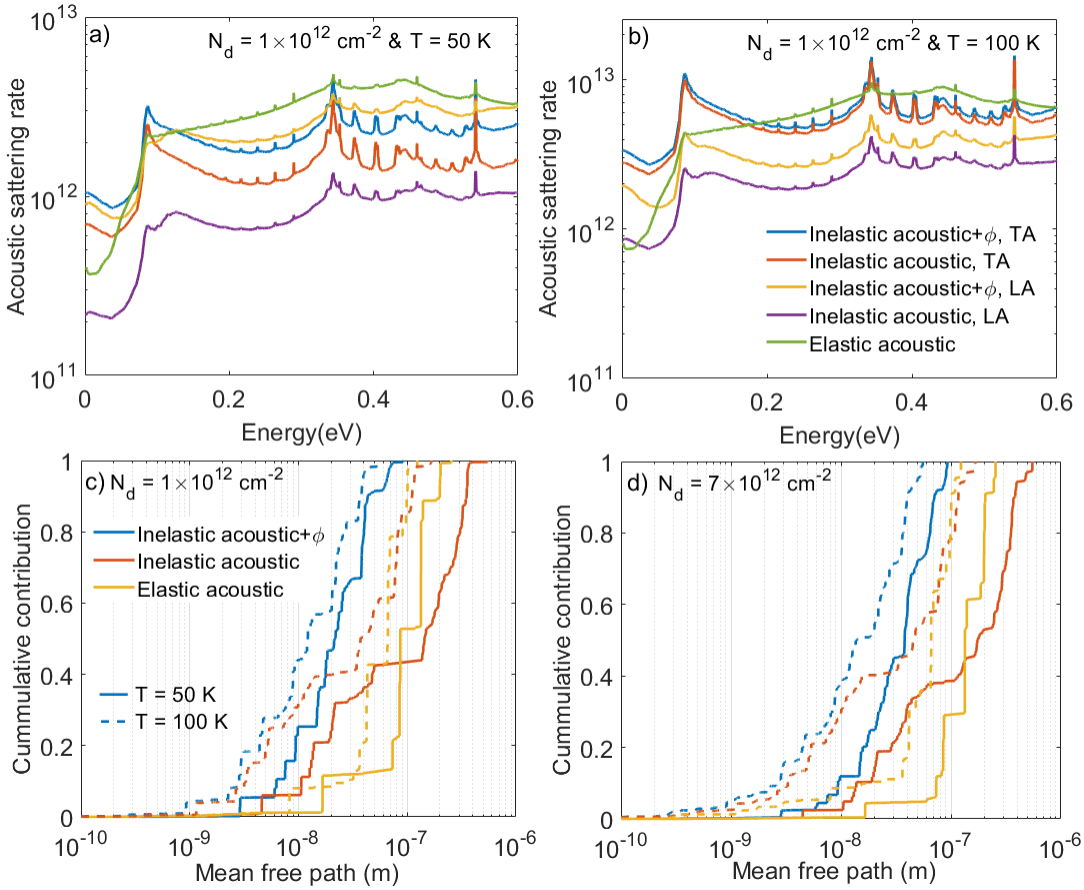

Figure 5.6: Acoustic phonon scattering at a) T = 50 K and b) T = 100 K at a carrier density of N$_d$ = 1×10^{12} cm^{-2}. TA phonons contribute more towards acoustic phonon scattering thereby contributing more towards phonon drag. The cummulative contribution of mean free path towards electrical conductivity is compared at t = 50 K and T = 100 K to understand the impact of ϕ. Higher mean free path contributing more towards transport at d) N$_d$ = 7×10^{12} cm^{-2} results in higher phonon drag contribution compared to c) N$_d$ = 1×10^{12} cm^{-2} at low temperatures.

The impact of carrier density can be understood using the mean free path of carriers. Fig. 5.6(c) and (d) shows cumulative contribution towards electrical conductivity corresponding to mean free path of carriers at T = 50 K and T = 100 K. Using inelastic acoustic scattering accounts for non-equilibrium phonons leads to more electron-phonon interaction and decreases the mean free path of carriers. At lower temperatures, conductivity of carri-

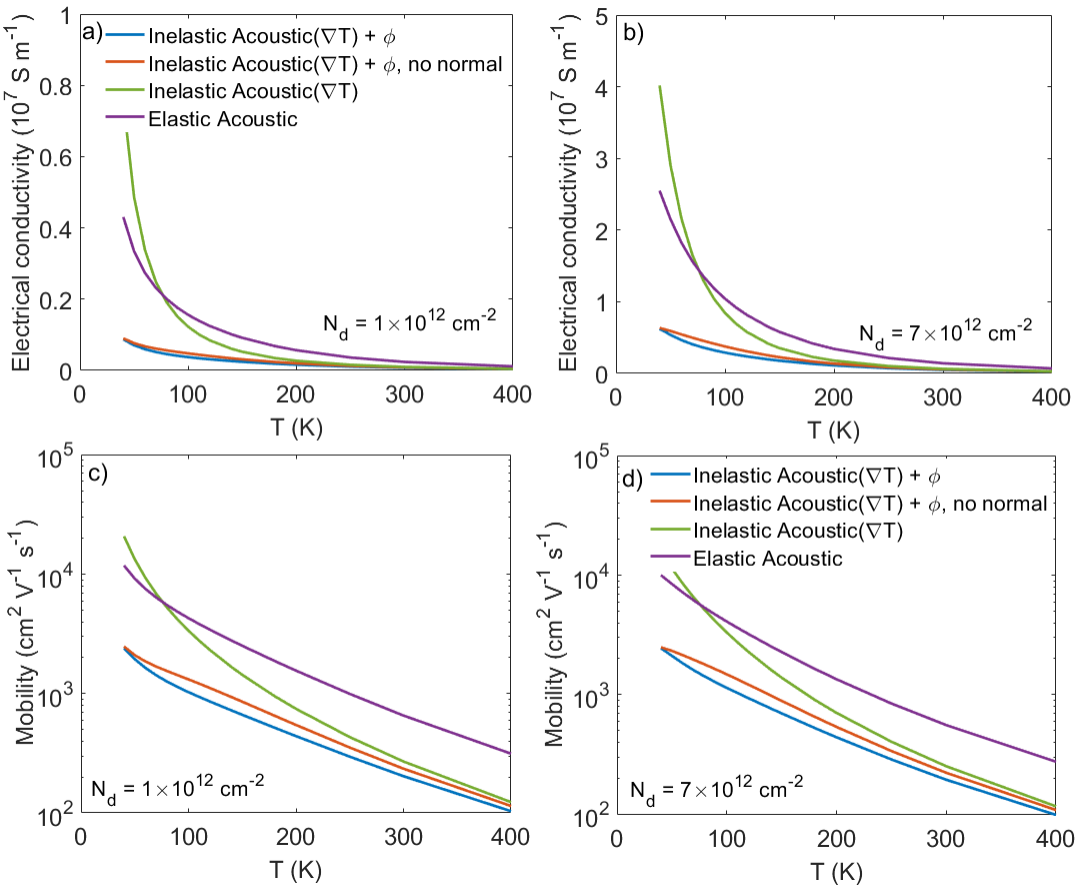

Figure 5.7: Electrical conductivity of MoS_2 at a) $N_d = 1\times10^{12}$ cm^{-2} and b) $N_d = 7\times10^{12}$ cm^{-2} and the impact of non-equilibrium phonons on electrical transport. The influence of carrier density on mobility of electrons at carrier densities c) $N_d = 1\times10^{12}$ cm^{-2} and d) $N_d = 7\times10^{12}$ cm^{-2} by varying the temperature. The change in mobility of electrons is minimal even with change in carrier density especially at carrier densities below $N_d = 1\times 10^{13}$ cm^{-2}.

ers is higher which is a consequence of higher mean free path. With increasing the carrier density from $N_d = 1\times 10^{12}$ cm^{-2} to $N_d = 7\times 10^{12}$ cm^{-2} the mean free path of carriers that contribute also changes. At $N_d = 7\times 10^{12}$ cm^{-2}, where peak power factor is observed in intrinsic MoS_2, higher mean free path carriers contribute to transport compared to lower carrier density especially at low temperatures. Coming to the relative contribution of TA and LA towards the phonon drag, acoustic scattering rate is plotted in Fig. 5.6(a) and (b) with respect to the carrier energy. TA phonons interact more with electrons compared to

LA phonons irrespective of the temperature especially at low energies that contribute to the transport. Since phonon drag contribution towards S (Eq. 5.1) is inversely proportional to relaxation time, TA phonons contribute to more towards phonon drag.

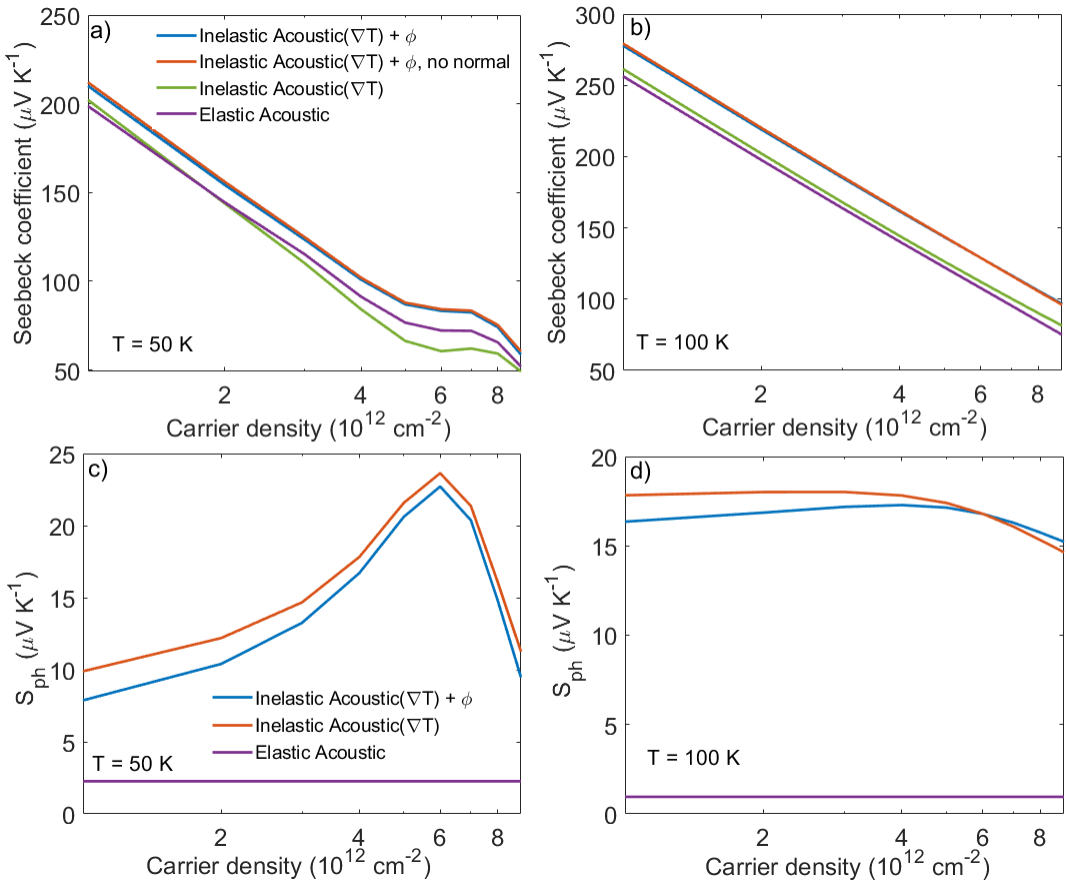

Figure 5.8: Significant increase in phonon drag contribution at low temperatures (T $<$ 70 K) with a carrier density of N_d = 6$\times$ 10^{12} cm^{-2}. The impact of carrier density on Seebeck coefficient in MoS_2 at a) T = 50 K and b) T = 100 K. The corresponding phonon Seebeck coefficient is plotted in c) and d). At T $>$ 70 K, there is no change in phonon drag contribution with increase in carrier density.

The increase in electron-phonon interactions at low temperatures which boosts the phonon drag in turn reduces the electrical conductivity. As seen in Fig. 5.7(a) and (b), including ϕ in phonon distribution results in reduction of electrical conductivity compared to using equilibrium Bose-Einstein distribution. This trend in electrical conductivity doesn't change with carrier density but scales with changes in carrier density. Little to no change in

mobility of electrons as seen in Fig. 5.7(c) and (d) with carrier density leads to this linear scaling in electrical conductivity. To further understand the impact of carrier density on phonon drag, S is calculated by varying the carrier density as shown in Fig. 5.8. Increasing the carrier density shows the expected decrease in S irrespective of the temperature. This is due to the diffusion Seebeck coefficient that dominates the total Seebeck coefficient. But, at T = 50 K the phonon drag contribution (S_{ph}) peaks near $N_d = 6\times 10^{12}$ cm^{-2} where the power factor peaks. Phonon drag contribution at this carrier density is more than twice of that observed $N_d = 1\times 10^{12}$ cm^{-2}. This behavior is not observed at temperatures higher than 70 K and S_{ph} is not affected by the change in carrier density. Also, using a elastic acoustic phonon scattering to influence transport is unable to capture this behavior.

5.4 Conclusion

Applying our transport model that captures the non-equilibrium phonon influence on carrier transport in MoS_2, we calculate the contribution of phonon drag towards Seebeck coefficient. Since the model is based on full phonon distribution and exact scattering rates, we will estimate the amount of momentum transfer to electrons from phonons. Also, the relative contribution from TA and LA towards phonon drag is studied. Our simulations show TA phonons contribution towards phonon drag is higher than LA phonons. At higher carrier densities, phonon drag boosts Seebeck coefficient up to 27% to low temperatures. This boost in phonon drag is due to increase in electron phonon interaction that result in higher scattering rates. Using this comprehensive model, we show the phonon drag impact on Seebeck coefficient and is not captured by existing models. Further, this model can be adopted to materials with known higher influence of normal processes on transport that control the phonon drag, which in future can be used in material selection for TE devices that operate at low temperatures.

CHAPTER 6

HIGH THERMOELECTRIC POWER FACTOR IN TWISTED BILAYER GRAPHENE (TBG)

With the breakthrough in graphene fabrication [175], extensive research is carried out to understand its properties and viability in different applications. Even though graphene has high electrical conductivity, the Dirac nature of the material with almost no bandgap limits its use in electronic devices. Especially in TE devices where higher bandgap improves Seebeck coefficient. Several techniques [176, 177, 178, 179] have been proposed to open bandgap in graphene but they result in reduced carrier conductivity. Graphene using hBN substrates is shown to achieve the highest known PF of 36 $mWm^{-1}K^2$ [180]. Apart from the power generation applications, high power factor materials like graphene can enhance passive cooling which is vital for electronic devices [181]. Further graphene thermocouples exhibit highest reported sensitivity [182] which can used in reliable temperature sensors.

Recent studies showed that absence of Fermi velocity at certain magic-angles in twisted bilayer graphene (TBG) resulted in unconventional superconductivity [1, 2] properties. The theoretically predicted flat bands near magic-angles [183, 3] contributes to superconducting states depending on the carrier density and twist angle. These remarkably flat bands with strongly correlated states also exhibits Mott-like insulator behavior at half-filling of moiré subbands. Even though the flat bands indicate sharp features in density of states (DOS), the suppression of DOS at half-filling results in insulating behavior. This combination of features in DOS is desirable for thermoelectric materials where sharp DOS maximizes the thermoelectric performance (ZT)[184, 22]. This in addition to secondary band gap between the lowest and first subbands in TBG can maximize the transport distribution function [26]. The highly tunable bandstructure of TBG with sharp DOS features, offers a new level of

control and a novel avenue to further decouple Seebeck and conductivity but nothing is known yet about its TE performance.

Here we study the impact of unique TBG DOS, on carrier transport and thermoelectric properties of TBG. In strongly correlated systems or "strange metals", resistivity scales linearly with temperature, which is observed in TBG [185, 186]. In these materials, quantum fluctuations are proposed to be the dominant scattering mechanism not phonons that results in T-linear behavior [187, 188]. However, the T-linear resistivity observed at broad range of twist angles in TBG independent of the correlated phases at magic angles [189]. This indicates a unified scattering mechanism control the carrier transport not correlation phases. Hence this study focuses on simulating phonon limited carrier transport at temperatures much higher than the critical temperature ($>$100 K) using bandstructure derived from continuum model. Here Boltzmann transport equation (BTE) is solved using Rode's method to model the carrier transport in TBG. Our model shows TBG has significant high PF compared to other 2D materials and an order higher compared to single layer graphene (SLG).

6.1 Transport model

The twist-angle resolved band structure of TBG used in this study is obtained from openly available exact continuum model proposed in [190]. The exact continuum model is based on $k \cdot p$ perturbation theory, combined with the computational efficiency of tight-binding Hamiltonians and the twist-angle control offered by continuum models. A self-consistent Jacobi iterative scheme based on Rode's method [191] is implemented to solve BTE. Rode's method is used here to incorporate the inelastic scattering effectively, especially the in-scattering of carriers. This is important in a Dirac material like graphene where transport is predominantly bipolar and significantly affected by inelastic scattering [101]. The carrier probability can be written as a sum of the equilibrium component (determined by Fermi-Dirac statistics, $f_0(k)$) and a small perturbation ($g(k)$) in the direction of the

applied field, $f(k) = f_0(k) + g(k)$. Using the standard Boltzmann form of the collision operator and Rode's method, the perturbation to carrier distribution is calculated using Eq. 4.7 and 4.18.

The δ function in Eq. 4.18 is evaluated using 2D version of Spherical Averaging (SAVE) method [192] by expanding the band structure inside a circle of radius R_s to compute the length of the constant-energy contour with a weight of $\Lambda(k')g_i(k')$. S_o is sum of the scattering processes, F is the applied electric field and Λ is a scattering dependent pre-factor to include the in-scattering rates [5]. The scattering rates included here are elastic acoustic phonon scattering (Γ_{ac}, Eq. A.5) and inelastic optical phonon scattering (Γ_{op}, A.10). In Eq. A.10, pre-factor to the integral represents $\Lambda(k')$ used in Eq. 4.8. Once the Jacobi iteration reaches convergence, as measured by the error between successive iterations, converged $g(k)$ is used to calculate transport distribution function (TDF) using Eq. 4.9. S and σ of the carriers are calculated from the TDF using Eq. 1.6 & Eq. 1.7 respectively. Due to the bipolar nature of the transport in TBG, the effective Seebeck coefficient (S_{eff}) is calculated by averaging the electron (S_n) and hole Seebeck coefficient (S_p) over their respective conductivities (σ_n and σ_p), S_{eff} = ($S_n\sigma_n + S_p\sigma_p$)/($\sigma_n + \sigma_p$). The total carrier conductivity is the sum of electron and hole conductivity, $\sigma_{eff} = \sigma_n + \sigma_p$.

6.2 Power factor in Graphene

In order to validate our model, TE properties of SLG are calculated using electronic band structure obtained from first principles [193]. Scattering rates are calculated using Eq. A.5 and Eq. A.10 with D_{ac} = 3 eV, D^{Γ}_{op} = 100 eV nm^{-1} at Γ-point, and D^{K}_{op} = 200 eV nm^{-1} at K-point. The deformation potentials are taken from [194] and adjusted to match the Seebeck coefficient [195] and maximum power factor [101]. The inelastic optical phonon processes are calculated at optical phonon energies of ω^{Γ}_{op} = 1589 cm^{-1} = 0.197 eV at Γ-point and ω^{K}_{op} = 1197 cm^{-1} = 0.148 eV at K-point taken from [196]. Fig. 1(a) shows the S_{eff} calculated for SLG at different temperatures by varying the carrier densities

using Rode's method. Our S_{eff}, σ_{eff} and PF (Fig.6.1) for SLG are in agreement with the literature ([195, 180, 101]) and shows the need to implement Rode's method to include the contribution from inelastic processes [197]. A peak PF of 28.6 mW m^{-1} K^2 is observed in SLG for electrons at 300 K when electric field is applied in [0 1] direction (as shown in Fig.6.1(c)).

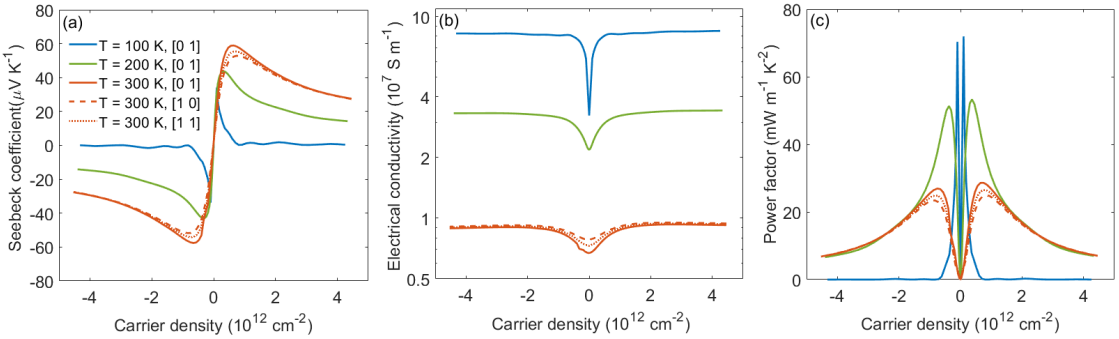

Figure 6.1: Thermoelectric properties of SLG a) Seebeck coefficient, b) electrical conductivity, and c) PF calculated at different temperatures. The peak in S is observed when applied electric field in [0 1] direction at T = 300 K. This translates to higher power factor in [0 1] direction. S_{eff} decreases with decreasing temperature while σ_{eff} increases.

6.3 Power factor in TBG

Our model is then used for TBG to calculate the TE properties at different twist angles. In Fig. 6.2(a) and Fig. 6.2(b) we show the electronic band structures used in this study at twist angle θ = 1.01° and θ = 1.35° respectively extracted from exact continuum model [190]. It shows the flat bands near magic-angle (6.2(a)); the low energy bands open up with increase in twist angle (6.2(b)) and eventually obtains a Dirac cone at K-point. The secondary band gap (E_g shown in 6.2(b)), the bandgap between lower and first subbands for both electrons and holes influences the carrier transport. Especially at half-filling where the material exhibit insulating behavior due the lack of states in the band gap to conduct. Due to the presence of flat bands the DOS of TBG has sharp features. Collision broadening [198, 199] due to carrier scattering with phonons is implemented in this study to account for

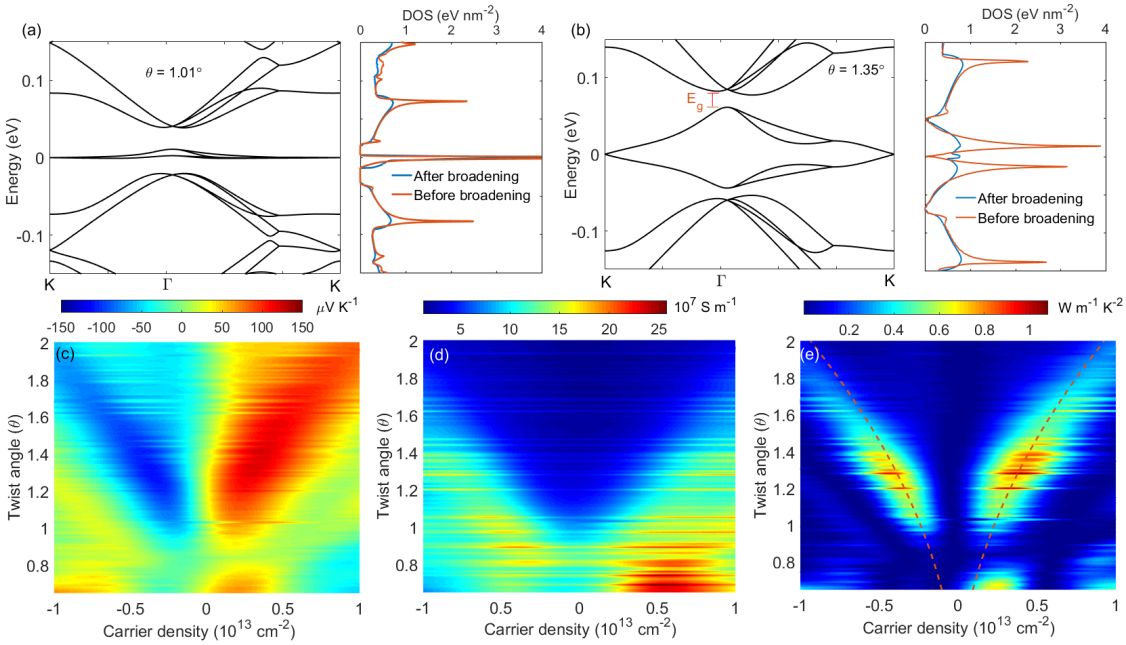

Figure 6.2: Bandstructure and density of states (DOS) of TBG at different twist angles a) 1.01° and b) 1.35°. Room temperature c) Seebeck coefficient(S), d) electrical conductivity (σ), and e) PF of TBG at different twist angles. The peak in power factor is observed at a twist angle of 1.28°. At this twist angle the maximum in S is observed which results in maximum power factor. The dotted lines represent $\pm n_s$ as the carrier density required to fill the lowest moiré subband.

its effect on steady-state energy distribution of carriers at high fields. Collision broadening also results in a high-energy tail of carrier distribution which effects high-energy scattering processes. The DOS calculated after applying inhomogenous collision broadening using acoustic phonon scattering is showed in Fig. 6.2(a) and Fig. 6.2(b) and compared with DOS without any broadening applied. The acoustic phonon scattering in TBG is calculated with a acoustic deformation potential of D_{ac} = 9 eV. This is in line with literature values that suggest D_{ac} of TBG is higher than the the value observed in SLG [200, 189]. D^{Γ}_{op} = 10 eV nm^{-1} with optical phonon energy of 0.150 meV (1213 cm^{-1}) at Γ-point and D^{K}_{op} = 20 eV nm^{-1} with optical phonon energies of 0.148 meV (1197 cm^{-1}) at K-point is used to calculate the inelastic phonon scattering rates [200].

Applying our model, the calculated S_{eff}, σ_{eff} and PF in [0 1] direction at T = 300 K are plotted in 6.2(c-e) with respect to twist angle and carrier density. The simulation domain is

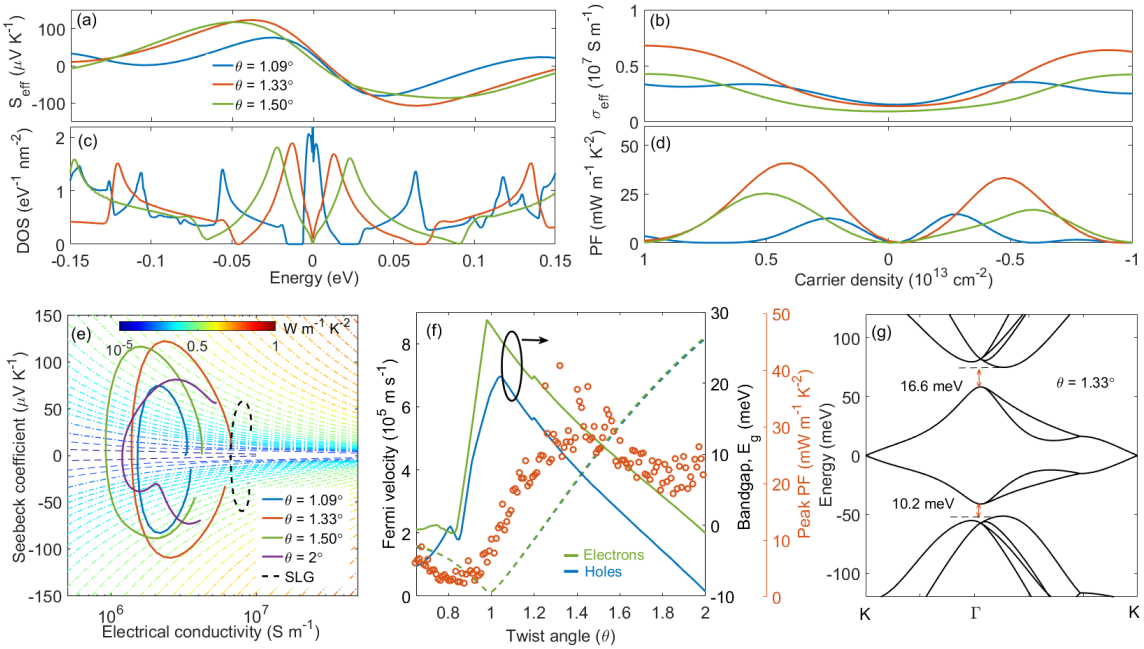

Figure 6.3: (a-d) TE properties near magic-angle (θ = 1.09°), at twist angle with peak PF(θ = 1.33°), and at twist angle with maximum S_{eff} (θ = 1.50°) a) S_{eff}, b) DOS, c) σ_{eff}, and d) PF at T = 300 K. The secondary bandgap in the bandstructure results in a gap in DOS that maximizes the S_{eff} e) Room temperature S_{eff} vs σ_{eff} of TBG at different twist angles compared with SLG to understand the PF peak at θ = 1.33°. The constant PF lines are plotted as a guide to the PF. f) Change in the carrier Fermi velocities of TBG with twist angle. The secondary bandgap (E_g) for electrons and holes at different twist angles. g) Band structure, Fermi velocity and band gap of TBG at a twist angle θ = 1.33° where peak PF is observed.

limited to twist angles above 0.65° due to the limitation of continuum model used for band structure calculation. This limitation comes from the inclusion of atomic relaxation in TBG that suppress the secondary magic-angle below θ = 0.65°. The peak in PF is observed at θ = 1.33° for both electrons and holes near the carrier density of $\pm n_s$ ($\pm$ 4.11 $\times$ 10^{12} cm^{-2} for θ = 1.33°). The peak in S_{eff} translates to the peak in PF as seen in 6.2(c) and σ_{eff} has the expected dependency on carrier density, σ_{eff} increases with increase in carrier density. Both room temperature S_{eff} and σ_{eff} observed at θ = 1.33° is higher than SLG. In 6.3(a), S_{eff} observed at θ = 1.33° is compared with S_{eff} near magic-angle (θ = 1.09°) and θ = 1.50°. Comparing S_{eff} at these twist-angles with their corresponding DOS (6.3(c)) shows that the peak in S_{eff} is a consequence of DOS band gaps where secondary band gaps (E_g)

are observed in band structure. These band gaps in DOS lead to little or no scattering which in-turn maximize the TDF (Eq. 4.9). TDF is proportional to perturbation in carrier distribution ($g(k)$) which is inversely proportional to scattering rates. Also, included in TDF is temperature dependent Fermi window ($\delta f/\delta E$) that determines the peak in S_{eff}.

Our calculations show that at room temperature, holes have S_{eff} of 122 μV K^{-1} which is higher than 107 μV K^{-1} observed in electrons as shown in Fig. 6.3(a). The peak in S_{eff} observed at a twist angle of θ = 1.33° with a carrier density of 3.06 $\times$ 10^{12} cm^{-2} in holes and 4.02 $\times$ 10^{12} cm^{-2} in electrons. On the other hand, σ_{eff} shows a decreasing trend with increasing twist angle with peak near magic-angle. This can be seen in 6.3(b) where increasing the θ from 1.09° to 1.50° decreases the σ_{eff}. This trend is illustrated by observing the S_{eff} and corresponding σ_{eff} for different twist angles in 6.3(e). A simultaneous increase in S_{eff} and σ_{eff} with twist angle peaks at θ = 1.33° and decreases with further increase in twist angle. Comparing with SLG, both S_{eff} and σ_{eff} is higher for TBG in the twist angles studied here. The observed peak in PF at room temperature is 40.8 mW m^{-1} K^{-2} in holes and 33.3 mW m^{-1} K^{-2} in electrons at θ = 1.33° (Fig. 6.3(d)). These peaks in PF occur at a carrier density of 3.99 $\times$ 10^{12} cm^{-2} in holes and 4.71 $\times$ 10^{12} cm^{-2} in electrons which is near the first band filling $n_s = \pm$ 4.11 $\times$ 10^{12} cm^{-2}. To further understand the control of band gap E_g on S_{eff} thereby on PF, highest PF observed at each twist angle either in electrons or holes is plotted along with the corresponding electron and hole secondary band gaps (E_g) in 6.3(f). Both electron and hole band gaps peak near 1° twist angle due to the flat bands in the band structure. This is evident in the corresponding electron and hole Fermi velocities at different twist angles. This shows that the maximum PF observed at any twist angle is dependent on band gap and peaks near the twist angles where band gap is highest. The exact position of the peak in PF relative to peak in band gap is temperature dependent due to change in width of Fermi window. 6.3(e) shows the electronic bandstructure at θ = 1.33° where peak PF is observed, along with the band gap between first and second bands which is 16.6 meV in electrons and 10.2 meV in holes.

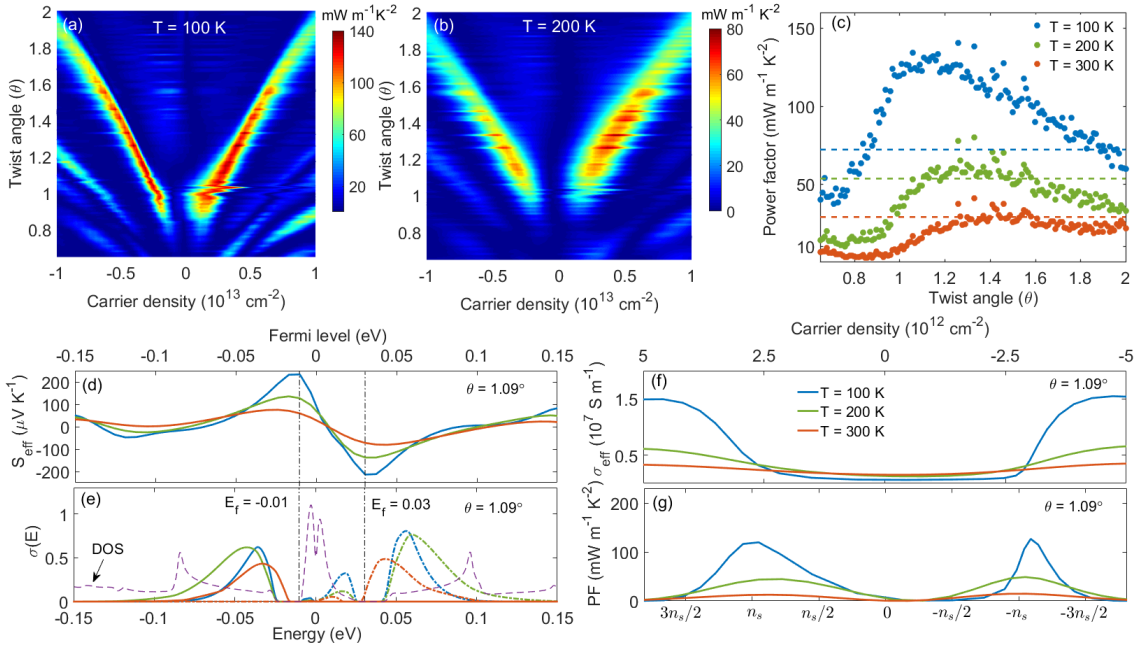

Figure 6.4: Power factor at a) T = 100 K and b) T = 200 K of TBG at different twist angles. c) Temperature dependence of peak PF at twist angles of TBG, observed by varying the carrier densities. The peak in power factor is observed at θ = 1.33° fot T = 300 K, θ = 1.33° for T = 200 K, and θ = 1.26° for T = 100 K. d) Temperature dependence of S_{eff} at θ = 0.97°. e) $\sigma(E)$ at Fermi levels where peak in S_{eff} is observed at T = 100 K. S_{eff} peaks when $\sigma(E)$ is asymmetric with respect to the corresponding Fermi level. Variation in f) σ and g) power factor with temperature at θ = 1.26° at different carrier densities. The peak in power factor is observed at carrier densities near $\pm n_s$ depending on the temperatures.

To understand the temperature dependence of PF in TBG, TE properties are calculated at T = 100 K and T = 200 K by changing the twist angle. We focused on T >= 100 K in this study as transport in lower temperatures can result in hydrodynamic transport which is beyond the scope of our model [201]. 6.4(a) and 6.4(b) shows the PF at different twist angles and carrier densities at T = 100 K and T = 200 K. With decreasing in temperature, the range of carrier densities with high PF reduces and the twist angle with peak PF decreases. The peak in PF either in holes or electrons at T = 100 K and T = 200 K is compared with the values observed at room temperature in 6.4(c). The peak PF is at θ = 1.33° for 300 K and 200 K whereas for 100 K it occurs at θ = 1.26°. A peak PF of 140.2 mW m^{-1} K^{-2} is observed at T = 100 K and 79.6 mW m^{-1} K^{-2} at T = 200 K while the value is 40.8

mW m^{-1} K^{-2} at room temperature. The dotted black line in Fig. 6.4(c) represents peak PF observed in SLG. TBG exhibits a peculiar behavior of increasing power factor with temperature while SLG shows the opposite trend [180]. This temperature dependence is previously observed in high-T_c superconductors like TBG [202]. Power factor in ultrathin FeSe increases an order in magnitude by decreasing temperature from 300 K to 100 K. These peaks in PF coincides with the peak in bandgap (between second and first bands) for both electrons and holes (shown in Fig. 6.3(f)). In 6.4(d), S_{eff} is plotted at $\theta = 0.97^{\circ}$ where PF peaks at T = 100 K, by varying Fermi level (E_f) at different temperatures. Seebeck coefficient increases with the increase of asymmetry in TDF with respect to E_f. Once the lowest subband is filled, increasing E_f further moves peak in TDF beyond E_f resulting in a change in the sign of S_{eff} as seen in 6.4(d). Contrary to the reduction of S_{eff} in SLG with decreasing temperature, it increases in TBG. This behavior can be explained using σ(E) or TDF, at lower temperatures the narrow width of Fermi window combined with the band gap maximizes the TDF as shown in 6.4(e). σ(E) is plotted at Fermi levels where S_{eff} maximum for holes and electrons which is E_f = -0.01 and E_f = 0.03 respectively. σ(E) seen above 0 eV corresponds to electrons and below 0 eV corresponds to holes. σ_{eff} at this twist angle increases with decreases with temperature due to the reduction in carrier scattering. This results in peak PF where the S_{eff} peaks with PF increasing with decreasing temperature. The peak in PF observed is at carrier densities that are near $\pm n_s$ as shown in 6.4(g). This shows that E_f above the first subband into the bandgap in DOS optimizes the TDF providing the observed high PF.

6.4 Conclusion

In conclusion, using an iterative solver for Boltzmann transport equation, phonon-limited thermoelectric properties of TBG are calculated by varying the twist angle. Both acoustic and optical phonon scattering rates are included to capture the carrier interactions. Band structure of TBG is obtained from a exact continuum model coupled with

tight-binding Hamiltonians. Our calculations show a peak PF of 40.8 $\mathrm{Wm^{-1}\ K^{-2}}$ at room temperature at a twist angle of 1.33°, which is two orders higher than SLG. The combination of flat bands with secondary band gap results in high Seebeck coefficient which eventually improves PF. The peak in power factor converges to a twist angle where the secondary band gap is maximum $\theta \approx 1.26°$, as temperature decreases from room temperature. Using temperature and twist angle as knobs, TE properties of TBG can be tuned to achieve desired TE performance. These unique properties of TBG makes it a promising candidate for future TE devices that can be operated under a wide spectrum of performance requirements.

APPENDIX A

SCATTERING RATES

The scattering rates that have been used in our calculations are:

A.1 Acoustic phonon scattering

Acoustic phonon scattering rate (Γ_{ac}^{3d}) in Bulk or 3D material is given as:

$$\Gamma_{ac}^{3d} = \frac{2\pi D_{ac}^2 k_B T}{\hbar v^2 \rho} DOS(E) \tag{A.1}$$

Acoustic phonon scattering rate (Γ_{acs}^{2d}) in a confined 2DEG is given as:

$$\Gamma_{ac}^{2d} = \frac{2\pi D_{ac}^2 k_B T e^2}{\hbar v_{ac}^2 \rho} \Xi_{nm} \zeta \tag{A.2}$$

where

$$\Xi_{nm} = \int\int \mid \psi_n(x,y) \mid^2 \mid \psi_m(x,y) \mid^2 dxdy \tag{A.3}$$

$$\zeta = \int \delta(k_x - k_x' + q_x)\delta(E - E')dz \tag{A.4}$$

where D_{ac} is acoustic phonon deformation potential, ρ is density, v_{ac} is velocity, $DOS(E)$ is density of states and ψ is the electron wave function. The momentum resolved acoustic phonon scattering in intrinsic 2D materials can be written as:

$$\Gamma_{ac}^{2d}(k) = \frac{2\pi D_{ac}^2 k_B T}{\hbar \rho v_{ac}^2} \int \delta(E(k) - E(k'))dk'. \tag{A.5}$$

A.2 Intervalley optical phonon scattering

Intervalley optical phonon out-scattering rate (Γ^{3d}_{iop}) in bulk or 3D material is given as:

$$\Gamma^{3d}_{iop} = \frac{qZD^2_{op}\left(N+\frac{1}{2}\pm\frac{1}{2}\pm f^{\pm}\right)}{\rho\omega_{op}} DOS(E \pm \hbar\omega_{op}) \tag{A.6}$$

where $\hbar\omega_{op}$ is optical phonon energy, f is Fermi-Dirac statistics for electron, N is the Bose-Einstein distribution for optical phonons, D_{op} is optical phonon coupling constant, ω_{op} is frequency of optical phonons and Z is the number of symmetry directions. '+' denotes absorption of phonon and '-' denotes emission of phonon, the corresponding change in energy of electron are taken care through Fermi-Dirac statistics.

Intervalley optical phonon out-scattering rate (Γ^{2d}_{iop}) in a confined 2DEG is given as:

$$\Gamma^{2d}_{iop} = \frac{\pi D^2_{op}}{\rho\omega_{op}}\left(N+\frac{1}{2}\pm\frac{1}{2}\right)\Xi_{nm}\zeta \tag{A.7}$$

where

$$\Xi_{nm} = \int\int \mid \psi_n(x,y) \mid^2 \mid \psi_m(x,y) \mid^2 dxdy \tag{A.8}$$

$$\zeta = \int \delta(k_x - k'_x \pm q_x)\delta(E - E' \pm \hbar\omega_{f|g})dz \tag{A.9}$$

'$\pm$' shows that there is both emission and absorption of optical phonons. The momentum resolved acoustic phonon scattering in intrinsic 2D materials can be written as:

$$\Gamma^{2d}_{iop}(k) = \frac{\pi D^2_{op}}{\rho\omega_{op}}(N \pm f^{\pm} + \frac{1}{2} \mp \frac{1}{2}) \int \delta(E(k) \pm \hbar\omega_{op} - E(k'))dk'. \tag{A.10}$$

A.3 Deformation potential optical phonon scattering

Deformation potential optical phonon out-scattering rate (Γ^{3d}_{dop}) in Bulk or 3D material is given as:

$$\Gamma^{3d}_{dop} = \frac{\pi D^2_{op}(N_{op} + f^{\pm})}{\rho\omega_{op}} DOS(E \pm \hbar\omega_{op}) \tag{A.11}$$

where D_{op} is deformation potential of the optical phonon.

A.4 Impurity scattering

The impurity scattering rate that has been implemented here is derived by Conwell-Weisskopf as

$$\Gamma_{imp} = \frac{Z^2 e^4 N_I}{16\sqrt{2}\pi\epsilon^2 m^{*1/2} E_k^{3/2}} \log\left(1 + \frac{Ze^2 N_I^{1/3}}{4\pi\epsilon E_k}\right) \tag{A.12}$$

where N_I is the number scattering centers created due to the impurities, m^* is effective mass of the material and E_k is the energy of carriers.

A.5 Boundary scattering

The boundary scattering rate where there is confinement of material with width L and velocity of carriers perpendicular to the boundary $v_z$is given as:

$$\Gamma_{boundary} = \left(\frac{1-p}{1+p}\right)\frac{v}{L} \tag{A.13}$$

where the specularity parameter p is calculated by

$$p = exp(-4k^2\Delta^2 cos(\phi_B)) \tag{A.14}$$

and k is the wave vector of the electron, Δ is the surface roughness and ϕ_B is the angle between the incident electron with the normal of the boundary.

APPENDIX B

WIGNER POTENTIAL AND POTENTIAL OPERATOR

B.1 A square potential with smoothening

A periodic fast-varying potential can be written as

$$V_q(r) = \sum_{n=-\infty}^{\infty} V_p(r - nL_p) \tag{B.1}$$

where V_p is the potential and L_p is the period length. The Wigner potential as shown in Eq. 2.5, is

$$V_w(r,k) = \frac{2}{\pi\hbar}\, Im\{e^{2ikr}\hat{V}_q(2k) \sum_{n=-\infty}^{\infty} e^{-2inL_pk}\} \tag{B.2}$$

where $\hat{V}_q(2k)$ is the Fourier transform of V_q and it can be written as

$$V_w(r,k) = \frac{2}{\pi\hbar} Im\{e^{2ikr}\hat{V}_q(2k) \sum_{m=-\infty}^{\infty} \delta(k - m\pi/L_p)\} \tag{B.3}$$

The quantum evolution term (Eq. 2.3)is obtained as

$$\begin{aligned} Qf_w(r,k) &= \frac{2}{\pi\hbar} \sum_{m=-\infty}^{\infty} Im\{e^{2im\pi r/L_p}\hat{V}_q(2m\pi/L_p)\} f_w(r, k - m\pi/L_p) \\ &= \sum_{m=-\infty}^{\infty} W_m(r) f_w(r, k - m\pi/L_p) \\ &= \sum_{m=1}^{\infty} W_m(r) \left[f_w(r, k - m\pi/L_p) - f_w(r, k + m\pi/L_p)\right] \end{aligned}$$

where the quantum weight $W_m(r)$ is

$$W_m(r) = \frac{2}{\pi\hbar} \sum_{m=-\infty}^{\infty} Im\{e^{2im\pi r/L_p}\hat{V}_q(2m\pi/L_p)\} \tag{B.4}$$

For a periodic potential of period L_p with a square potential of height V_0 with smoothening factor β and width $2a$ of form

$$V_q(r) = \frac{V_0}{2}\left\{-erf[\beta(r-a)] + erf[\beta(r+a)]\right\} \tag{B.5}$$

and Fourier transform of $V_q(r)$ is

$$\hat{V}_q(k) = \frac{2V_0}{k} e^{-k^2/(4\beta^2)} sin(ka) \tag{B.6}$$

The quantum weight is obtained as

$$W_m(r) = \frac{2V_0}{\pi\hbar m} e^{\frac{-m^2\pi^2}{\beta^2 {L_p}^2}} sin\left(\frac{2\pi ma}{L_p}\right) sin\left(\frac{2\pi mr}{L_p}\right) \tag{B.7}$$

B.2 Cosine potential

For a cosine potential of form $V_q(r) = A\, cos(K_0 r)$, the Wigner potential (Eq. 2.5)is obtained as

$$\begin{aligned} V_w(r,k) &= \frac{2A}{\hbar\pi} Im\{e^{2ikr}\hat{V}_q(2k)\} \\ &= \frac{A}{\hbar\pi} Im\{e^{2ikr}\left[\delta(2k-K_0) + \delta(2k+K_0)\right]\} \\ &= \frac{A\, sin(2kr)}{\pi\hbar}\left[\delta(2k-K_0) + \delta(2k+K_0)\right] \end{aligned}$$

The potential operator or force term corresponding to potential variation is

$$\begin{aligned} Qf_w(r,k,t) &= \int dk' V_w(r, k-k')\, f_w(r,k) \\ &= \int dk' \frac{A\, sin(2(k-k')r)}{\pi\hbar}\left[\delta(2(k-k')-K_0) + \delta(2(k-k')+K_0)\right] f_w(r,k) \\ &= \frac{A\, sin(K_0 r)}{\pi\hbar}\left[f_w\left(r, k-\frac{K_0}{2}\right) - f_w\left(r, k+\frac{K_0}{2}\right)\right] \end{aligned}$$

BIBLIOGRAPHY

[1] Yuan Cao, Valla Fatemi, Shiang Fang, Kenji Watanabe, Takashi Taniguchi, Efthimios Kaxiras, and Pablo Jarillo-Herrero. Unconventional superconductivity in magic-angle graphene superlattices. *Nature*, 556(7699):43–50, 2018.

[2] Yuan Cao, Valla Fatemi, Ahmet Demir, Shiang Fang, Spencer L. Tomarken, Jason Y. Luo, Javier D. Sanchez-Yamagishi, Kenji Watanabe, Takashi Taniguchi, Efthimios Kaxiras, Ray C. Ashoori, and Pablo Jarillo-Herrero. Correlated insulator behaviour at half-filling in magic-angle graphene superlattices. *Nature*, 556(7699):80–84, 2018.

[3] Allan H. MacDonald and Rafi Bistritzer. Graphene moiré mystery solved? *Nature*, 474(7352):453–454, 2011.

[4] Matthew Yankowitz, Shaowen Chen, Hryhoriy Polshyn, Yuxuan Zhang, K. Watanabe, T. Taniguchi, David Graf, Andrea F. Young, and Cory R. Dean. Tuning superconductivity in twisted bilayer graphene. *Science*, 363(6431):1059–1064, 2019.

[5] A. Kommini and Z. Aksamija. Thermoelectric properties of periodic quantum structures in the wigner-rode formalism. *J. Phys.: Condens. Matter*, 30(4):044004, 2018.

[6] Conyers Herring. Theory of the thermoelectric power of semiconductors. *Phys. Rev.*, 96(5):1163–1187, 1954.

[7] H. J. Goldsmid. *Thermoelectric Refrigeration*. Plenum, New York, 1964.

[8] N. W. Ashcroft and N. D. Mermin. *Solid State Physics*. Brooks/Cole, Belmont, CA, 1976.

[9] R. Chen, A. I. Hochbaum, P. Murphy, J. Moore, P. Yang, and A. Majumdar. Thermal conductance of thin silicon nanowires. *Phys. Rev. Lett.*, 101:105501, 2008.

[10] T. Markussen, A.-P. Jauho, and M. Brandbyge. Surface-decorated silicon nanowires: A route to high-ZT thermoelectrics. *Phys. Rev. Lett.*, 103:055502, 2009.

[11] Li Shi. Thermal and thermoelectric transport in nanostructures and low-dimensional systems. *Nanoscale Microscale Thermophys. Eng.*, 16(2):79–116, 2012.

[12] D. T. Morelli, J. P. Heremans, and G. A. Slack. Estimation of the isotope effect on the lattice thermal conductivity of group IV and group III-V semiconductors. *Phys. Rev. B*, 66(19):195304, 2002.

[13] P. Yasaei, A. Fathizadeh, R. Hantehzadeh, A. K. Majee, A. El-Ghandour, D. Estrada, C. Foster, Z. Aksamija, F. Khalili-Araghi, and A. Salehi-Khojin. Bimodal phonon scattering in graphene grain boundaries. *Nano Lett.*, 15(7):4532–4540, 2015.

[14] Z. Aksamija and I. Knezevic. Lattice thermal transport in large-scale polycrystalline graphene. *Phys. Rev. B*, 90:035419, 2014.

[15] Z. Aksamija and I. Knezevic. Anisotropy and boundary scattering in the lattice thermal conductivity of silicon nanomembranes. *Phys. Rev. B*, 82:045319, 2010.

[16] Z. Aksamija and I. Knezevic. Anisotropy and edge roughness scattering in the lattice thermal conductivity of graphene nanoribbons. *ECS Trans.*, 35:195, 2011.

[17] L. D. Hicks and M. S. Dresselhaus. Thermoelectric figure of merit of a one-dimensional conductor. *Phys. Rev. B*, 47:16631, 1993.

[18] G. D. Mahan and J. O. Sofo. The best thermoelectric. *Proc. Natl. Acad. Sci. U. S. A.*, 93:7436–7439, 1996.

[19] Y. Pei, A. D. LaLonde, H. Wang, and G. J. Snyder. Low effective mass leading to high thermoelectric performance. *Energy Environ. Sci.*, 5:7963–7969, 2012.

[20] Y. Pei, H. Wang, and G. J. Snyder. Band engineering of thermoelectric materials. *Adv. Mater.*, 24(46):6125–6135, 2012.

[21] M. L. Liu, F. Q. Huang, L. D. Chen, and I. W Chen. A wide-band-gap p-type thermoelectric material based on quaternary chalcogenides of $\mathrm{Cu_2ZnSnQ_4(Q = S, Se)}$. *Appl. Phys. Lett.*, 94(20):202103, 2009.

[22] G. D. Mahan. Figure of merit for thermoelectrics. *J. Appl. Phys.*, 65(4):1578–1583, 1989.

[23] Y. Yan, Y. R. Jin, G. Zhang, J. Yang, Y. Wang, and W. Ren. Optimum electronic structures for high thermoelectric figure of merit within several isotropic elastic scattering models. *Sci. Rep*, 7(1):10104–, 2017.

[24] Y. Pei, X. Shi, A. LaLonde, H. Wang, L. Chen, and G. J. Snyder. Convergence of electronic bands for high performance bulk thermoelectrics. *Nature*, 473:66–69, 2011.

[25] G. Jeffrey Snyder and Eric S. Toberer. Complex thermoelectric materials. *Nature Mater.*, 7:105–114, 2008.

[26] A. Kommini and Z. Aksamija. Low-temperature enhancement of the thermoelectric seebeck coefficient in gated 2d semiconductor nanomembranes. *J. Comput. Electron.*, 15(1):27–33, 2016.

[27] N. Neophytou and M. Thesberg. Modulation doping and energy filtering as effective ways to improve the thermoelectric power factor. *J. Comput. Electron.*, 15(1):16, 2016.

[28] M. Zebarjadi, G. Joshi, G. Zhu, B. Yu, A. Minnich, Y. Lan, X. Wang, M. Dresselhaus, Z. Ren, and G. Chen. Power factor enhancement by modulation doping in bulk nanocomposites. *Nano Lett.*, 11(6):2225, 2011.

[29] H. J. Ryu, Z. Aksamija, D. M. Paskiewicz, S. A. Scott, M. G. Lagally, I. Knezevic, and M. A. Eriksson. Quantitative determination of contributions to the thermoelectric power factor in si nanostructures. *Phys. Rev. Lett.*, 105:256601, 2010.

[30] R. Kim and M. S. Lundstrom. Computational study of the seebeck coefficient of one-dimensional composite nano-structures. *J. Appl. Phys.*, 110:034511, 2011.

[31] J. M. O. Zide, J.-H. Bahk, R. Singh, M. Zebarjadi, G. Zeng, H. Lu, J. P. Feser, D. Xu, S. L. Singer, Z. X. Bian, A. Majumdar, J. E. Bowers, A. Shakouri, and A. C. Gossard. High efficiency semimetal/semiconductor nanocomposite thermoelectric materials. *J. Appl. Phys.*, 108(12):123702, 2010.

[32] Y. Yokomizo and J. Nakamura. Giant seebeck coefficient of the graphene/h-BN superlattices. *Appl. Phys. Lett.*, 103(11):113901, 2013.

[33] N. Neophytou, X. Zianni, H. Kosina, S. Frabboni, B. O. Lorenzi, and D. Narducci. Simultaneous increase in electrical conductivity and seebeck coefficient in highly boron-doped nanocrystalline Si. *Nanotechnology*, 24(20):205402, 2013.

[34] D. Dragoman and M. Dragoman. Giant thermoelectric effect in graphene. *Appl. Phys. Lett.*, 91(20):203116, 2007.

[35] M. Cheng. Large thermoelectric effect in graphene superlattices. *Physica E*, 46:189, 2012.

[36] N. Neophytou and H. Kosina. Optimizing thermoelectric power factor by means of a potential barrier. *J. Appl. Phys.*, 114(4):044315, 2013.

[37] G. Jeffrey Snyder and Eric S. Toberer. Complex thermoelectric materials. *Nature Mater.*, 7:105–114, 2008.

[38] Sootsman Joseph R, Chung Duck Young, and Kanatzidis Mercouri G. New and old concepts in thermoelectric materials. *Angewandte Chemie International Edition*, 48(46):8616–8639, 2009.

[39] Li-Dong Zhao, Shih-Han Lo, Yongsheng Zhang, Hui Sun, Gangjian Tan, Ctirad Uher, C. Wolverton, Vinayak P. Dravid, and Mercouri G. Kanatzidis. Ultralow thermal conductivity and high thermoelectric figure of merit in snse crystals. *Nature*, 508(7496):373–377, 2014.

[40] L. Esaki. New phenomenon in narrow germanium $p - n$ junctions. *Phys. Rev.*, 109:603, 1958.

[41] L. Esaki and R. Tsu. Superlattice and negative differential conductivity in semiconductors. *IBM J. Res. Dev.*, 14(1):61, 1970.

[42] R. Lake and S. Datta. Nonequilibrium Green's-function method applied to double-barrier resonant-tunneling diodes. *Phys. Rev. B*, 45:6670, 1992.

[43] A. P. Jauho, N. S. Wingreen, and Y. Meir. Time-dependent transport in interacting and noninteracting resonant-tunneling systems. *Phys. Rev. B*, 50:5528, 1994.

[44] T. Christen and M. Büttiker. Gauge-invariant nonlinear electric transport in mesoscopic conductors. *Europhys. Lett.*, 35(7):523, 1996.

[45] W. R. Frensley. Wigner-function model of a resonant-tunneling semiconductor device. *Phys. Rev. B*, 36:1570, 1987.

[46] B. A. Biegel and J. D. Plummer. Comparison of self-consistency iteration options for the Wigner function method of quantum device simulation. *Phys. Rev. B*, 54:8070, 1996.

[47] M. Nedjalkov, H. Kosina, S. Selberherr, C. Ringhofer, and D. K. Ferry. Unified particle approach to Wigner-Boltzmann transport in small semiconductor devices. *Phys. Rev. B*, 70(11):115319, 2004.

[48] L. D. Hicks and M. S. Dresselhaus. Effect of quantum-well structures on the thermoelectric figure of merit. *Phys. Rev. B*, 47:12727, 1993.

[49] J. O. Sofo and G. D. Mahan. Thermoelectric figure of merit of superlattices. *Appl. Phys. Lett.*, 65(21):2690, 1994.

[50] L. D. Hicks, T. C. Harman, X. Sun, and M. S. Dresselhaus. Experimental study of the effect of quantum-well structures on the thermoelectric figure of merit. *Phys. Rev. B*, 53:R10493, 1996.

[51] P. J. Lin-Chung and T. L. Reinecke. Thermoelectric figure of merit of composite superlattice systems. *Phys. Rev. B*, 51:13244, 1995.

[52] D. A. Broido and T. L. Reinecke. Thermoelectric transport in quantum well superlattices. *Appl. Phys. Lett.*, 70(21):2834, 1997.

[53] R. Venkatasubramanian, E. Siivola, and T. S. Colpitts. In-plane thermoelectric properties of freestanding Si/Ge superlattice structures. In *Seventeenth International Conference on Thermoelectrics. Proceedings ICT98 (Cat. No.98TH8365)*, page 191, 1998.

[54] T. Koga, X. Sun, S. B. Cronin, and M. S. Dresselhaus. Carrier pocket engineering applied to strained Si/Ge superlattices to design useful thermoelectric materials. *Appl. Phys. Lett.*, 75(16):2438, 1999.

[55] A. Shakouri, C. LaBounty, J. Piprek, P. Abraham, and P. Bowen. Thermionic emission cooling in single barrier heterostructures. *Appl. Phys. Lett.*, 74(1):88, 1999.

[56] Gehong Zeng, A. Shakouri, C. L. Bounty, G. Robinson, E. Croke, P. Abraham, Xiafeng Fan, H. Reese, and J. E. Bowers. $\mathrm{Si/Ge}$ micro-cooler. *Electron. Lett.*, 35(24):2146, 1999.

[57] X. Fan, G. Zeng, C. LaBounty, J. E. Bowers, E. Croke, C. C. Ahn, S. Huxtable, A. Majumdar, and A. Shakouri. $\mathrm{SiGeC/Si}$ superlattice microcoolers. *Appl. Phys. Lett.*, 78(11):1580, 2001.

[58] X. Fan, G. Zeng, E. Croke, C. LaBounty, D. Vashaee, A. Shakouri, and J. E. Bowers. High cooling power density $\mathrm{SiGe/Ge}$ microcoolers. *Electron. Lett.*, 37(2):126, 2001.

[59] C. LaBounty, A. Shakouri, and John E. Bowers. Design and characterization of thin film microcoolers. *J. Appl. Phys.*, 89(7):4059–4064, 2001.

[60] C. J. LaBounty, A. Shakouri, P. Abraham, and J. E. Bowers. Monolithic integration of thin-film coolers with optoelectronic devices. *Opt. Eng.*, 39(11):2847, 2000.

[61] D. A. Broido and T. L. Reinecke. Thermoelectric power factor in superlattice systems. *Appl. Phys. Lett.*, 77(5):705, 2000.

[62] D. A. Broido and T. L. Reinecke. Theory of thermoelectric power factor in quantum well and quantum wire superlattices. *Phys. Rev. B*, 64(4):045324, 2001.

[63] J. C. Caylor, K. Coonley, J. Stuart, T. Colpitts, and R. Venkatasubramanian. Enhanced thermoelectric performance in pbte-based superlattice structures from reduction of lattice thermal conductivity. *Appl. Phys. Lett.*, 87(2):023105, 2005.

[64] H. Beyer, J. Nurnus, H. Böttner, A. Lambrecht, T. Roch, and G. Bauer. PbTe based superlattice structures with high thermoelectric efficiency. *Appl. Phys. Lett.*, 80(7):1216, 2002.

[65] A. Khitun, K. L. Wang, and G. Chen. Thermoelectric figure of merit enhancement in a quantum dot superlattice. *Nanotechnology*, 11(4):327, 2000.

[66] Y. M. Lin and M. S. Dresselhaus. Thermoelectric properties of superlattice nanowires. *Phys. Rev. B*, 68:075304, 2003.

[67] A. A. Balandin and O. L. Lazarenkova. Mechanism for thermoelectric figure-of-merit enhancement in regimented quantum dot superlattices. *Appl. Phys. Lett.*, 82(3):415, 2003.

[68] Z. Bian, M. Zebarjadi, R. Singh, Y. Ezzahri, A. Shakouri, G. Zeng, H. Bahk, J, J. E. Bowers, J. M. O. Zide, and A. C. Gossard. Cross-plane seebeck coefficient and lorenz number in superlattices. *Phys. Rev. B*, 76:205311, 2007.

[69] T. C. Harman, P. J. Taylor, D. L. Spears, and M. P. Walsh. Thermoelectric quantum-dot superlattices with high ZT. *J. Electron. Mater.*, 29(1):L1, 2000.

[70] C. Jacoboni and L. Reggiani. The monte-carlo method for the solution of charge transport in semiconductors with applications to covalent materials. *Rev. Mod. Phys.*, 55:645, 1983.

[71] M. Mohamed, Z. Aksamija, W. Vitale, F. Hassan, K.-H. Park, and U. Ravaioli. A conjoined electron and thermal transport study of thermal degradation induced during normal operation of multigate transistors. *IEEE Trans. Electron Devices*, 61:976, 2014.

[72] G. Chindalore, S. A. Hareland, S. A. Jallepalli, A. F. Tasch, C. M. Maziar, V. K. F. Chia, and S. Smith. Experimental determination of threshold voltage shifts due to quantum mechanical effects in MOS electron and hole inversion layers. *IEEE Electron Dev. Lett.*, 18(5):206, 1997.

[73] C.-Y. Wu, S. Banerjee, K. Sadra, B.G. Streetman, and R. Sivan. Quantization effects in inversion layers of PMOSFET on Si (100) substrates. *IEEE Electron Dev. Lett.*, 17(6):276, 1996.

[74] M. Nedjalkov, D. Querlioz, P. Dollfus, and H. Kosina. Review chapter: Wigner function approach. In *Nano-Electronic Devices*, page 289. Springer New York, 2011.

[75] E. Wigner. On the quantum correction for thermodynamic equilibrium. *Phys. Rev.*, 40:749, 1932.

[76] J. Weinbub and D. K. Ferry. Recent advances in wigner function approaches. *Appl. Phys. Rev*, 5(4):041104, 2018.

[77] R. Rosati, F. Dolcini, R. C. Iotti, and F. Rossi. Wigner-function formalism applied to semiconductor quantum devices: Failure of the conventional boundary condition scheme. *Phys. Rev. B*, 88:035401, 2013.

[78] D. Taj, L. Genovese, and F. Rossi. Quantum-transport simulations with the Wigner-function formalism: Failure of conventional boundary-condition schemes. *Europhys. Lett.*, 74(6):1060, 2006.

[79] Z. Zhan, E. Colomés, and X. Oriols. Unphysical features in the application of the boltzmann collision operator in the time-dependent modeling of quantum transport. *J. Comput. Electron.*, 15(4):1206, 2016.

[80] R. C. Iotti, F. Dolcini, and F. Rossi. Wigner-function formalism applied to semiconductor quantum devices: Need for nonlocal scattering models. *Phys. Rev. B*, 96:115420, 2017.

[81] R. Rosati, R. C. Iotti, F. Dolcini, and F. Rossi. Derivation of nonlinear single-particle equations via many-body lindblad superoperators: A density-matrix approach. *Phys. Rev. B*, 90:125140, 2014.

[82] F. Dolcini, R. C. Iotti, and F. Rossi. Interplay between energy dissipation and reservoir-induced thermalization in nonequilibrium quantum nanodevices. *Phys. Rev. B*, 88:115421, 2013.

[83] E. Colomés, Z. Zhan, D. Marian, and X. Oriols. Quantum dissipation with conditional wave functions: Application to the realistic simulation of nanoscale electron devices. *Phys. Rev. B*, 96:075135, Aug 2017.

[84] S. Datta. Nanoscale device modeling: the green's function method. *Superlatt. Microstruct.*, 28:253, 2000.

[85] A. P. Jauho H. Haug. *Quantum Kinetics in Transport and Optics of Semiconductors*, volume 123 of *Springer Series in Solid-State Sciences*. Springer-Verlag Berlin Heidelberg, 2008.

[86] C. Caroli, R. Combescot, P. Nozieres, and D. Saint-James. Direct calculation of the tunneling current. *J. Phys. C*, 4(8):916, 1971.

[87] Supriyo Datta. *Electronic Transport in Mesoscopic Systems*, page 375. Cambridge Studies in Semiconductor Physics and Microelectronic Engineering. Cambridge University Press, 1995.

[88] A. Bulusu and D. G. Walker. Quantum modeling of thermoelectric performance of strained Si/Ge/Si superlattices using the nonequilibrium *g*reen's function method. *J. Appl. Phys.*, 102(7):073713, 2007.

[89] A. Bulusu and D. G. Walker. Quantum modeling of thermoelectric properties of Si/Ge/Si superlattices. *IEEE Trans. Electron Devices*, 55(1):423, 2008.

[90] T. Grange. Electron transport in quantum wire superlattices. *Phys. Rev. B*, 89:165310, 2014.

[91] Vassilios Vargiamidis and Neophytos Neophytou. Hierarchical nanostructuring approaches for thermoelectric materials with high power factors. *Phys. Rev. B*, 99:045405, 2019.

[92] A. I. Boukai, Y. Bunimovich, J. Tahir-Kheli, J. Yu, W. A. Goddard III, and J. R. Heath. Silicon nanowires as efficient thermoelectric materials. *Nature*, 451:168, 2008.

[93] A.I. Hochbaum, R. Chen, R.D. Delgado, W. Liang, E.C. Garnett, M. Najarian, A. Majumdar, and P. Yang. Enhanced thermoelectric performance of rough silicon nanowires. *Nature*, 451:163, 2008.

[94] T. E. Humphrey and H. Linke. Reversible thermoelectric nanomaterials. *Phys. Rev. Lett.*, 94:096601, Mar 2005.

[95] B. Zheng, C. Ma, D. Li, J. Lan, Z. Zhang, X. Sun, W. Zheng, T. Yang, C. Zhu, G. Ouyang, G. Xu, X. Zhu, X. Wang, and A. Pan. Band alignment engineering in two-dimensional lateral heterostructures. *J. Am. Chem. Soc.*, 140(36):11193, 2018.

[96] H. P. Komsa, S. Kurasch, O. Lehtinen, U. Kaiser, and A. V. Krasheninnikov. From point to extended defects in two-dimensional MoS_2: Evolution of atomic structure under electron irradiation. *Phys. Rev. B*, 88:035301, 2013.

[97] E. Akhoundi and M. Sharifi. Computational study of a new resonant tunneling diode based on an MoS_2 nanoribbon with sulfur line vacancies. *J. Comput. Electron.*, 16(2):253, 2017.

[98] Y. Lin, R. K. Ghosh, R. Addou, N. Lu, S. M. Eichfeld, H. Zhu, M. Li, X. Peng, M. J. Kim, L. J. Li, R. M. Wallace, S. Datta, and J. A. Robinson. Atomically thin resonant tunnel diodes built from synthetic van der waals heterostructures. *Nat. Commun.*, 6:7311, 2015.

[99] P. M. Campbell, A. Tarasov, C. A. Joiner, W. J. Ready, and E. M. Vogel. Enhanced resonant tunneling in symmetric 2d semiconductor vertical heterostructure transistors. *ACS Nano*, 9(5):5000, 2015.

[100] J. Shim, D. Oh, S.and Kang, S. Jo, M. H. Ali, W. Choi, K. Heo, J. Jeon, S. Lee, M. Kim, Y. J. Song, and J. H. Park. Phosphorene/rhenium disulfide heterojunction-based negative differential resistance device for multi-valued logic. *Nat. Commun.*, 7:13413, 2016.

[101] Yuri M. Zuev, Willy Chang, and Philip Kim. Thermoelectric and magnetothermoelectric transport measurements of graphene. *Phys. Rev. Lett.*, 102(9):096807, 2009.

[102] Peng Wei, Wenzhong Bao, Yong Pu, Chun Ning Lau, and Jing Shi. Anomalous thermoelectric transport of dirac particles in graphene. *Phys. Rev. Lett.*, 102(16):166808, 2009.

[103] Fereshte Ghahari, Hong-Yi Xie, Takashi Taniguchi, Kenji Watanabe, Matthew S. Foster, and Philip Kim. Enhanced thermoelectric power in graphene: Violation of the mott relation by inelastic scattering. *Phys. Rev. Lett.*, 116:136802, 2016.

[104] Jeong Yun Kim and Jeffrey C. Grossman. High-efficiency thermoelectrics with functionalized graphene. *Nano Lett.*, 15(5):2830–2835, 2015.

[105] S. V. Koniakhin and E. D. Eidelman. Phonon drag thermopower in graphene in equipartition regime. *Europhys. Lett.*, 103(3):37006, 2013.

[106] G. Ding, C. Wang, G. Gao, K. Yao, C. Dun, C. Feng, D. Li, and G. Zhang. Engineering of charge carriers via a two-dimensional heterostructure to enhance the thermoelectric figure of merit. *Nanoscale*, 10:7077, 2018.

[107] V. Hung Nguyen, M. C. Nguyen, H. V. Nguyen, J. Saint-Martin, and P. Dollfus. Enhanced thermoelectric figure of merit in vertical graphene junctions. *Appl. Phys. Lett.*, 105(13):133105, 2014.

[108] S. J. Liang, B. Liu, W. Hu, K. Zhou, and L. K. Ang. Thermionic energy conversion based on graphene van der waals heterostructures. *Sci. Rep*, 7:46211, 2017.

[109] C. C. Chen, Z. Li, L. Shi, and S. B. Cronin. Thermoelectric transport across graphene/hexagonal boron nitride/graphene heterostructures. *Nano Res.*, 8(2):666, 2015.

[110] P. S. Mahapatra, K. Sarkar, H. R. Krishnamurthy, S. Mukerjee, and A. Ghosh. Seebeck coefficient of a single van der waals junction in twisted bilayer graphene. *Nano Lett.*, 17(11):6822, 2017.

[111] K S Bhargavi and S S Kubakaddi. Phonon-drag thermopower in a monolayer mos_2. *J. Phys.: Condens. Matter*, 26(48):485013, 2014.

[112] H. P. R. Frederikse. Thermoelectric power of germanium below room temperature. *Phys. Rev.*, 92:248–252, Oct 1953.

[113] T. H. Geballe and G. W. Hull. Seebeck effect in germanium. *Phys. Rev.*, 94(5):1134–1140, 1954.

[114] R Mansfield and S A Salam. Electrical properties of molybdenite. *Proceedings of the Physical Society. Section B*, 66(5):377–385, may 1953.

[115] S. M. Puri and T. H. Geballe. Phonon drag in n-type insb. *Phys. Rev.*, 136:A1767–A1774, Dec 1964.

[116] R. P. Chasmar and R. Stratton. The thermoelectric figure of merit and its relation to thermoelectric generators. *J. Electron. Control*, 7(1):52–72, 1959.

[117] Jun Yan, Prashun Gorai, Brenden Ortiz, Sam Miller, Scott A. Barnett, Thomas Mason, Vladan Stevanovi, and Eric S. Toberer. Material descriptors for predicting thermoelectric performance. *Energy Environ. Sci.*, 8(3):983–994, 2015.

[118] Evan Witkoske, Xufeng Wang, Mark Lundstrom, Vahid Askarpour, and Jesse Maassen. Thermoelectric band engineering: The role of carrier scattering. *J. Appl. Phys.*, 122(17):175102, 2017.

[119] Zachary M. Gibbs, Francesco Ricci, Guodong Li, Hong Zhu, Kristin Persson, Gerbrand Ceder, Geoffroy Hautier, Anubhav Jain, and G. Jeffrey Snyder. Effective mass and fermi surface complexity factor from ab initio band structure calculations. *npj Comput. Mater.*, 3(1):8, 2017.

[120] R.W. McKinney, P. Gorai, V. Stevanovic, and E. S. Toberer. Search for new thermoelectric materials with low lorenz number. *J. Mater. Chem. A*, 5:17302–17311, 2017.

[121] G. Krishnendu and S. Uttam. Thermoelectric transport coefficients in mono-layer $\mathrm{MoS_2}$ and $\mathrm{WSe_2}$: Role of substrate, interface phonons, plasmon, and dynamic screening. *J. Appl. Phys.*, 118(13):135711, 2015.

[122] H. Babaei, J. M. Khodadadi, and S. Sinha. Large theoretical thermoelectric power factor of suspended single-layer $\mathrm{MoS_2}$. *Appl. Phys. Lett.*, 105(19):193901, 2014.

[123] Yongfu Sun, Hao Cheng, Shan Gao, Qinghua Liu, Zhihu Sun, Chong Xiao, Changzheng Wu, Shiqiang Wei, and Yi Xie. Atomically thick bismuth selenide freestanding single layers achieving enhanced thermoelectric energy harvesting. *J. Am. Chem. Soc.*, 134(50):20294–20297, December 2012.

[124] G. Cheon, K. N. Duerloo, A. D. Sendek, C. Porter, Y. Chen, and E. J. Reed. Data mining for new two- and one-dimensional weakly bonded solids and lattice-commensurate heterostructures. *Nano Lett*, 17(3):1915–1923, 2017.

[125] S. Haastrup, M. Strange, M. Pandey, T. Deilmann, P. S. Schmidt, N. F. Hinsche, M. N. Gjerding, D. Torelli, P. M. Larsen, A. C. Riis-Jensen, J. Gath, K. W. Jacobsen, J. J. Mortensen, T. Olsen, and K. S. Thygesen. The computational 2d materials database: high-throughput modeling and discovery of atomically thin crystals. *2D Materials*, 5(4):042002, 2018.

[126] N. Mounet, M. Gibertini, P. Schwaller, D. Campi, A. Merkys, A. Marrazzo, T. Sohier, I. E. Castelli, A. Cepellotti, G. Pizzi, and N. Marzari. Two-dimensional materials from high-throughput computational exfoliation of experimentally known compounds. *Nat. Nanotech*, 13(3):246–252, 2018.

[127] K. Kaasbjerg, K. S. Thygesen, and K. W. Jacobsen. Phonon-limited mobility in n-type single-layer $\mathrm{MoS_2}$ from first principles. *Phys. Rev. B*, 85:115317, 2012.

[128] S. Haastrup, M. Strange, M. Pandey, T. Deilmann, P. S. Schmidt, N. F. Hinsche, M. N. Gjerding, D. Torelli, P. M. Larsen, A. C. Riis-Jensen, J. Gath, K. W. Jacobsen, J. J. Mortensen, T. Olsen, and K. S. Thygesen. The computational 2d materials database: high-throughput modeling and discovery of atomically thin crystals. *2D Materials*, 5(4):042002, 2018.

[129] Zhengwei Zhang, Peng Chen, Xidong Duan, Ketao Zang, Jun Luo, and Xiangfeng Duan. Robust epitaxial growth of two-dimensional heterostructures, multiheterostructures, and superlattices. *Science*, 357(6353):788–792, 2017.

[130] G. D. Mahan and L. M. Woods. Multilayer thermionic refrigeration. *Phys. Rev. Lett.*, 80:4016–4019, 1998.

[131] Amirhossein Behranginia, Poya Yasaei, Arnab K. Majee, Vinod K. Sangwan, Fei Long, Cameron J. Foss, Tara Foroozan, Shadi Fuladi, Mohammad Reza Hantehzadeh, Reza Shahbazian-Yassar, Mark C. Hersam, Zlatan Aksamija, and Amin Salehi-Khojin. Direct growth of high mobility and low-noise lateral $\mathrm{MoS_2}$-graphene heterostructure electronics. *Small*, 13(30):1604301, 2017.

[132] Arnab K. Majee, Adithya Kommini, and Zlatan Aksamija. Electronic transport and thermopower in 2d and 3d heterostructures-a theory perspective. *Ann. Phys. (Berlin)*, 531(9):1800510, 2019.

[133] Jun Kang, Sefaattin Tongay, Jian Zhou, Jingbo Li, and Junqiao Wu. Band offsets and heterostructures of two-dimensional semiconductors. *Appl. Phys. Lett.*, 102(1):012111, 2013.

[134] Daniel Trainer, Yuan Zhang, Fabrizio Bobba, Xiaoxing Xi, Saw-Wai Hla, and Maria Iavarone. The effects of atomic-scale strain relaxation on the electronic properties of monolayer mos2. *ACS Nano*, 13(7):8284–8291, July 2019.

[135] Krishna P. Dhakal, Shrawan Roy, Houk Jang, Xiang Chen, Won Seok Yun, Hyunmin Kim, JaeDong Lee, Jeongyong Kim, and Jong-Hyun Ahn. Local strain induced band gap modulation and photoluminescence enhancement of multilayer transition metal dichalcogenides. *Chem. Mater.*, 29(12):5124–5133, June 2017.

[136] Sefaattin Tongay, Deepa S. Narang, Jun Kang, Wen Fan, Changhyun Ko, Alexander V. Luce, Kevin X. Wang, Joonki Suh, K. D. Patel, V. M. Pathak, Jingbo Li, and Junqiao Wu. Two-dimensional semiconductor alloys: Monolayer $Mo_{1-x}W_xSe_2$. *Appl. Phys. Lett.*, 104(1):012101, 2014.

[137] Lutz Waldecker, Archana Raja, Malte Rösner, Christina Steinke, Aaron Bostwick, Roland J. Koch, Chris Jozwiak, Takashi Taniguchi, Kenji Watanabe, Eli Rotenberg, Tim O. Wehling, and Tony F. Heinz. Rigid band shifts in two-dimensional semiconductors through external dielectric screening. *Phys. Rev. Lett.*, 123:206403, 2019.

[138] G. Ding, C. Wang, G. Gao, K. Yao, C. Dun, C. Feng, D. Li, and G. Zhang. Engineering of charge carriers via a two-dimensional heterostructure to enhance the thermoelectric figure of merit. *Nanoscale*, 10:7077, 2018.

[139] Guangqian Ding, Junjie He, G. Y. Gao, and Kailun Yao. Two-dimensional MoS_2-$MoSe_2$ lateral superlattice with minimized lattice thermal conductivity. *J. Appl. Phys.*, 124(16):165101, 2018.

[140] Z. Bian and A. Shakouri. *Monte Carlo Simulation of Solid-State Thermionic Energy Conversion Devices Based on Non-Planar Heterostructure Interfaces*, pages 179–182. Springer Berlin Heidelberg, Berlin, Heidelberg, 2006.

[141] D. L. Rode. Electron mobility in direct-gap polar semiconductors. *Phys. Rev. B*, 2:1012, Aug 1970.

[142] D. L. Rode. Electron transport in InSb, InAs, and InP. *Phys. Rev. B*, 3:3287, 1971.

[143] O. Jonasson and I. Knezevic. Dissipative transport in superlattices within the wigner function formalism. *J. Comput. Electron.*, 14(4):879–887, Dec 2015.

[144] Paolo Giannozzi, Stefano Baroni, Nicola Bonini, Matteo Calandra, Roberto Car, Carlo Cavazzoni, Davide Ceresoli, Guido L Chiarotti, Matteo Cococcioni, Ismaila Dabo, Andrea Dal Corso, Stefano de Gironcoli, Stefano Fabris, Guido Fratesi, Ralph Gebauer, Uwe Gerstmann, Christos Gougoussis, Anton Kokalj, Michele Lazzeri, Layla Martin-Samos, Nicola Marzari, Francesco Mauri, Riccardo Mazzarello, Stefano Paolini, Alfredo Pasquarello, Lorenzo Paulatto, Carlo Sbraccia, Sandro Scandolo, Gabriele Sclauzero, Ari P Seitsonen, Alexander Smogunov, Paolo Umari, and Renata M Wentzcovitch. QUANTUM ESPRESSO: a modular and open-source software project for quantum simulations of materials. *Journal of Physics: Condensed Matter*, 21(39):395502, sep 2009.

[145] W.R. Fehlner and P.D. Loly. Save: A general approach for calculating the spectral properties of solids. *Solid St. Commun.*, 15(1):69 – 72, 1974.

[146] Kedar Hippalgaonkar, Ying Wang, Yu Ye, Diana Y. Qiu, Hanyu Zhu, Yuan Wang, Joel Moore, Steven G. Louie, and Xiang Zhang. High thermoelectric power factor in two-dimensional crystals of $\mathrm{Mos_2}$. *Phys. Rev. B*, 95:115407, Mar 2017.

[147] Morteza Kayyalha, Jesse Maassen, Mark Lundstrom, Li Shi, and Yong P. Chen. Gate-tunable and thickness-dependent electronic and thermoelectric transport in few-layer mos2. *J. Appl. Phys.*, 120(13):134305, 2016.

[148] Masaro Yoshida, Takahiko Iizuka, Yu Saito, Masaru Onga, Ryuji Suzuki, Yijin Zhang, Yoshihiro Iwasa, and Sunao Shimizu. Gate-optimized thermoelectric power factor in ultrathin wse2 single crystals. *Nano Lett.*, 16(3):2061–2065, March 2016.

[149] M. Kriener, A. Kikkawa, T. Suzuki, R. Akashi, R. Arita, Y. Tokura, and Y. Taguchi. Modification of electronic structure and thermoelectric properties of hole-doped tungsten dichalcogenides. *Phys. Rev. B*, 91:075205, Feb 2015.

[150] Nan Ma and Debdeep Jena. Charge scattering and mobility in atomically thin semiconductors. *Phys. Rev. X*, 4:011043, Mar 2014.

[151] Junxi Duan, Xiaoming Wang, Xinyuan Lai, Guohong Li, Kenji Watanabe, Takashi Taniguchi, Mona Zebarjadi, and Eva Y. Andrei. High thermoelectricpower factor in graphene/hbn devices. *Proc. Natl. Acad. Sci. U.S.A.*, 113(50):14272–14276, 2016.

[152] A. Miele, R. Fletcher, E. Zaremba, Y. Feng, C. T. Foxon, and J. J. Harris. Phonon-drag thermopower and weak localization. *Phys. Rev. B*, 58:13181–13190, Nov 1998.

[153] B. Tieke, R. Fletcher, U. Zeitler, M. Henini, and J. C. Maan. Thermopower measurements of the coupling of phonons to electrons and composite fermions. *Phys. Rev. B*, 58:2017–2025, Jul 1998.

[154] W. Kang, Song He, H. L. Stormer, L. N. Pfeiffer, K. W. Baldwin, and K. W. West. Temperature dependent scattering of composite fermions. *Phys. Rev. Lett.*, 75:4106–4109, Nov 1995.

[155] R. Fletcher, M. Tsaousidou, P.T. Coleridge, Y. Feng, and Z.R. Wasilewski. Electronphonon coupling and phonon-drag thermopower of a very low mobility 2deg. *Physica E: Low-dimensional Systems and Nanostructures*, 12(1):478 – 481, 2002. Proceedings of the Fourteenth International Conference on the Ele ctronic Properties of Two-Dimensional Systems.

[156] V I Fal'ko and S V Iordanskii. Electron-phonon drag effect at 2d landau levels. *J. Phys.: Condens. Matter*, 4(46):9201–9212, nov 1992.

[157] I. Pallecchi, F. Telesio, D. Marré, D. Li, S. Gariglio, J.-M. Triscone, and A. Filippetti. Large phonon-drag enhancement induced by narrow quantum confinement at the $\mathrm{laalo_3/srtio_3}$ interface. *Phys. Rev. B*, 93:195309, May 2016.

[158] C. Ruf, H. Obloh, B. Junge, E. Gmelin, K. Ploog, and G. Weimann. Phonon-drag effect in gaas-$\mathrm{al_xga_{1-x}as}$ heterostructures at very low temperatures. *Phys. Rev. B*, 37:6377–6380, Apr 1988.

[159] J. Vavro, M. C. Llaguno, J. E. Fischer, S. Ramesh, R. K. Saini, L. M. Ericson, V. A. Davis, R. H. Hauge, M. Pasquali, and R. E. Smalley. Thermoelectric power of p-doped single-wall carbon nanotubes and the role of phonon drag. *Phys. Rev. Lett.*, 90:065503, Feb 2003.

[160] W. Zhou, J. Vavro, N. M. Nemes, J. E. Fischer, F. Borondics, K. Kamarás, and D. B. Tanner. Charge transfer and fermi level shift in p-doped single-walled carbon nanotubes. *Phys. Rev. B*, 71:205423, May 2005.

[161] M. Tsaousidou. Theory of phonon-drag thermopower of extrinsic semiconducting single-wall carbon nanotubes and comparison with previous experimental data. *Phys. Rev. B*, 81:235425, Jun 2010.

[162] M. Tsaousidou. Phonon-drag thermopower of ballistic semiconducting single-wall carbon nanotubes and comparison with the semiclassical result. *EPL (Europhysics Letters)*, 93(4):47010, feb 2011.

[163] S. S. Kubakaddi and K. S. Bhargavi. Enhancement of phonon-drag thermopower in bilayer graphene. *Phys. Rev. B*, 82:155410, Oct 2010.

[164] S. S. Kubakaddi. Interaction of massless dirac electrons with acoustic phonons in graphene at low temperatures. *Phys. Rev. B*, 79:075417, Feb 2009.

[165] K S Bhargavi and S S Kubakaddi. Phonon-drag thermopower in an armchair graphene nanoribbon. *Journal of Physics: Condensed Matter*, 23(27):275303, jun 2011.

[166] Conyers Herring. Theory of the thermoelectric power of semiconductors. *Phys. Rev.*, 96(5):1163–1187, 1954.

[167] D G Cantrell and P N Butcher. A calculation of the phonon-drag contribution to the thermopower of quasi-2d electrons coupled to 3d phonons. ii. applications. *J. Phys. Chem.*, 20(13):1993–2003, 1987.

[168] M. Tsaousidou, P. N. Butcher, and G. P. Triberis. Fundamental relationship between the Herring and Cantrell-Butcher formulas for the phonon-drag thermopower of two-dimensional electron and hole gases. *Phys. Rev. B*, 64(16):165304, 2001.

[169] Joseph Callaway. Model for lattice thermal conductivity at low temperatures. *Phys. Rev.*, 113:1046–1051, 1959.

[170] Younès Ezzahri and Karl Joulain. Dynamical thermal conductivity of bulk semiconductor crystals. *J. Appl. Phys.*, 112(8):083515, 2012.

[171] Philip B. Allen. Improved callaway model for lattice thermal conductivity. *Phys. Rev. B*, 88:144302, 2013.

[172] Z. Aksamija and I. Knezevic. Lattice thermal conductivity of graphene nanoribbons: anisotropy and edge roughness scattering. *Appl. Phys. Lett.*, 98:141919, 2011.

[173] Z. Aksamija and I. Knezevic. Thermal transport in graphene nanoribbons supported on SiO_2. *Phys. Rev. B*, 86:165426, 2012.

[174] Arnab K. Majee and Zlatan Aksamija. Length divergence of the lattice thermal conductivity in suspended graphene nanoribbons. *Phys. Rev. B*, 93:235423, 2016.

[175] K. S. Novoselov, A. K. Geim, S. V. Morozov, D. Jiang, Y. Zhang, S. V. Dubonos, I. V. Grigorieva, and A. A. Firsov. Electric field effect in atomically thin carbon films. *Science*, 306(5696):666–669, 2004.

[176] Julia Berashevich and Tapash Chakraborty. Tunable band gap and magnetic ordering by adsorption of molecules on graphene. *Phys. Rev. B*, 80:033404, Jul 2009.

[177] Gianluca Giovannetti, Petr A. Khomyakov, Geert Brocks, Paul J. Kelly, and Jeroen van den Brink. Substrate-induced band gap in graphene on hexagonal boron nitride: Ab initio density functional calculations. *Phys. Rev. B*, 76:073103, Aug 2007.

[178] S. Y. Zhou, G.-H. Gweon, A. V. Fedorov, P. N. First, W. A. de Heer, D.-H. Lee, F. Guinea, A. H. Castro Neto, and A. Lanzara. Substrate-induced bandgap opening in epitaxial graphene. *Nat. Mater.*, 6(10):770–775, October 2007.

[179] K. Fuchs. The conductivity of thin metallic films according to the electron theory of metals. *Proc. Cam. Phil. Soc.*, 34:100–108, 1938.

[180] Junxi Duan, Xiaoming Wang, Xinyuan Lai, Guohong Li, Kenji Watanabe, Takashi Taniguchi, Mona Zebarjadi, and Eva Y. Andrei. High thermoelectricpower factor in graphene/hbn devices. *Proc. Natl. Acad. Sci.*, 113(50):14272–14276, 2016.

[181] M. Zebarjadi. Electronic cooling using thermoelectric devices. *Appl. Phys. Lett.*, 106(20):203506, 2015.

[182] Achim Harzheim, Fabian Könemann, Bernd Gotsmann, Herre van der Zant, and Pascal Gehring. Single-material graphene thermocouples. *Adv. Funct. Mater.*, 30(22):2000574, 2020.

[183] Rafi Bistritzer and Allan H. MacDonald. Moiré bands in twisted double-layer graphene. *Proc. Natl. Acad. Sci*, 108(30):12233–12237, 2011.

[184] Adithya Kommini and Zlatan Aksamija. Materials selection rules for optimum power factor in two-dimensional thermoelectrics. *J. Phys.: Matter.*, 3(1):015005, nov 2019.

[185] D. van der Marel, H. J. A. Molegraaf, J. Zaanen, Z. Nussinov, F. Carbone, A. Damascelli, H. Eisaki, M. Greven, P. H. Kes, and M. Li. Quantum critical behaviour in a high-tc superconductor. *Nature*, 425(6955):271–274, September 2003.

[186] Yuan Cao, Debanjan Chowdhury, Daniel Rodan-Legrain, Oriol Rubies-Bigorda, Kenji Watanabe, Takashi Taniguchi, T. Senthil, and Pablo Jarillo-Herrero. Strange metal in magic-angle graphene with near planckian dissipation. *Phys. Rev. Lett.*, 124:076801, Feb 2020.

[187] V. J. Emery and S. A. Kivelson. Superconductivity in bad metals. *Phys. Rev. Lett.*, 74:3253–3256, Apr 1995.

[188] J. A. N. Bruin, H. Sakai, R. S. Perry, and A. P. Mackenzie. Similarity of scattering rates in metals showing t-linear resistivity. *Science*, 339(6121):804–807, 2013.

[189] Hryhoriy Polshyn, Matthew Yankowitz, Shaowen Chen, Yuxuan Zhang, K. Watanabe, T. Taniguchi, Cory R. Dean, and Andrea F. Young. Large linear-in-temperature resistivity in twisted bilayer graphene. *Nat. Phys.*, 15(10):1011–1016, 2019.

[190] Stephen Carr, Shiang Fang, Ziyan Zhu, and Efthimios Kaxiras. Exact continuum model for low-energy electronic states of twisted bilayer graphene. *Phys. Rev. Research*, 1:013001, Aug 2019.

[191] D. L. Rode. Electron transport in InSb, InAs, and InP. *Phys. Rev. B*, 3:3287, 1971.

[192] Gabriela C Correa, Cameron J Foss, and Zlatan Aksamija. Interface thermal conductance of van der Waals monolayers on amorphous substrates. *Nanotechnology*, 28(13):135402, 2017.

[193] P. Yasaei, A. Fathizadeh, R. Hantehzadeh, A. K. Majee, A. El-Ghandour, D. Estrada, C. Foster, Z. Aksamija, F. Khalili-Araghi, and A. Salehi-Khojin. Bimodal phonon scattering in graphene grain boundaries. *Nano Lett.*, 15(7):4532–4540, 2015.

[194] K. M. Borysenko, J. T. Mullen, E. A. Barry, S. Paul, Y. G. Semenov, J. M. Zavada, M. Buongiorno Nardelli, and K. W. Kim. First-principles analysis of electron-phonon interactions in graphene. *Phys. Rev. B*, 81:121412, Mar 2010.

[195] Kaito Kanahashi, Masatou Ishihara, Masataka Hasegawa, Hiromichi Ohta, and Taishi Takenobu. Giant power factors in p- and n-type large-area graphene films on a flexible plastic substrate. *npj 2D Mater. Appl.*, 3(1):44, November 2019.

[196] Alexandr I. Cocemasov, Denis L. Nika, and Alexander A. Balandin. Phonons in twisted bilayer graphene. *Phys. Rev. B*, 88:035428, Jul 2013.

[197] Fereshte Ghahari, Hong-Yi Xie, Takashi Taniguchi, Kenji Watanabe, Matthew S. Foster, and Philip Kim. Enhanced thermoelectric power in graphene: Violation of the mott relation by inelastic scattering. *Phys. Rev. Lett.*, 116:136802, 2016.

[198] K. Kim, B. A. Mason, and K. Hess. Inclusion of collision broadening in semiconductor electron-transport simulations. *Phys. Rev. B*, 36:6547–6550, Oct 1987.

[199] Lino Reggiani, Paolo Lugli, and A. P. Jauho. Quantum kinetic equation for electronic transport in nondegenerate semiconductors. *Phys. Rev. B*, 36:6602–6608, Oct 1987.

[200] K. M. Borysenko, J. T. Mullen, X. Li, Y. G. Semenov, J. M. Zavada, M. Buongiorno Nardelli, and K. W. Kim. Electron-phonon interactions in bilayer graphene. *Phys. Rev. B*, 83:161402, Apr 2011.

[201] Mohammad Zarenia, Indra Yudhistira, Shaffique Adam, and Giovanni Vignale. Enhanced hydrodynamic transport in near magic angle twisted bilayer graphene. *Phys. Rev. B*, 101:045421, Jan 2020.

[202] Sunao Shimizu, Junichi Shiogai, Nayuta Takemori, Shiro Sakai, Hiroaki Ikeda, Ryotaro Arita, Tsutomu Nojima, Atsushi Tsukazaki, and Yoshihiro Iwasa. Giant thermoelectric power factor in ultrathin fese superconductor. *Nat. Commun.*, 10(1):825, February 2019.